Characterization and Reactivity of Synthetic Nonheme Oxoiron(IV) Complexes

A DISSERTATION
SUBMITTED TO THE FACULTY OF
UNIVERSITY OF MINNESOTA
BY

Jennifer Otto Bigelow

IN PARTIAL FULFILLMENT OF THE REQUIREMENTS
FOR THE DEGREE OF
DOCTOR OF PHILOSOPHY

Prof. Lawrence Que, Jr.

May 2015

Acknowledgements

I must first and foremost thank Larry Que, Jr. for taking me into his lab at the start of my second year. It was a great risk, and I hope it paid off for him and I haven't caused too much trouble in his life. I have learned an incredible amount in his group. He always pushed me to think more about my results and analysis. I am grateful for having been in his lab as I grew from a student to a scientist.

Pretty much all of the Que group has helped me out at one time or another. My first mentors, Matt Cranswick and Kathy van Heuvelen, not only were around in the early morning to bug with my questions and read drafts for my written but taught me about pretty much every instrumentation in the lab. Matt taught me resonance Raman spectroscopy, and without his and Kathy's responses to my numerous questions, chapter 5 would not be what it is.

Ken Xue and Aidan McDonald, though I am sure they were annoyed with me from time to time, taught me important scientific thinking and helped me with a variety of problem-solving. Ken was the person I went to with questions on how to analyze data and trouble-shooting the bulk electrolysis set up. Aidan helped make the lab safer by teaching me how to handle air-sensitive compounds and even helping me get a mercury bubbler into a waste container. His advice for my oral exam was invaluable.

I also have to thank both Dong Wang and Feifei Li, graduate students who gave over their projects to me. What they were hoping I would accomplish never came to fruition, but new results led me to new pathways. I appreciate their work and thoughts, even if my projects went in different directions.

Jason England was an enormous help in all things TMC-related. Whether helping with the failed purple species (we will not forget you, purple species) project, pointing me in the right direction for ligand synthesis, or arguing over the finer points of the blue species paper, he aided me a great deal in finding my way through the TMC forest.

The current group has read my terrible drafts, listened to my group meetings, and helped me puzzle out whatever I was thinking about. My thanks especially to Mayank, Greg, Scott, Caleb, Will, Lisa, Jai, Johannes and Andy, who at one time or another helped me sort out my thoughts into something approaching coherence and are always willing to

lend me their expertise. Greg reacquainted me with X-ray crystallography this year, helping me solve my only crystal structure since taking the X-ray class. Johannes introduced me to computational chemistry. Mayank helped me with conflicts with the UV-vis spectrometers. Scott and Andy are always there to help me with my laser troubles. Andy, in particular, has always been there when I've wanted to complain or need moral support. Whatever I have accomplished is in part due to working with such a great set of people.

I also have to thank many professors in this department, who helped with all my crazy questions. Phil Buhlmann aided in my electrochemical knowledge and was available for discussions on what the cyclic voltammetry actually meant. Chris Cramer aided my first (small) foray into computational chemistry by use of his supercomputer time. Victor Young was very helpful for crystallographic characterization. The collaboration of Christine McKenzie and Elena Rybak-Akimova allowed chapter 5 to be what it is. John Lipscomb has discussed mechanisms and is yet again on another Que group member's committee, which I appreciate. Connie Lu and Valerie Pierre were both excellent teachers for Physical Inorganic and Mechanisms, respectively, which ended up being the foundation for my research. Connie in particular was incredibly supportive in my first year, which greatly helped me staying in the program.

I would not be writing this if it weren't for the support of my family, especially my parents, who I am sure are tired of my complaints about writing a dissertation by now, but still send me encouragement, including zebra fish emoticons with "just keep swimming" by them. Thanks to my brother, for always finding the humor in things, and for my sister-in-law for understanding the Ph.D. struggle. To my friends, who laughed at my doubts about myself, and kept me sane, I am incredibly grateful. And to my fiancé, Ben, who put up with the struggle, day in, day out, for six years and still wants to marry me. Without his support and love, my transition to a new group might have been more tearful than it was. He was my partner in all this, and though he often was confused at what exactly I was doing, he understood my struggle. Thank you for being there through the tears of frustration and the shouts of success. After this, everything is easy, right?

Dedication

To my family, especially my parents and Ben. They know why.

A Poem Partially Written in Lab Notebook #5

Oh Chemistry! Thou art a fickle god
Your faithful servant I have been in truth
My repeat experiments are but fod-
Der for your perfidious glee. Forsooth!
How many more, so burned by laser bright,
For sacrifice must I lay upon thy pyre?
Against impurities must I longer fight?
A thousand liters quench not thy desire,
Yet capriciously, thou led me astray
To intermediates un-trappable,
Instruments thwarting my every foray
But here I still remain, unflappable.
Am I your Sisyphus, rewarded likewise,
For failure to properly eulogize?

Abstract

Nonheme iron enzymes are prevalent throughout nature and utilize oxygen as the oxidant. While some intermediates are proposed, such as iron(IV)-oxo and iron(III)-peroxo species, the nature of the reactivity of these species has not yet been fully explored. Nonheme synthetic iron model complexes allow for easy modification to probe the reactivity of such species, and allow for characterization for later comparison with enzymes.

This dissertation explores the reactivity of iron(IV)-oxo species supported by a tetramethycyclam framework. Interesting, in contrast to what had been reported previously, the electron-donating properties of the axial ligand do not correspond to the hydrogen atom transfer (HAT) reactivity, while a consistent trend for oxygen atom transfer (OAT) is observed. Ligand tethering is found to have a large impact on the enthalpy of activation. It is proposed that the iron(IV)-oxo moiety rises out of the plane to react, which forces tethered ligands to weaken the axial bond.

The activation of oxygen by synthetic iron complexes, in the presence of either a hydrogen atom donor or an acid and a proton source, has been proposed to mimic enzymatic activity. However, the reexamination of mechanisms previously reported to follow an enzyme-mimicking pathway are instead due to peroxyl radicals. This highlights the importance of testing such mechanisms, as autooxidation is a common problem with many compounds in the presence of dioxygen.

Finally, species such as iron(IV)-oxo and iron(III)-peroxo complexes, as well as related complexes, are characterized by resonance Raman spectroscopy. Many of these complexes have a ligand with a carboxylate moiety, as seen in nonheme enzymes. Characterization of these complexes show similarities between iron(IV)-oxo and iron(III)-peroxo and chromium(IV)-peroxo species reported previously, having similar vibration values, while major differences exist in vibrations between previously reported iodosylarene-iron(III) complexes and new iodosylarene-iron(III) complexes.

Table of Contents

List of Abbreviations

BDPP	(*S*,*S*)-1,1′-(2,6-Pyridinyldimethyl)-bis[2-(diphenylmethanol)pyrrolidine]
Bn-TPEN	*N*-benzyl-*N*,*N*′,*N*′-tris(2-pyridylmethyl)ethane-1,2-diamine
BQCN	*N*,*N*′-dimethyl-*N,N*′-bis(8-quinolyl)cyclohexanediamine
EXAFS	extended X-ray absorption fine structure
HAT	hydrogen atom transfer
KIE	kinetic isotope effect
L^8py_2	*N*,*N*′-bis(2-pyridylmethyl)-1,5-diazacyclooctane
6-Me_3TPA	tris(6-methyl-2-pyridylmethyl)amine
Me_3NTB	tris(1-methylbenzimidazol-2-ylmethyl)amine
N4Py	*N*,*N*-bis(2-pyridylmethyl)-*N*-bis(2-pyridyl)methylamine
OAc	acetate
OAT	oxygen atom transfer
OPr	propionate
OTf	triflate
PyMac	2,7,12-trimethyl-3,7,11,17-tetra-azabicyclo[11.3.1]heptadeca-1(17),13,15-triene
TMC	tetramethylcyclam; 1,4,8,11-Tetramethyl-1,4,8,11-tetraazacyclotetradecane
TMCAc	4,8,11-trimethyl-1,4,8,11-tetraazacyclotetradecane-1-acetate
TMCPrA	4,8,11-trimethyl-1,4,8,11-tetraazacyclotetradecane-1-propionate
TMCS	1-(2-mercaptoethyl)-4,8,11-trimethyl-1,4,8,11-tetraazacyclotetradecane
TMCG_3-tren	1,1,1-tris{2-[N^2-(1,1,3,3-tetramethylguanidino)]ethyl}amine
TMG_2-dien	2',2'-(2,2'-(methylazanediyl)bis(ethane-1,2-diyl))bis(1,1,3,3-tetramethylguanidine
TPA	tris(2-pyridylmethyl)amine
tpa^{Ph}	tris(5-phenylpyrrol-2-ylmethyl)amine)
tpena	N,N,N′-tris(2-pyridylmethyl)ethylenediamine-N′-acetato
TQA	tris(2-quinolylmethyl)amine

List of Schemes

List of Tables

List of Figures

Chapter 1
Nonheme Iron Enzymes and their Synthetic Model Complexes

1.1 Nonheme Iron Enzymes

Nonheme iron enzymes are able to catalyze a wide variety of interesting reactions utilizing oxygen as the oxidant.[1,2] Some of the major nonheme monoiron enzymes and enzyme families include extradiol catechol dioxygenases, Rieske dioxygenases, 2-oxoglutarate-dependent oxidases and oxygenases, tetrahydropterin-containing oxygenases, isopenicillin N-synthase, fosfomycin synthase, and 1-aminocyclopropane-1-carboxylate oxidase. This subset of nonheme iron enzymes utilize similar active sites, where an iron is bound to a 2-His-1-carboxylate facial triad. The commonality of this motif, along the common use of dioxygen as the oxidant, makes the diversity of substrate transformations all the more surprising. Despite the variety of oxidative transformations that these enzymes catalyze, several similar mechanistic pathways are proposed for many of the enzymes.[1,2] These mechanisms often involve oxygen binding to the iron(II), formation of a peroxo species, and cleavage of the O-O bond to provide a high-valent iron intermediate, often proposed to be an iron(IV) or iron(V), which is implicated as the reactive intermediate (Scheme 1.1).

A particularly well-studied enzyme family, 2-oxoglutarate-dependent oxidases and oxygenases, has been shown to require a co-substrate to form the reactive intermediate.[1,2] The co-substrate, 2-oxoglutarate, binds to the active iron center, changing the enzyme, which allows the substrate can enter the active site (Scheme 1.2). Upon oxygen binding, an iron-superoxo species forms. The terminal oxygen then attacks the co-substrate to form an alkylperoxo species. This species loses CO_2 and forms an iron(IV)-oxo species responsible for hydrogen atom abstraction from the substrate. The *S* = 2 iron(IV)-oxo species has been trapped in taurine:α-ketoglurate dioxygenase, TauD,[3–5] and prolyl-4-hydroxylase,[6] as well as related halogenase enzymes CytC3[7,8] and SyrB2.[9] The isomer shift of 0.30 mm/s ± 0.03 mm/s is reported to be indicative of an iron(IV)-oxo intermediate in all enzymes, though the quadrupole doublet absolute value varies from 0.70 to 1.09 mm/s. Only the TauD iron(IV)-oxo intermediate has been characterized by resonance Raman spectroscopy, where a band at 821 cm^{-1} was assigned to an Fe-O stretch.[5] EXAFS of this species indicated a short Fe-O bond of 1.62 Å.[10] The iron(IV)-oxo intermediate was determined to be the reactive intermediate due to a large deuterium

Scheme 1.1: Generalized mechanism of many nonheme iron enzymes.

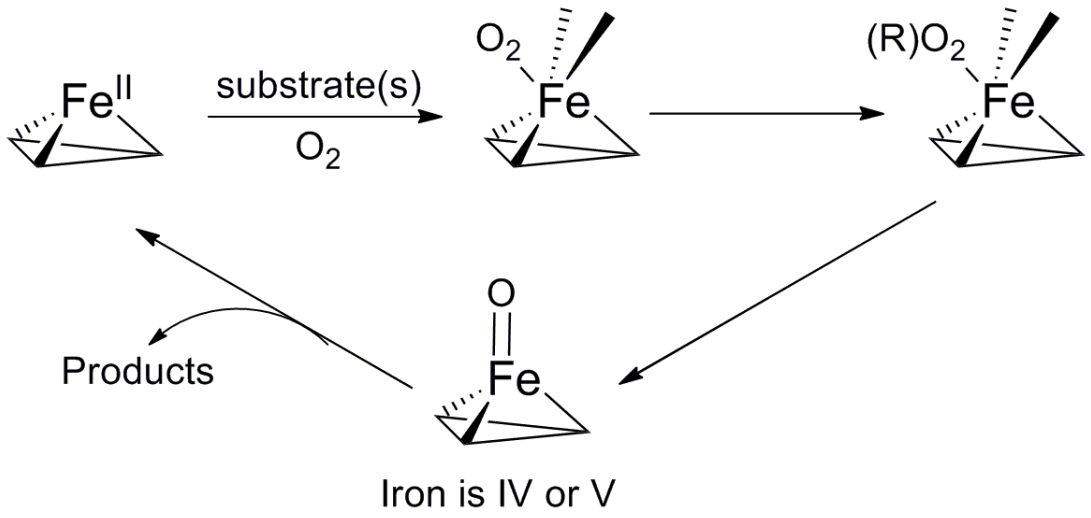

Scheme 1.2: Mechanism of TauD.

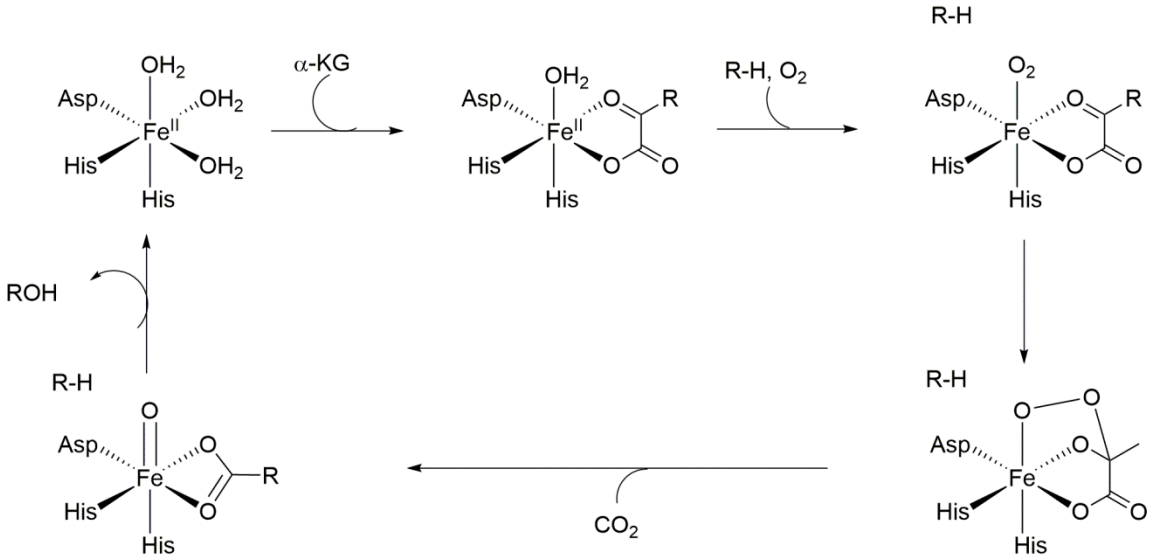

effect with the substrate taurine estimated at ~37.[11] The large KIE > 7 indicates a tunneling mechanism.

Iron(IV)-oxo intermediates are not just proposed in the mechanisms of 2-oxoglutarate-dependent oxidases and oxygenases and halogenases. Tetrahydropterin-containing oxygenases are proposed to form an iron(IV)-oxo intermediate after the cleavage of an alkylperoxo species. An iron(IV) intermediate has been detected by Mössbauer for members of this family: intermediates of phenylalanine hydroxylase (δ = 0.28 mm/s, ΔE_Q = 1.26 mm/s)[12]and tyrosine hydroxylase (0.25 mm/s and ΔE_Q = 1.27 mm/s)[13] are consistent with an iron(IV)-oxo formulation.

While they have not been trapped, an iron(IV)-oxo intermediate is proposed for 1-aminocyclopropane-1-carboxylate oxidase (ACCO) and isopenicillin-N-synthase.[1,2] ACCO is proposed to follow a similar pathway to the 2-oxoglutarate-dependent oxidases and oxygenases.[14] The substrate 1-aminocyclopropane-1-carboxylate binds to the iron at the active site. A superoxo intermediate is proposed that then attacks the substrate to form a peroxo species. This peroxo species undergoes O-O bond cleavage to form an iron(IV)-oxo intermediate. The iron(IV)-oxo intermediate is proposed to attack the substrate to allow for the final products to form.

For isopenicillin-N-synthase, the substrate is proposed to bind through a sulfur atom.[1,2,15] This leaves the site *trans* to the aspartate open, which is different from the other enzymes. After the dioxygen binds to form a putative superoxo intermediate, the terminal oxygen is proposed to abstract a hydrogen atom to form a substrate radical. The peroxo intermediate is proposed to abstract a proton, which allows for the formation of an iron(IV)-oxo intermediate and the first ring closure of the substrate. This intermediate is proposed to abstract another hydrogen atom to form a substrate radical, which allows for the second ring closure and the product formation.

While many of the intermediates, especially for TauD, have been trapped and characterized, there is no consensus on what governs the rate of each step, particularly the iron(IV)-oxo species reacting with the substrate. How do ligand electron-donation, spin state, and sterics allow the enzyme to achieve the goal of turning substrate into product? The understanding of these intermediates can be achieved two ways: through the

investigation of the enzymes themselves, with more attempts to trap and characterize intermediates, and through synthetic model complexes that mimic the reactivity seen in these enzymes. Synthetic model complexes have an advantage of easy changes to the coordination sphere, and thus can be modified to probe a variety of different factors that might affect reactivity, as will be seen in the next section.

1.2 Synthetic Model Systems

1.2.1 Iron(IV)-oxo Complexes

Through the efforts of the Que group and others, many different iron(IV)-oxo complexes have been synthesized. These complexes have allowed for modeling of not only the spectroscopy of the iron(IV)-oxo intermediates found in enzymes, but also the reactivity. A large focus has been investigating the reactivity of these synthetic complexes towards hydrogen atom transfer (HAT), the proposed rate-determining step in many enzymes. These model systems allow for modifications that probe what factors yield more reactive complexes towards HAT. With these biomimetic complexes in hand, investigations pursued factors such as steric, spin, and ligand electron-donation.

Sterics are always a factor that must be evaluated with new iron(IV)-oxo complexes because a decrease in reactivity may be attributed to the inability of the substrate to access the iron(IV)-oxo moiety. For example, [Fe(Tp^{Ph_2})(BF)], upon addition of oxygen, was reported to form a putative iron(IV)-oxo intermediate (Scheme 1.5).[16] This was tested by interception of both oxygen atom transfer (OAT) and hydrogen atom transfer (HAT) substrates. The sterically less hindered cyclohexene was able to intercept the iron(IV)-oxo moiety at much lower concentrations than the more sterically hindered ethylbenzene, even though both substrates have similar bond dissociation energies. Sterically hindered ligands thus counteract productive electronic changes e.g. weakening the ligand field. It is therefore of the utmost importance to control the steric factors when modifying a ligand, so to hinder reactivity.

Spin is another variable of considerable interest in iron(IV)-oxo reactivity as enzymatic intermediates have an $S = 2$ spin state, while most synthetic iron(IV)-oxo species have an $S = 1$ spin state.[17] The high-spin state found in nature is predicted to be

more reactive based on exchange-enhanced reactivity.[18] With the exchange-enhanced reactivity, same spin electrons are stabilized by exchange energy. As seen in Scheme 1.6 there is greater exchange energy in the product, but the opposite is true for Scheme 1.7. This exchange is balanced by the d-orbital splitting, which forces electrons to pair up if the splitting energy is too large. The high-spin complexes benefit from the smaller splitting by allowing the d_{z^2} orbital to be the orbital involved in hydrogen atom abstraction. Upon breaking a C-H or O-H bond, the electron obtained is able to occupy the d_{z^2} orbital and have the same spin as the other electrons (Scheme 1.6). This stabilizes the product as compared to the product of the $S = 1$ spin state (Scheme 1.7).

Some iron(IV)-oxo complexes have been synthesized with an $S = 2$ spin state. One way to generate an $S = 2$ spin state synthetically is to use a ligand that enforces trigonal bipyramidal geometry (Scheme 1.8). This strategy allowed the $d_{x^2-y^2}$ and the d_{xy} orbitals to become degenerate (Scheme 1.9), as compared to a pseudo-octahedral complex, preventing the $S = 1$ spin state from being achieved. While the TMG_3-tren ligand was the first to employ this strategy, several complexes have been subsequently synthesized based on this idea.[19–22] Unfortunately, the steric constraints of the ligand made the iron(IV)-oxo species very slow to react with bulky substrates.[19] While 9,10-dihydroanthracene (DHA) and 1,4-cyclohexadiene (CHD) have similar bond dissociation energies, the reaction of the iron(IV)-oxo complex with CHD is over 10 times faster than the reaction with DHA, indicating the bulkier DHA is prevented from accessing the oxo moiety as readily as CHD. This was also seen with the iron(IV)-oxo complex with tpa^{Ph} as the ligand.[20] However, a modified version of TMG_3-tren, which is missing the third arm, not only allowed an open site *cis* to the oxo, but increased reactivity by an order of magnitude.[21] Therefore, sterics were a major reactivity factor in this class of complexes.

Scheme 1.3: Hydrogen atom transfer (HAT) example with $[Fe(O)TMC(NCCH_3)]^{2+}$ and a generic substrate.

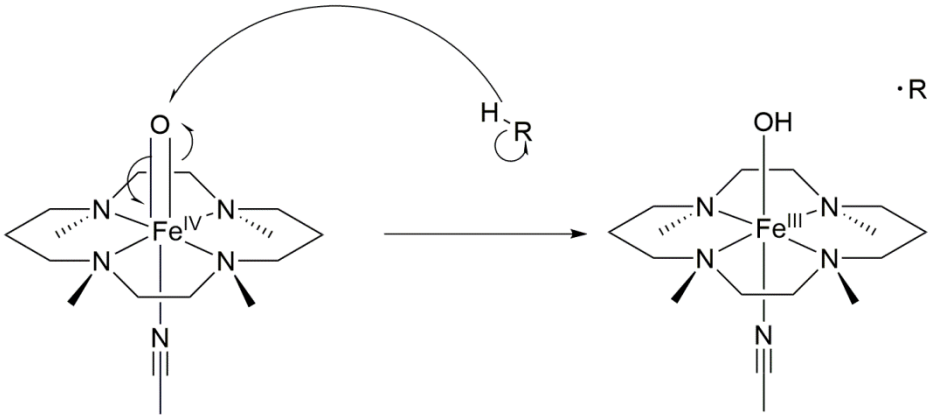

Scheme 1.4: Oxygen atom transfer (OAT) example with $[Fe(O)TMC(NCCH_3)]^{2+}$ and PPh_3.

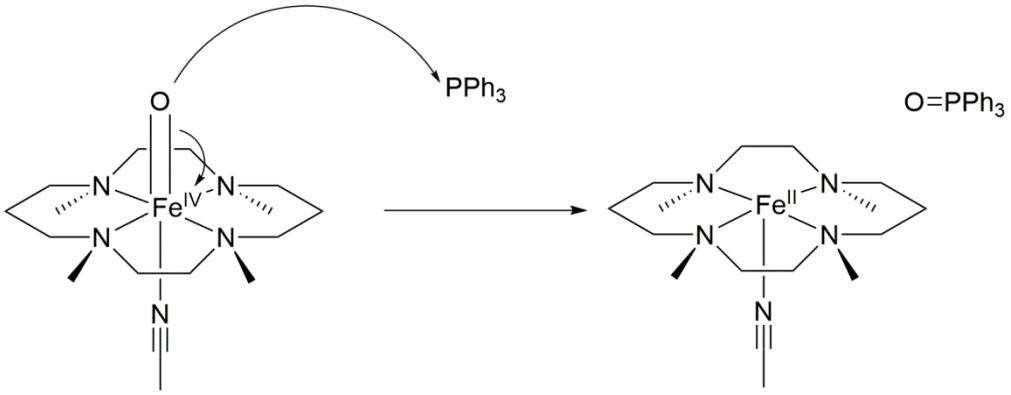

Scheme 1.5: Space-filling model of the proposed $[Fe(O)(Tp^{Ph2})(BF)]$ Reprinted with permission from Mukherjee, A.; Martinho, M.; Bominaar, E. L.; Münck, E.; Que, L. *Angewandte Chemie* **2009**, *121* (10), 1812–1815. Copyright © 2009 John Wiley and Sons.

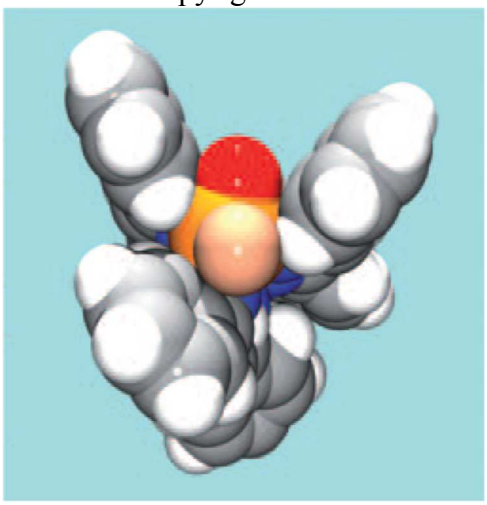

Scheme 1.6: An *S* = 2 iron(IV)-oxo complex reacts with a C-H bond. The product has all electrons with the same spin, which enhances the stability of the complex. Modified from Shaik *et al*.[18]

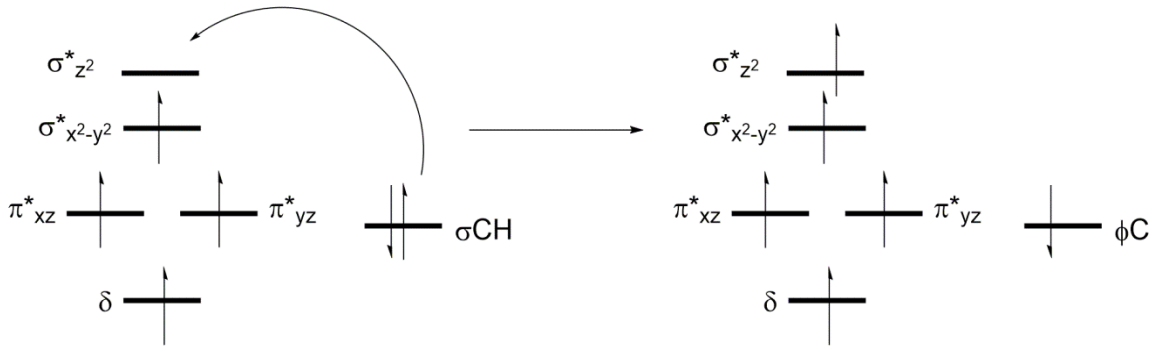

Scheme 1.7: An *S* = 1 spin iron(IV)-oxo complex reacts with a C-H bond. The π* orbital interacts with the bond instead of the d_{z2} orbital, as in the *S* = 2 case. The molecule is less stable due to lowering of the exchange energy. Modified from Shaik *et al*.[18]

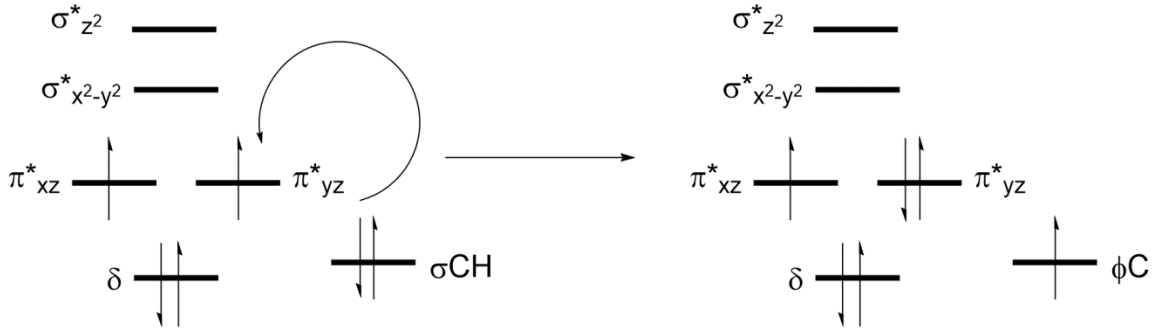

Scheme 1.8: Synthetic high-spin iron(IV)-oxo complexes with ligands that enforce trigonal bipyrimidal geometry.

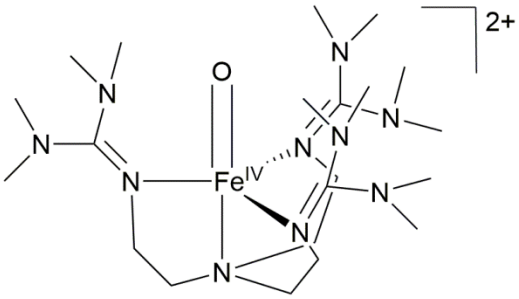

Fe(O)TMG$_3$-tren

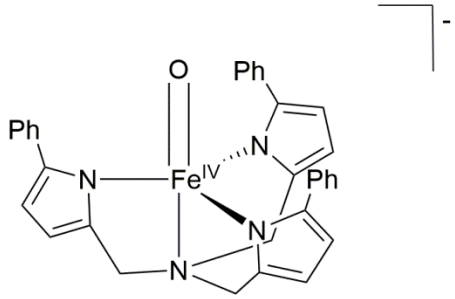

Fe(O)tpa^{Ph}

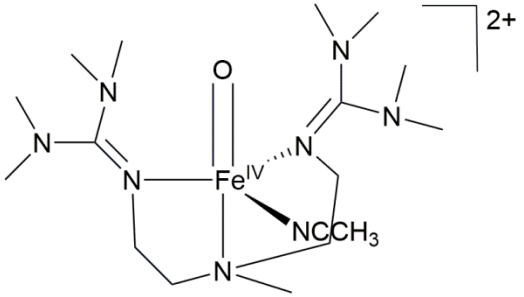

Fe(O)TMG$_2$-dien

Scheme 1.9: The orbital splitting diagram of the d-orbitals for pseudo-octahedral (left) and trigonal bipyramidal (right) geometries.

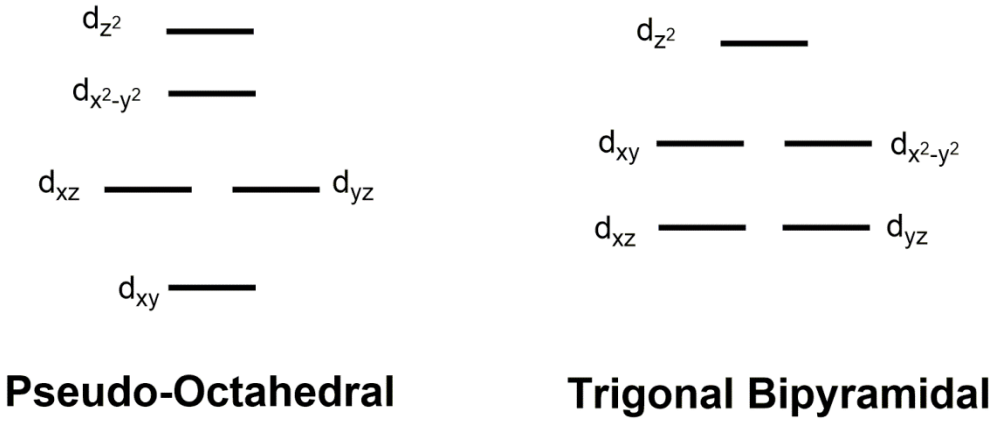

Scheme 1.10: Synthetic iron(IV)-oxo complexes with similar ligand structures, but different spin states. $[Fe^{IV}(O)(TQA)(NCMe)]^{2+}$ is $S = 2$, while $[Fe^{IV}(O)(Me_3NTB)(NCMe)]^{2+}$ is $S = 1$.

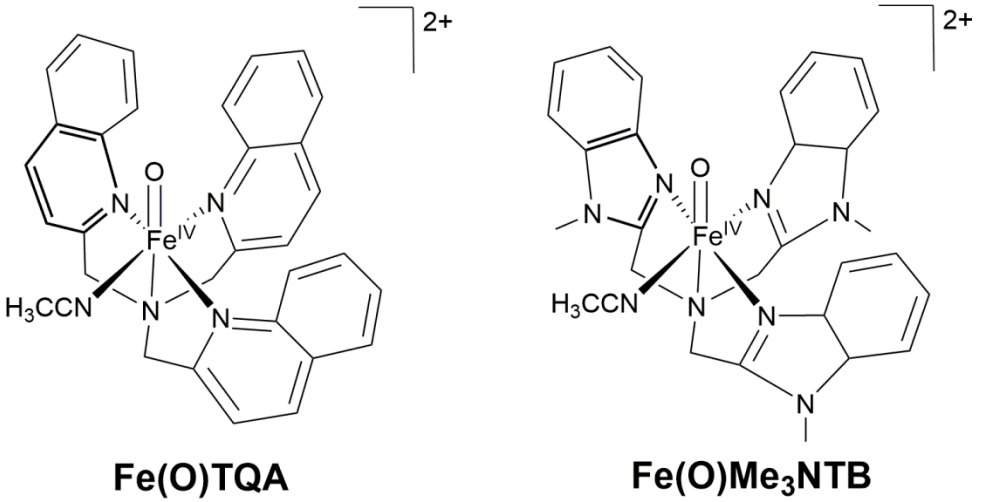

To avoid these steric issues, a pseudo-octahedral iron(IV)-oxo complex, $[Fe^{IV}(O)(TQA)(NCMe)]^{2+}$, was synthesized with an open site *cis* to the oxo.[23] This complex has an $S = 2$ state, like those of the enzymatic iron(IV)-oxo intermediates, and is very reactive compared to most $S = 1$ complexes. However, a similar complex, $[Fe^{IV}(O)(Me_3NTB)(NCMe)]^{2+}$, has an $S = 1$ ground state was characterized and has very similar reactivity.[24] There is a proposal that the $S = 1$ complex has a low-lying $S = 2$ state that may affect the reactivity. However, the similar reactivity of these complexes calls into question whether high-spin complexes are truly more reactive.

Another major component of reactivity of iron(IV)-oxo species that has been investigated is the effect of electron donation from the ligands. This is based not only on what ligands are bound, but where they are bound. For instance, $[Fe^{IV}(O)(L^8py_2)]^{2+}$ has a site *trans* to the oxo moiety that is occupied by solvent, whereas $[Fe^{IV}(O)(TPA)]^{2+}$ has a site *cis* to the oxo moiety that is occupied by solvent (Scheme 1.11). Upon the addition of pyridine N-oxides, the solvent is replaced by this new ligand.[25] The comparison of HAT reactivity of *cis* vs. *trans* ligand replacements indicated the position of the ligand affects the reactivity in different ways. The *cis* ligands simply affect Lewis acidity of the iron(IV)-oxo moiety, while *trans* ligands may have influenced the iron(IV)-oxo bond strength, as more electron-donating ligands increased reactivity .[25]

Another study showed that the more electron-donating *trans* ligands of TMC-based complexes led to complexes that were more reactive.[26] A study of four iron(IV)-

Scheme 1.11: Iron(IV)-oxo complexes used to compare the reactivity of changing ligand at the site *cis* to the oxo versus *trans*.

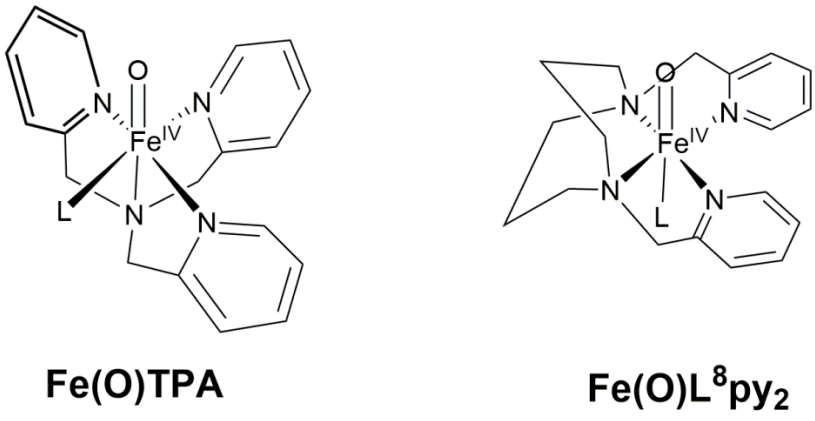

oxo complexes using the TMC framework had four different axial ligands: CH_3CN, CF_3COO^-, N_3^-, and RS^- (Scheme 1.12). The most electron-donating ligand, RS^-, resulted in the slowest rate for oxygen atom transfer, but the fastest rate for HAT. A trend was seen between reaction rate and reduction potential of all complexes: OAT reactivity followed an electrophilic trend, while HAT followed an anti-electrophilic trend.

The anti-electrophilic trend was explained by the two-state reactivity (TSR) model. This model has many incarnations, which will be explored in chapters 2 and 3; however, a brief description will be given here. The iron(IV)-oxo complexes having an $S = 1$ ground spin state may be able, according to the TSR model, to access an $S = 2$ spin state, either as a cross-over to the $S = 2$ transition state, or by a blending of the two barriers. The gap between the reactant ground $S = 1$ state and the $S = 2$ state is determined by the donating properties of the ligands. More electron-donating axial ligands were calculated to have smaller gaps between the $S = 1$ and $S = 2$ state, thereby increasing their reactivity.

The modification need not be simply to the axial ligand. Changing the methyl groups to benzyl groups to create tetrabenzylcyclam increased HAT reactivity ~150-fold of $[Fe^{IV}(O)TBC(CH_3CN)]^{2+}$ from $[Fe^{IV}(O)TMC(CH_3CN)]^{2+}$.[27] The distortion caused by the benzyl groups increased the bond length of both the axial iron-acetonitrile and the equatorial Fe-N bonds. This stabilized both the d_{x2-y2} orbital and the d_{z2} orbital, which in turn decreased the gap between the $S = 1$ and $S = 2$ states. $[Fe^{IV}(O)TBC(CH_3CN)]^{2+}$ was explained to be more reactive because of this smaller gap between the two states, which allowed for a lower energy transition state.

Scheme 1.12: Cyclam-based iron(IV)-oxo complexes used in various studies.

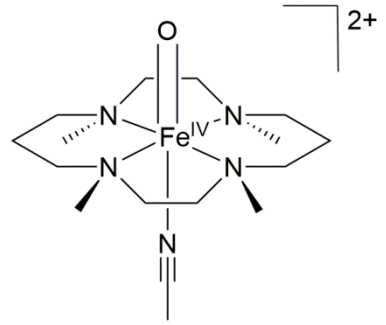

Fe(O)TMC(NCCH$_3$)

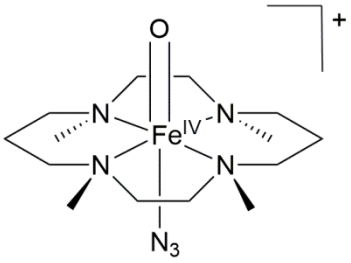

Fe(O)TMC(N$_3$)

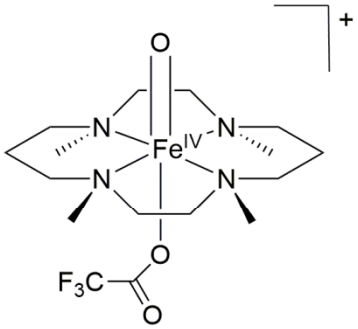

Fe(O)TMC(OOCCF$_3$)

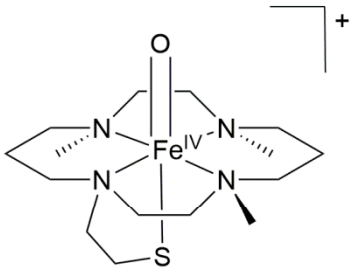

Fe(O)TMCS

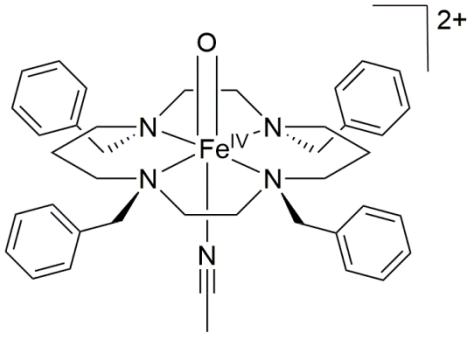

Fe(O)TBC(NCCH$_3$)

The TSR model aided in the explanation of much of iron(IV)-oxo reactivity towards HAT. However, there were a few examples that did not fit the model. A series of pentadentate iron(IV)-oxo complexes actually increased in HAT rate with increasing reduction potential,[28] counter to what had been seen in the $[Fe^{IV}(O)TMC(X)]^{2+}$ case. Also, with the ligand BQCN, there are two different topologies. The more reactive iron(IV)-oxo complex had the higher reduction potential (Scheme 1.13).[29] As will be explored in chapters 2 and 3, the TSR model may not be able to account for all HAT reactivity seen with iron(IV)-oxo complexes, which calls into question how relevant the high-spin $S = 2$ state is to reactivity.

Scheme 1.13: Iron(IV)-oxo complexes with different topologies, but the same BQCN ligand.

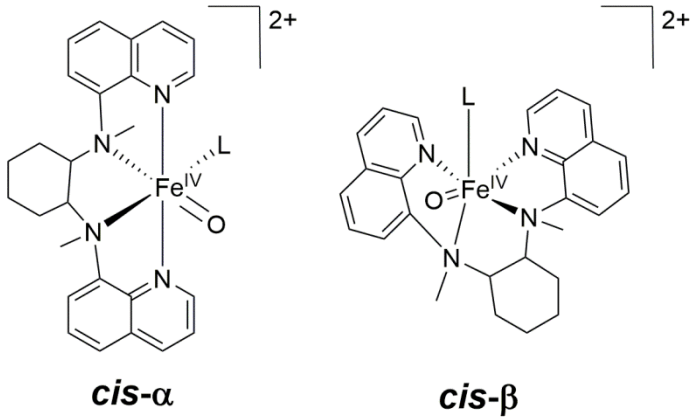

1.2.2 Synthetic Iron-peroxo to Iron(IV)-oxo Mechanisms

While the iron(IV)-oxo species is the reactive intermediate in many nonheme iron enzymatic cycles, how this species forms is just as important for understanding reactivity as the hydrogen abstraction step performed by the iron(IV)-oxo moiety. Synthetic model complexes form iron(IV)-oxo species, utilizing either hydrogen peroxide or oxygen as the oxygen atom source.

One iron complex that purports to mimic an iron heme enzyme, horseradish peroxidase, is $[Fe^{II}(TMC)]^{2+}$. Interestingly, upon addition of a single equivalent of hydrogen peroxide and pyridine, nearly quantitative yield of $[Fe^{IV}(O)(TMC)]^{2+}$ formed.[30] This was proposed to be due to a proton being shuttled from the oxygen bound to the iron

to the terminal oxygen, allowing for heterolytic cleavage to occur (Scheme 1.14). The requirement of base is similar to how horseradish peroxidase has an imidazole in the active site proposed to participate in the same proton shuttle mechanism.

Generation of side-on peroxo complexes has also been achieved. Two different groups confirmed that $[Fe^{III}(OO)(TMC)]^{2+}$ could be synthesized.[31,32] This complex was protonated to form an end-on hydroperoxo species, which then formed $[Fe^{IV}(O)(TMC)]^{2+}$ (Scheme1.15). However, depending on the solvent, heterolytic or homolytic cleavage could occur. In acetonitrile, the conversion of $[Fe^{III}(OOH)(TMC)]^{2+}$ to $[Fe^{IV}(O)(TMC)]^{2+}$ upon the addition of perchloric acid showed a first-order dependence.[31] Conversely, the same conversion in a 3:1 acetone:trifluoroethanol mixture showed no dependence on acid concentration.[32] A similar reaction also occurred with Lewis acids used in the place of a proton source.[33,34] The addition of the Lewis acid formed side-on peroxo species with the Lewis acid bound to the peroxo moiety. $[Fe^{IV}(O)(TMC)]^{2+}$ was still able to form, as long as there was an electron source.

Recently, $[Fe^{II}BDPP]$ has been shown to react with oxygen to form an iron(III)-superoxo species.[35] This assignment was aided by resonance Raman, which showed a vibration at 1125 cm^{-1} that shifted to 1062 cm^{-1} upon ^{18}O-labeling. Interestingly, this iron(III)-superoxo species reacted with 9,10-dihydroanthracene. The reaction had a KIE of 7, indicating that the HAT was the rate determining step. This may produce an iron(III)-peroxo species as an intermediate; studies are underway to characterize the products to see an iron(IV)-oxo species forms.

Oxygen was also a source for potential peroxo formation. While not directly trapped or characterized, peroxo species were proposed to form when $[Fe^{II}(TMC)]^{2+}$ was exposed to dioxygen and either an acid source and an electron source,[33,36,37] or a hydrogen atom donor.[38] In the case of the acid and electron source, two different electron sources could be used: BNAH, an NADH mimic, or a tetraphenylborate salt. Both scandium triflate and perchloric acid were used with tetraphenylborate salts to generate $[Fe^{IV}(O)(TMC)]^{2+}$. These were previously proposed to form an iron(III)-peroxo species before undergoing O-O bond cleavage to form the iron(IV)-oxo species (Scheme 1.12). A similar reaction was proposed for the hydrogen atom source, which was cycloalkenes.

However, the scandium and tetraphenylborate reaction was recently reported to generate peroxide radicals, which were the main source of $[Fe^{IV}(O)(TMC)]^{2+}$ formation.[39] Both the proton-coupled electron transfer and hydrogen atom transfer mechanisms are reevaluated in chapter 4.

Scheme 1.14: Proposed reaction mechanism for the reaction of $[Fe^{II}TMC]^{2+}$ to produce the iron(IV)-oxo complex

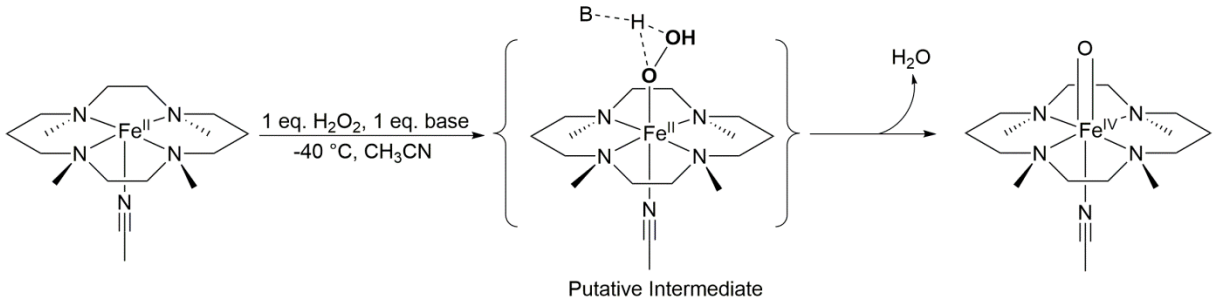

Scheme 1.15: Proposed mechanism for reaction of $[Fe^{III}(OO)(TMC)]^{2+}$ with a proton to form $[Fe^{IV}(O)TMC]^{2+}$.

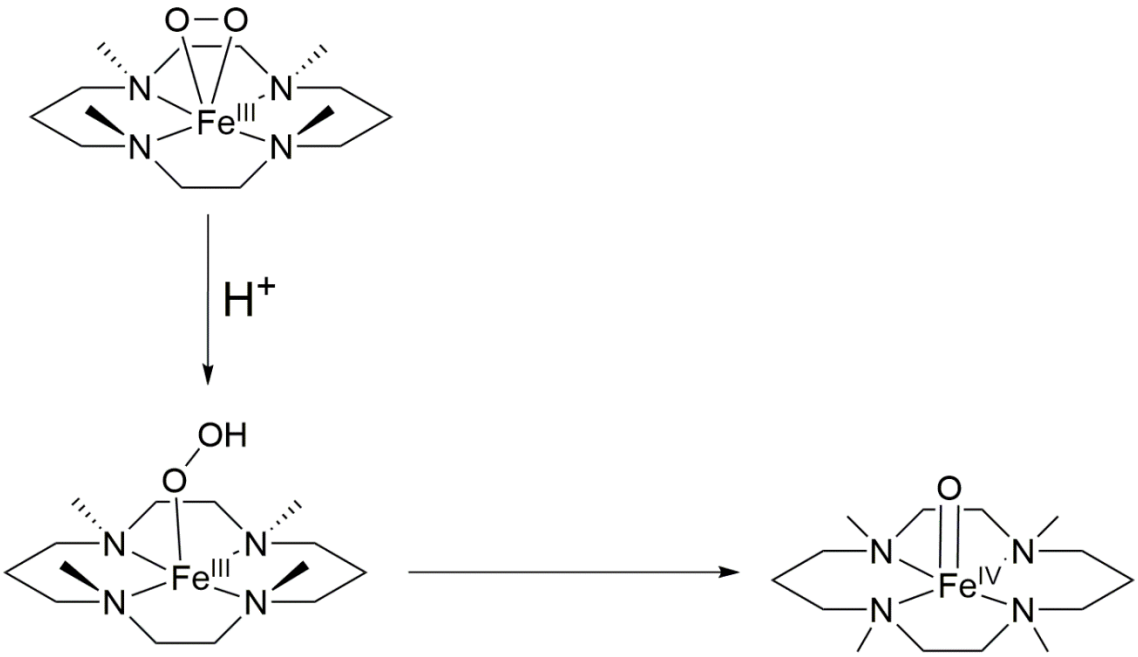

Scheme 1.16: Previously proposed oxygen activation mechanism.

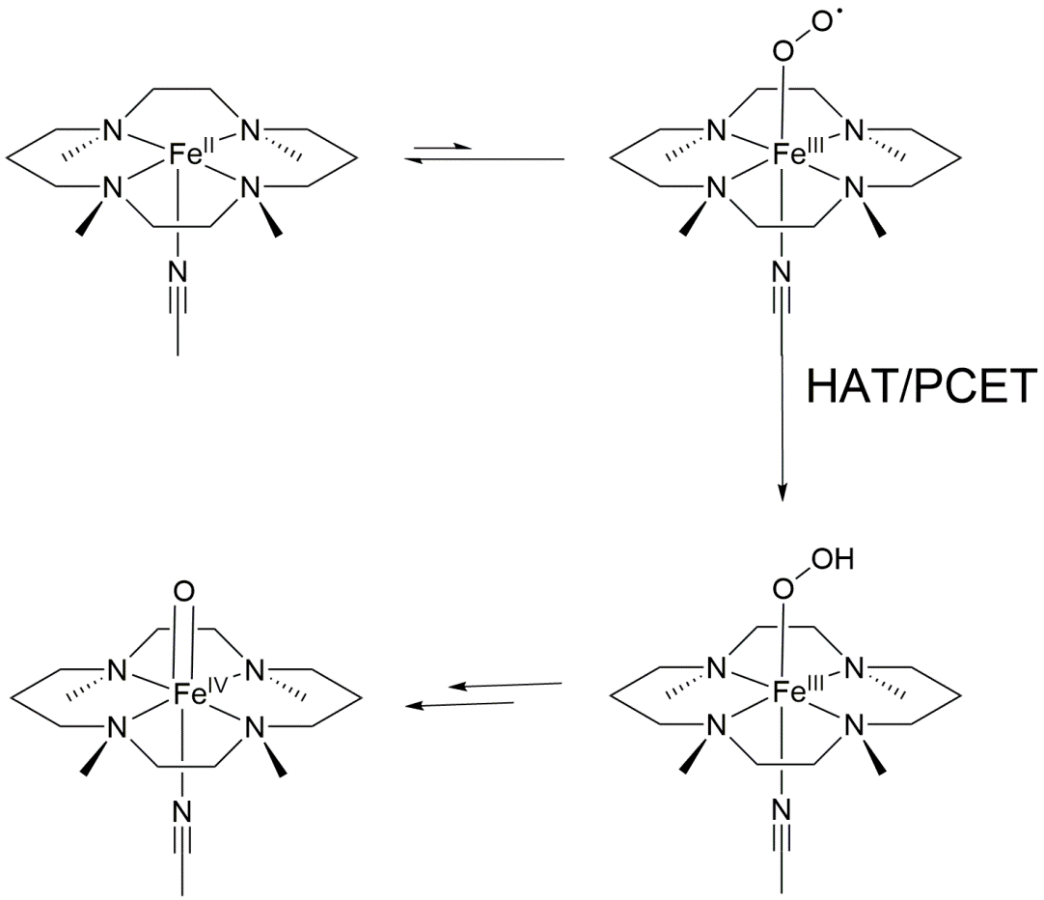

1.3 Scope and Aims of Thesis

This thesis explores the properties of synthetic complexes, lending insight to the biological community for factors to consider in enzymes, as well as spurring new insights for the synthetic community.

The aim of this thesis is to elucidate what factors affect the reactivity of synthetic iron(IV)-oxo complexes, what mechanism allows for oxygen to react to form iron(IV)-oxo complexes, and how biologically-relevant complexes can be characterized and compared using resonance Raman spectroscopy.

The focus of chapter 2 is the reactivity of iron(IV)-oxo conjugate acid-base pairs. Using very similar systems, which only vary in electronics, allows us to test one factor and how this changes reactivity. Interestingly, although the complexes vary widely in the electron-donating ability of the axial ligand, their reactivity in hydrogen atom abstraction changes insignificantly.

Chapter 3 focuses on axially-bound carboxylate iron(IV)-oxo species, some of which have the axial ligand tethered to the main ligand framework. Although the axial ligands have very similar electron-donating abilities, as verified by cyclic voltammetry, the rate constants vary by approximately 100-fold for both HAT and OAT.

Chapter 4 re-examines the mechanisms of oxygen activation. Instead of first reacting with the iron as previous proposed, this work suggests that dioxygen reacts with the different substrates to form peroxyl radicals. These radicals are trapped by the iron(II) complex, which allows for the formation of iron(IV)-oxo species.

Resonance Raman spectroscopic investigations are the focus of chapter 5. The characterization of these complexes aids the understanding of how synthetic iron-oxo complexes form, why certain metals are prevalent in biology, and the properties of new, bioinspired complexes.

Chapter 2

Electrochemistry and Reactivity of Oxoiron(IV) Conjugate Acid-Base Pairs

Part of this work appeared in: England, J.; Bigelow, J. O.; Heuvelen, K. M. V.; Farquhar, E. R.; Martinho, M.; Meier, K. K.; Frisch, J. R.; Münck, E.; Que, L. *Chem. Sci.* **2014**, *5*, 1204–1215.

2.1 Introduction

Iron(IV)-oxo species are implicated as the reactive intermediate in a wide array of non-heme iron-containing mononuclear enzymes.[2,40] Iron(IV)-oxo intermediates have been trapped in several enzymes,[4,6,7,9,12,13] and are proposed to react with substrate by abstracting a hydrogen atom from a C-H bond, the crucial step for product formation.[40] Given this, the importance of understanding the factors that affect the reactivity of the iron(IV)-oxo moiety are clear: understanding how enzymes tune the iron(IV)-oxo moiety aids in elucidating the key step of hydrogen atom transfer (HAT).

However, iron(IV)-oxo intermediates in the enzymes are unstable and the enzyme framework is not easily modified, unlike synthetic systems. Synthetic systems can vary factors like electronics, sterics, and spin state systematically to investigate the reactivity of iron(IV)-oxo moieties.

Even with this ability to vary different factors, understanding the reactivity of synthetic iron(IV)-oxo complexes has proved complicated. The most systematic study of iron(IV)-oxo reactivity in complexes with similar ligand structures employed TMC-based ligands for Fe^{IV}(O)TMC(X), where X was a ligand coordinating trans to the oxo moiety.[26] As expected, the oxygen atom transfer (OAT) reactivity trend of increasing rate constants with increasing reduction potential, which was due to the two-electrons that must be transferred in OAT, was consistent with other the synthetic systems studied. In contrast to OAT, an anti-electrophilic trend was observed for HAT, which was explained using a two-state reactivity (TSR) model. This model states that there is greater contribution of the lower-lying $S = 2$ state when there is a smaller the gap between the $S = 1$ state and $S = 2$ state in the reactant. The difference in energy of these states is controlled by the ligand environment. In Fe^{IV}(O)TMC(X) complexes, this is controlled by the change of the axial ligand X. More electron donating ligands decrease the gap between the $S = 1$ state and the $S = 2$ state, which, if this correlates with a decrease in the spin-inversion probability, would account for the anti-electrophilic trend.[41] The quintet transition state is lower in energy than the triplet, so the greater the contribution of the $S = 2$ state would lower the overall energy required for H-atom transfer.

Scheme 2.1: Conjugate acid-base pairs with TMC-based ligands used in this study.

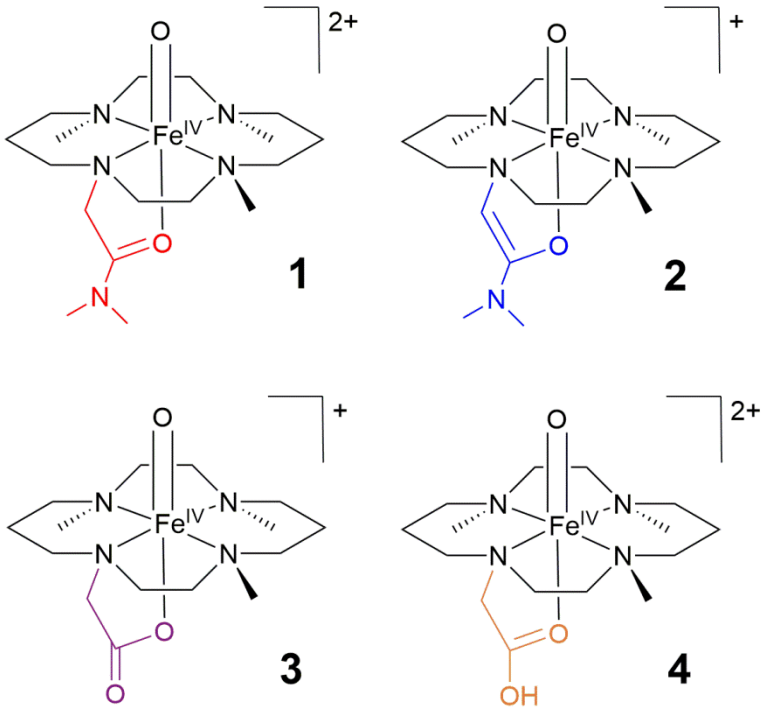

Scheme 2.2: Iron(IV)-oxo complexes also used in this study.

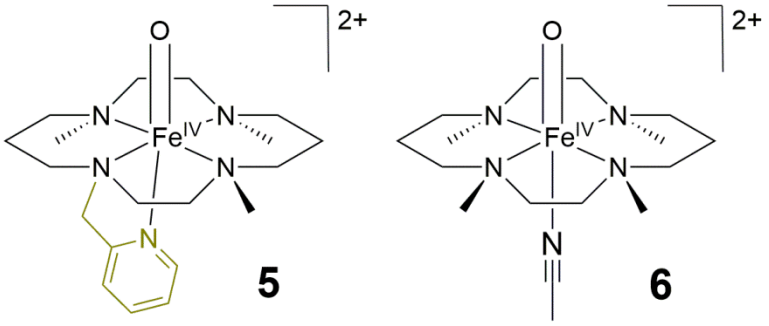

In a subsequent study with pentadentate iron(IV)-oxo complexes reported by Wang *et al.*, the HAT reactivity increased with increasing redox potential.[28] This is not an isolated case: Hong *et al*. reported higher HAT and OAT rates for the cis-α $[Fe^{IV}(O)(BQCN)]^{2+}$ than the cis-β $[Fe^{IV}(O)(BQCN)]^{2+}$ complex, where the α-complex was shown to have a higher redox potential than the β-complex.[29] These results suggest that the TSR model may not be universally applicable.

Given the lack of a consistent trend in the HAT reactivity and reduction potential of synthetic iron(IV)-oxo complexes, a larger series that investigated a similar ligand framework would aid in clarifying the factors that affect HAT rates. The earlier TMC-based study[26] varied the potential by switching the axial ligand, it was complicated by several factors: the tethering, or lack thereof, of the axial ligand to the TMC-framework; change in the solvent systems used; and the type of the atom coordinated to the iron at the axial position. To minimize these problems, iron(IV)-oxo complexes with very similar TMC-based ligands were synthesized. Herein we report our investigations of two sets of iron(IV)-oxo complexes were that are conjugate acid-base pairs; these species are the first reported. Complex **1** can be deprotonated with a base to form **2**, while **3** can be protonated to form **4**. These pairings allow for the comparison of iron(IV)-oxo complexes that vary little with respect to the ligand framework, keeping structure nearly constant, including the atoms coordinated to the iron center. With these complexes in hand, the TSR model can be effectively tested without complicating factors.

2.2 Experimental

2.2.1 General Methods

All reagents were purchased from Sigma-Aldrich, unless otherwise noted. Iodosylbenzene was synthesized by a previously published method.[42] The ligand for **1**, **3**, and **5** were synthesized using previously published methods.[36,43–46] $Fe(OTf)_2(CH_3CN)_2$ was synthesized using previously published methods.[47] TMC was purchased from Angene International Limited or Strem. The iron(II) precursor to **5** was prepared using the published method.[36] The iron(II) precursor to **6** was generated by a modification of the previously reported method.[48] Generally, 1 mmole of $Fe(OTf)_2(CH_3CN)_2$ was

dissolved in dichloromethane with 1 mmole of TMC. This was stirred for 2-3 hours before being filtered into diethyl ether. A precipitate formed immediately. The solution was filtered and the solid collected. The solid was dissolved in dichloromethane and set up for vapor diffusion with diethyl ether in a -40 °C freezer. After several days, the solution was filtered and the solid collected. A typical yield was 64%. Triphenylphosphine was purified by dissolving in hexane and running through a silica gel column. Ferrocene, decamethylferrocene, and cobaltocene were purified by sublimation.

2.2.2 Instrumentation

A BAS 100B/W Electrochemical Analyzer potentiostat was used for all cyclic voltammetry experiments. All electronic spectra were obtained using a HP8453A diode array spectrometer equipped with a cryostat from Unisoku Scientific Instruments (Osaka, Japan). ^{1}H NMR was carried out on Varian Inova 500 MHz, 300 MHz or Bruker AV-500 and referenced to residual solvent peaks. ^{31}P NMR were carried out on a Bruker AV-500. All resonance Raman species were collected Spectra-Physics Model 2060 Kr^{+} laser with an Action AM-506 monochromator equipped with a Princeton LN/CCD data collection system,

2.2.3 Complex Synthesis

Syntheses originally conducted by Jason England, except for attempts to generate **4**. Synthesis of **3** was based on my data using Dr. England's method.

$[Fe^{II}(Me_3cyclam\text{-}CH_2C(O)NMe_2)](OTf)_2$ (precursor to **1**): A mixture of $Me_3cyclam\text{-}CH_2C(O)NMe_2$ (0.34 g, 1.04 mmol), $Fe(OTf)_2(CH_3CN)_2$ (0.46 g, 1.04 mmol) and THF (10 mL) was stirred overnight. The pale green precipitate that formed during this time was isolated by filtration, washed with THF (2 × 5 mL) and diethyl ether (20 mL), and dried under vacuum to give the product as a cream-colored solid (0.49 g, 69%). Crystals suitable for X-ray analysis were grown by vapor diffusion of diethyl ether into a concentrated acetonitrile solution of complex. ^{1}H-NMR (CD_3CN, 293 K, all peaks appear as broad singlets): δ390.0 (1H, CH_2), 376.5 (1H, CH_2), 338.8 (1H, CH_2), 314.7 (1H, CH_2), 251.2 (1H, CH_2), 207.6 (1H, CH_2), 195.6 (1H, CH_2), 171.1 (1H, CH_2), 168.4 (1H, CH_2), 108.4 (3H, N*Me*), 105.5 (1H, CH_2), 103.6 (3H, N*Me*), 98.5 (4H, N*Me* + CH_2), 101.9 (1H, CH_2), 79.9 (1H, CH_2), 50.5 (3H, N*Me*), 34.8 (1H, CH_2), 17.3 (1H, CH_2), 12.4

(4H, N*Me* + C*H*$_2$), 7.5 (1H, C*H*$_2$), -4.0 (1H, C*H*$_2$), -16.9 (1H, C*H*$_2$), -34.5 (1H, C*H*$_2$), -36.8 (1H, C*H*$_2$), -97.3 (1H, C*H*$_2$). MS (+ESI): *m/z* 532.1 [(M-OTf)$^+$]. Anal. Calcd. (found) for $C_{19}H_{37}F_6FeN_5O_7S_2$: C, 33.49 (33.51); H, 5.47 (5.52); N, 10.28 (10.11).

[Fe^{II}(Me_3cyclam-CH_2COO)][$B(C_6F_5)_4$] (precursor to **3**): The ligand precursor Me_3cyclam-CH_2COOH·4HCl (0.6246 g, 1.4 mmole) was neutralized with sodium methoxide (0.3025 g, 5.6 mmole) in methanol and stirred for 15 minutes. The solvent was removed by rotary evaporation, and then dichloromethane was added. After stirring, the solution was filtered. The solvent was removed by rotary evaporation and dried by vacuum. Under a nitrogen atmosphere, methanol, $Fe(OTf)_2(CH_3CN)_2$ (0.5571 g, 1.3 mmol) and trimethylamine (0.85 mL, 6.1 mmol) were added and stirred overnight. Lithium tetrakis(pentafluorophenyl)borate diethyl ether complex (0.9667 g, 1.3 mmol) was added and a precipitate formed. The solid was filtered and washed with diethyl ether. Yield 23%. ^{1}H NMR(CD_3CN, 293 K, all peaks appear as broad singlets): δ337.7, 332.5, 321.8, 189.4, 163.4, 149.8, 144.7, 133.5, 103.1, 95.9, 88.3, 80.2, 60.4, 24.9, 7.9, -0.3, -14.3, -29.4, -54.5.

Attempts at generating [Fe^{II}(Me_3cyclam-CH_2COO)][$B(C_6F_5)_4$] (precursor to **4**): In all attempts, the ligand precursor Me_3cyclam-CH_2COOH·4HCl was neutralized with NaOMe as in the synthesis above. Addition of $Fe(OTf)_2(CH3CN)_2$ in methanol and precipitation with either $NaBPh_4$ or lithium tetrakis(pentafluorophenyl)borate diethyl ether complex did not yield the expected iron(II) species, but rather seemed to yield the precursor to **3**. If the solvent was removed instead of attempting to precipitate the complex, a similar species was formed. Iron(II) chloride in place of $Fe(OTf)_2(CH_3CN)_2$ with acetonitrile instead of methanol formed a slurry to which $AgSbF_5$ was added. A precipitate formed, which was filtered from the solution. The solution was put in a -40 °C freezer over two days and filtered. The filtrate solvent was removed by vacuum. Testing by iodosylbenzene formed a species that was not **4**.

Complexes **1** and **3** were generated in acetonitrile with the appropriate Fe(II) precursor using an excess (~3x) of iodosylbenzene, stirred for approximately 15 minutes, and then was filtered prior to use, a method developed by Dr. Jason England.

Generation of **2** was accomplished by addition of NBu_4OH or NBu_4OMe to **1**. The quantity of NBu_4OH added equates to the minimum amount required for full conversion of **1** to **2**, which was established by titration at -40 °C using electronic spectroscopy. Conversion of **3** to **4** was accomplished by addition of a solution of perchloric acid to **3**.

2.2.4 Cyclic Voltammetry

All cyclic voltammetry experiments were performed either inside a nitrogen atmosphere glove box, or under a positive pressure of argon in a vial sealed with a septum. Acetonitrile solution containing 0.1 M tetrabutylammonium hexafluorophosphate (NBu_4PF_6) as the electrolyte, a glassy carbon working electrode, a platinum wire counter electrode, and a Ag^+/Ag reference electrode were used throughout. The latter was prepared by inserting a Ag wire into an acetonitrile solution of 0.1 M NBu_4PF_6 and 0.01 M $AgPF_6$ contained within a glass tubing capped with a porous vycor tip and heat shrink tubing (BASi, Inc., West Lafayette, IN, USA, part no. MF-2064). Temperature was maintained using a methanol/liquid nitrogen bath for -40 °C experiments. All scans were conducted at 100 mV/s unless otherwise noted. All potentials are referenced against the ferrecenium/ferrocene (Fc^+/Fc) couple.

2.2.5 Titrations

Stock solutions of Fc, Fc*, and $CoCp_2$ were prepared. Varying amounts of these solutions were added solutions of iron(IV)-oxo species in CH_3CN. The solution was allowed to equilibrate based on absorption features detected by the UV-vis spectrometer. These were plotted using methods mentioned previously.[49,50]

2.2.6 Reaction Kinetics

Kinetic reactions with PPh_3 were conducted by Jason England.

All kinetic studies were performed under a nitrogen atmosphere. Acetonitrile solutions were prepared of 0.5 mM (**1** and **3**) or either 1 mM (**5**). The yields of oxoiron(IV) complex were assessed using electronic spectroscopy and found to be near quantitative based on molar absorptivities calculated from Mössbauer results. Generation of **2** was achieved by addition of 1.2-1.3 equivs of NBu_4OH dissolved in dry CH_3CN (0.1 mM solution) relative to iron concentration. Generation of **4** was accomplished by addition of 1.4 eq. perchloric acid to **3**, the amount established necessary for full

conversion at 0 ˚C. Dichloromethane solutions of the substrates PPh_3, $PMePh_2$, thioanisole, and 1,4-cyclohexadiene (CHD) were added in > 10-fold excess to solution of the aforementioned oxoiron(IV) complexes at 0 °C. The resulting reactions were monitored by decay of their respective near-IR features and some were found to display pseudo-first order kinetics. Data was fit with an exponential fit macro using Origin software. Plots of effective rate constants (k_{eff}) *vs*. substrate concentration were found to be linear in all cases, thereby yielding second order rate constants (k_2).

2.2.7 Product Analysis

In order to determine the products from kinetic reactions, solutions of **1** and **2** at 0.5 mM and 2 mM were generated in CD_3CN and the reaction carried out at 0 °C. The ^{31}P NMR delay time was lengthened to 30 seconds to allow for proper integration of the phosphorus peaks. A sample with just CD_3CN and organic reactant was used to account for any amount of product already present in the starting material in all cases. The products generated were compared with the concentration of iron(IV)-oxo species generated based on the absorbance at each respective λ_{max} with UV-vis spectroscopy to determine yield.

2.2.8 Resonance Raman Spectroscopy

Spectra of **1** and **2** were collected by Johnathan Frisch and Kathy Van Heuvelen.

Resonance Raman experiments were conducted using a laser line of 406.7 nm at 20-30 mW of power or 568.2 nm at ~90 mW of power. Both lines were calibrated to indene. Generation of **1** and **3** was accomplished by the mixing of excess iodosylbenzene or ^{18}O-labeled iodosylbenzene with the iron(II)-precursor, which was then frozen on a cold finger. A similar method to generate was used to generate **4**, with the additional step of adding 2 eq. perchloric acid to **3** to generate **4** before freezing. The cold finger was evacuated and kept cold with liquid nitrogen. These samples were rastered as photodecay has been noted to be an issue with iron(IV)-oxo complexes with such a high energy laser.

Species **2** could not be generated in the same manner, so instead anhydrous NBu4OMe methanol solution was added to an acetonitrile solution of **1** cooled to -44 °C. At -20 °C in a flat-bottomed NMR tube, a resonance Raman spectrum could be obtained.

2.2.9 Mössbauer Spectroscopy

Data was collected and analysed by Marlène Martinho and Eckard Münck.

The Mössbauer spectra were recorded with a home built spectrometer, using a Janis Research (Wilmington, MA) Super Varitemp dewar. Isomer shifts are quoted relative to Fe metal at 298 K

Frozen solution samples of **2** suitable for Mössbauer spectroscopy were generated in butyronitrile solution at -60 °C, by addition of 2.5 – 5 equiv of a 0.2 M toluene solution of $NOct_4OH$.

2.2.10 X-ray Absorption Spectroscopy

Data was collected and analyzed by Erik Farquhar and Greg Rohde.

X-ray absorption data was collected on beamlines 9-3 (**1**, 7 scans, 16 mM, quantitative yield by UV/Vis) and 7-3 (**2**, 15 scans, 6.94 mM, yield of 90% by UV/Vis) of the Stanford Synchrotron Radiation Lightsource (SSRL) of SLAC National Accelerator Laboratory with storage ring conditions of 3.0 GeV and 80 – 100 mA. Fe K-edge XAS data were collected for frozen solutions maintained at a temperature of *ca.* 15 K over an energy range of 6.9 – 8.0 keV using a Si(220) double crystal monochromator for energy selection and an Oxford Instruments CF1208 continuous flow liquid helium cryostat for temperature control. Harmonic rejection was achieved at both beamlines using a vertically collimating Rh-coated mirror located upstream of the monochromator. Data were obtained as fluorescence excitation spectra with a 30-element solid-state germanium detector array (Canberra). An iron foil spectrum was recorded concomitantly for internal energy calibration and the first inflection point of the K-edge was assigned to 7112.0 eV. The edge energies of the XAS samples were routinely monitored during data collection for red-shifts indicative of photoreduction. While **1** exhibited no evidence for photoreduction, a red-shift of ~0.5 eV was observed for **2** when a single spot was exposed to the x-ray beam for two or more hours (equivalent to 6 complete EXAFS scans). Consequently, the position of the x-ray beam was moved to a fresh portion of **2** following three complete scans at individual spots, and the averaged data reflects the sum of the first three scans only at all exposed spots.

Data reduction, averaging, and normalization were performed using the program EXAFSPAK.[51] Following calibration and averaging of the data, background absorption was removed by fitting a Gaussian function to the pre-edge region and then subtracting this function from the entire spectrum. A three-segment spline with fourth order components was then fit to the EXAFS region of the spectrum to obtain $\chi(k)$. Analysis of the pre-edge features was carried out with the program SSExafs.[52] Theoretical phase and amplitude parameters for a given absorber-scatterer pair were calculated using FEFF 8.40[53] at the single-scattering level of theory, and were utilized by the opt program of the EXAFSPAK package during curve-fitting. In all analyses, the coordination number of a given shell was a fixed parameter, and was varied iteratively while bond lengths (r) and Debye-Waller factors (σ^2) were allowed to freely float. The amplitude reduction factor S_0 was fixed at 0.9. For each sample, E_0 (the point at which $k = 0$ Å^{-1}) was taken to be the first inflection point of the rising Fe K-edge, and the edge shift parameter ΔE_0 was allowed to float as a single value for all shells. ΔE_0 values were between -10 and +10 eV in all reported fits. In any given fit, the number of floating parameters = (2 × num shells) + 1. The goodness of fit F was defined simply as $\Sigma (\chi_{exptl}-\chi_{calc})^2$. In order to account for the effect that additional shells have on improving fit quality, an additional goodness-of-fit metric *F'* was employed. $F' = F^2 / (N_{IDP} - N_{VAR})$, where N_{VAR} is the number of floated variables in the fit, while N_{IDP} is the number of independent data points and is defined as $N_{IDP} = 2\Delta k \Delta r/\pi$.[54]

2.3 Results and Discussion

2.3.1 Previous Characterization

Initial investigations of complex **1** by our group showed a surprising new electronic absorption spectrum upon the addition of methoxide or hydroxide (see Figure 2.1). The reaction was found to be reversible by the addition of perchloric acid, with an 80 % yield of **1**. This initial finding led to an investigation of what gave rise to this new spectrum. ESI-MS, ^{1}H NMR, Mössbauer, resonance Raman, and XAS spectroscopy confirmed that a new species had formed. The ESI-MS spectrum showed a new peak

corresponding to an iron(IV)-oxo species similar to **1**, except for the loss of a proton. This finding, combined with the acid-base studies, indicated that new species was likely formulated as **2**. ^{1}H NMR spectroscopy indicated that two species were present and that the axial ligand was still bound in **2**. The Mössbauer spectrum confirmed that **2** was an iron(IV) species that was distinct from **1**. Resonance Raman spectroscopy showed a peak at 833 cm^{-1} for **1** and a peak at 823 cm^{-1} for **2**, which were consistent with iron(IV)-oxo stretches and a weakened Fe=O bond for **2**. These peaks shifted to 798 cm^{-1} and 787 cm^{-1}, respectively, which was consistent with Hooke's law. The XAS spectra also confirmed two distinct species that each had an O scattering atom in the EXAFS within the range commonly detected for iron(IV)-oxo moieties: 1.63 Å for **1** and 1.67 Å for **2**. The XAS spectra indicated that the two species were similar although distinct.

2.3.2 Acid-Base Titrations

Titration of **1** with NBu_4OH showed that 1.2 eq. were needed for the maximum conversion (91-93 % yield based on ε) at -40 °C. Determining the pK_a was complicated by the fact that there is water in the tetrabutylammonium hydroxide salt that was used, and that the pK_a of hydroxide in acetonitrile is not well established. However, a linear trend has been determined between pK_a values in acetonitrile and pK_a values in water,[55] which approximated the pKa value of hydroxide in acetonitrile to be ~26. Using this equation and the pKa of water in water, the pKa of **1** was determined to be approximately 23, close to the pKa of water in acetonitrile. Complex **1** is therefore a very weak acid, confirming the need for strong bases like hydroxide and methoxide to deprotonate it.

Another conjugate acid-base pair was discovered by adding perchloric acid to **3**. The spectrum of species **3** converted to a new spectrum upon addition of perchloric acid. A near-IR feature similar to, but distinct from that of **1** formed. This indicated that the carboxylate did not dissociate from the iron upon protonation, because a UV-vis spectrum was not similar to **6** (Figure 2.4). Titration reveals that 1.4 eq. of perchloric acid are needed for the maximum conversion to be reached, indicating that the likely carboxylate oxygen that is being protonated has a pKa of 4-5 at 25 °C, based on the range of pKa values of perchloric acid in acetonitrile reported,[56] which are complicated by the

water present due to the perchloric acid stock solution. Like the generation of **2**, the conversion was reversible; addition of an equal amount of 2,6-lutidine to **4** showed 97% recovery based on the molar absorptivity of the two peaks assigned to **3**. The resonance Raman spectroscopy also indicates that a new species is formed. The peak corresponding to the iron(IV)-oxo vibration shifts from 825 cm^{-1} to 836 cm^{-1} upon the addition of acid. Upon labeling with ^{18}O, the peak associated with **4** shifts to 795 cm^{-1}, four cm^{-1} larger than predicted by Hooke's law. While it is unusual for the ^{18}O shift to be larger than expected, this was seen in the original values reported for **3**, where 831 cm^{-1} shifted to 791 cm^{-1}, which was below the predicted 794 cm^{-1}.[57] The resonance Raman data, combined with the new near-IR feature, indicates that **3** and **4** are two different species and that they are an acid-base pair. Attempts to synthesize **4** independently of addition of acid to **3** by first generating the iron(II) acid complex were unsuccessful.

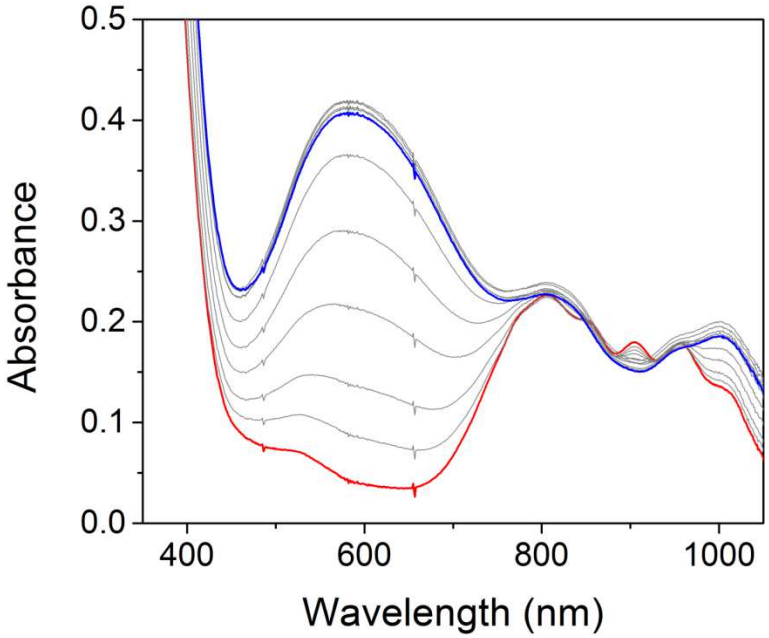

Figure 2.1: Electronic spectra recorded of the titration of 1 mM solution of **1** with tetrabutylammonium hydroxide (0.2 eq. per spectrum) from the starting spectrum (red) to the final spectrum of **2** (blue).

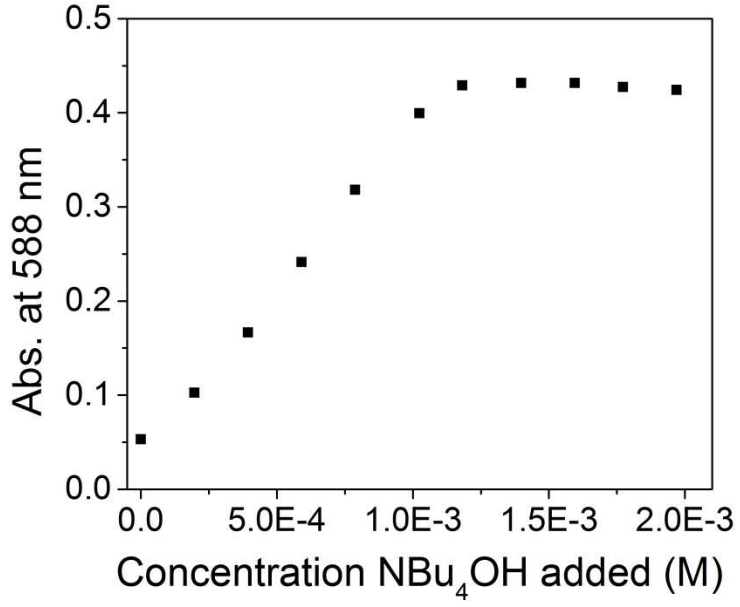

Figure 2.2: Titration curve of 1 mM solution of **1** titrated with tetrabutylammonium hydroxide versus the absorption feature at 588 nm of **2**.

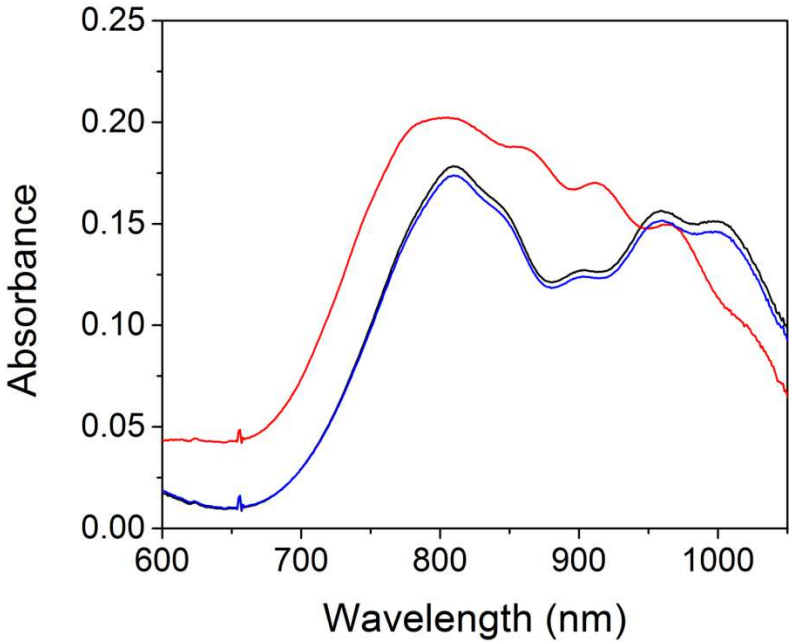

Figure 2.3: The electronic spectra at 0 °C of a 1 mM solution of **3** (black) upon addition of 1.5 eq. perchloric acid to generate **4** (red) and once 1.5 eq. of 2,6-lutidine is added to recover **3** (blue). Complex **3** was recovered in 97% yield based on the λ_{max} absorbances.

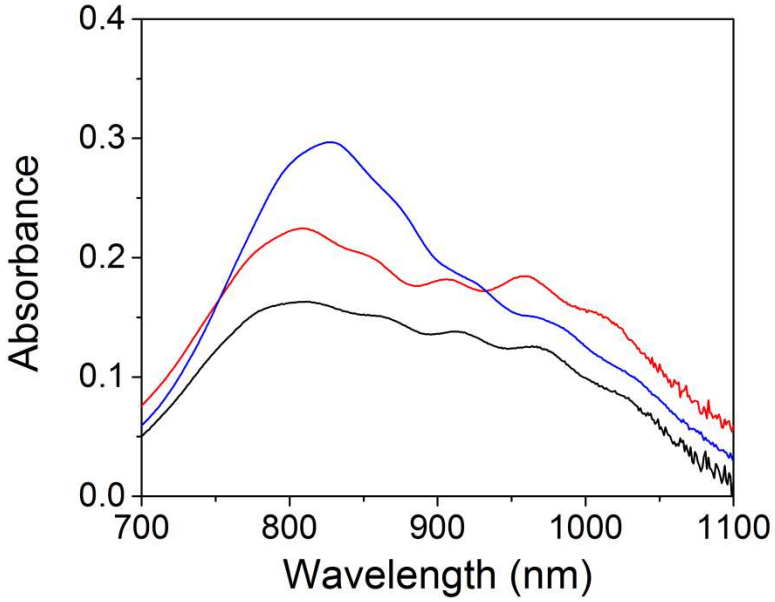

Figure 2.4: Comparison the near-IR portion of the UV-vis spectra of **4** (black), **1** (red), and **6** (blue) at 25 °C. The spectrum of **4** has features closer to what is seen in **1**.

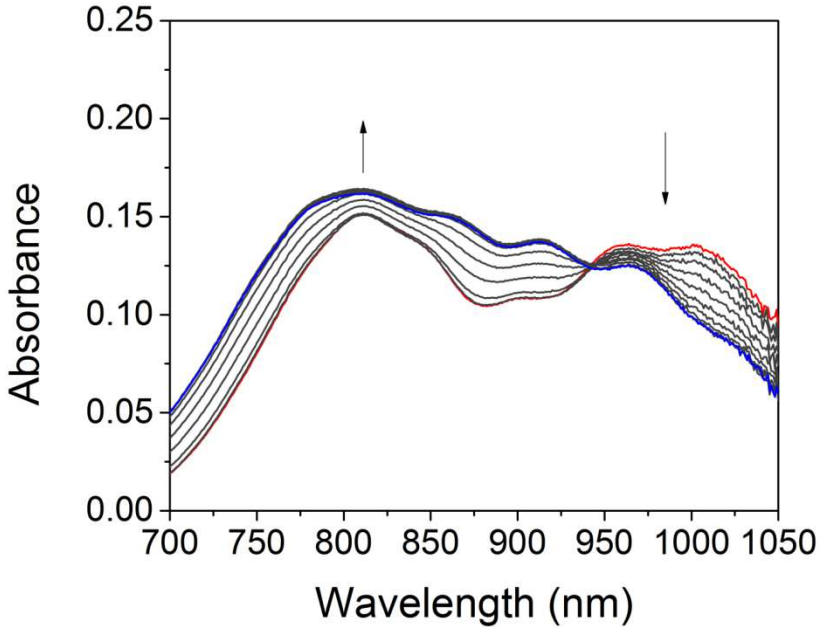

Figure 2.5: The electronic spectra at 25 °C of a 1 mM solution of **3** (red) titrated with $HClO_4$. Each new spectrum represents the addition of 0.2 eq. $HClO_4$ until the final spectrum at 2 eq. $HClO_4$ is obtained (blue).

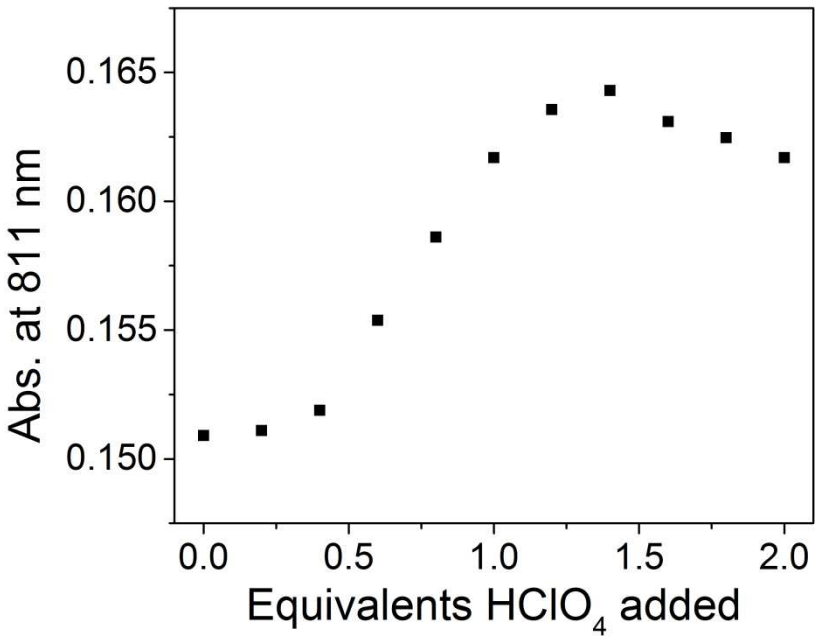

Figure 2.6: Titration curve of a 1 mM solution of **3** titrated with perchloric acid versus the absorption at 811 nm at 25 °C.

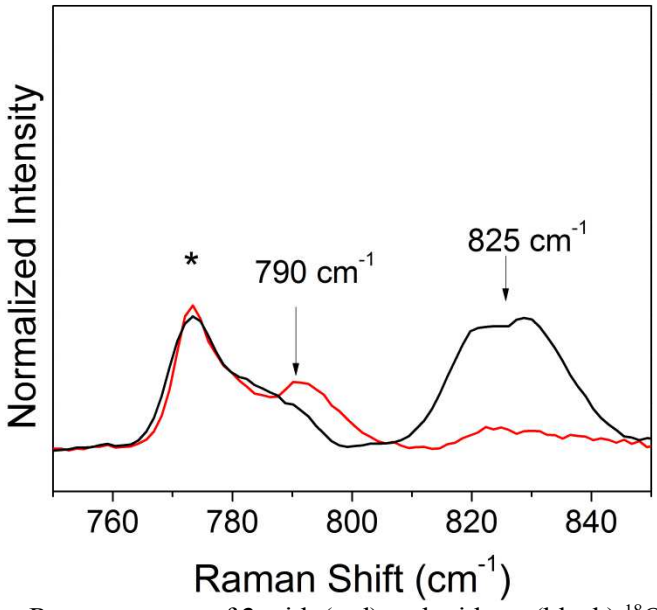

Figure 2.7: Resonance Raman spectra of **3** with (red) and without (black) ^{18}O-labeling. The ^{16}O spectrum has been smoothed. The data is similar to what was reported in the thesis of Frisch.[57]

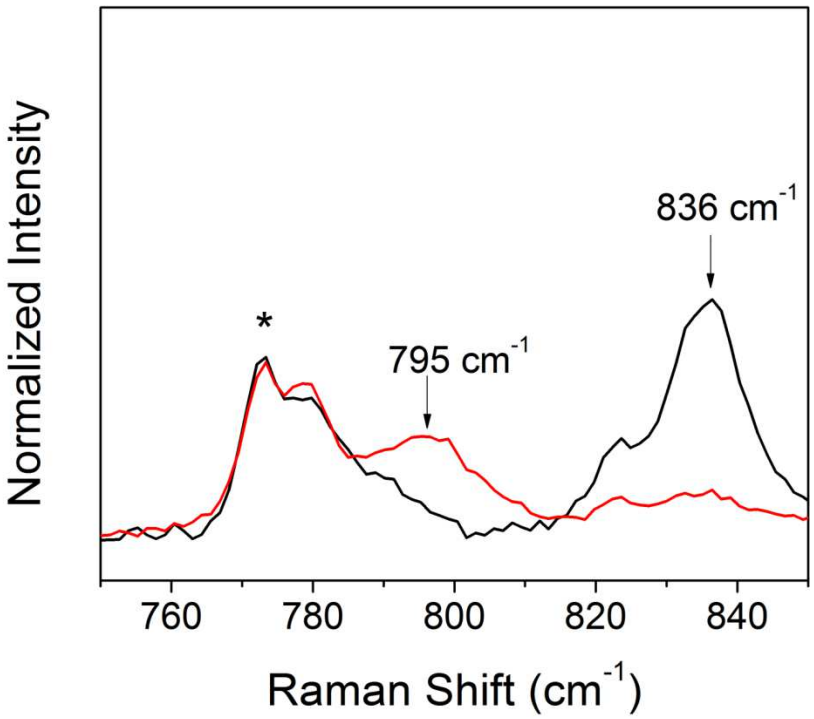

Figure 2.8: Resonance Raman spectra of **4** with (red) and without (black) ^{18}O-labeling. The difference is similar to what is predicted by Hooke's law for an iron-oxo stretch.

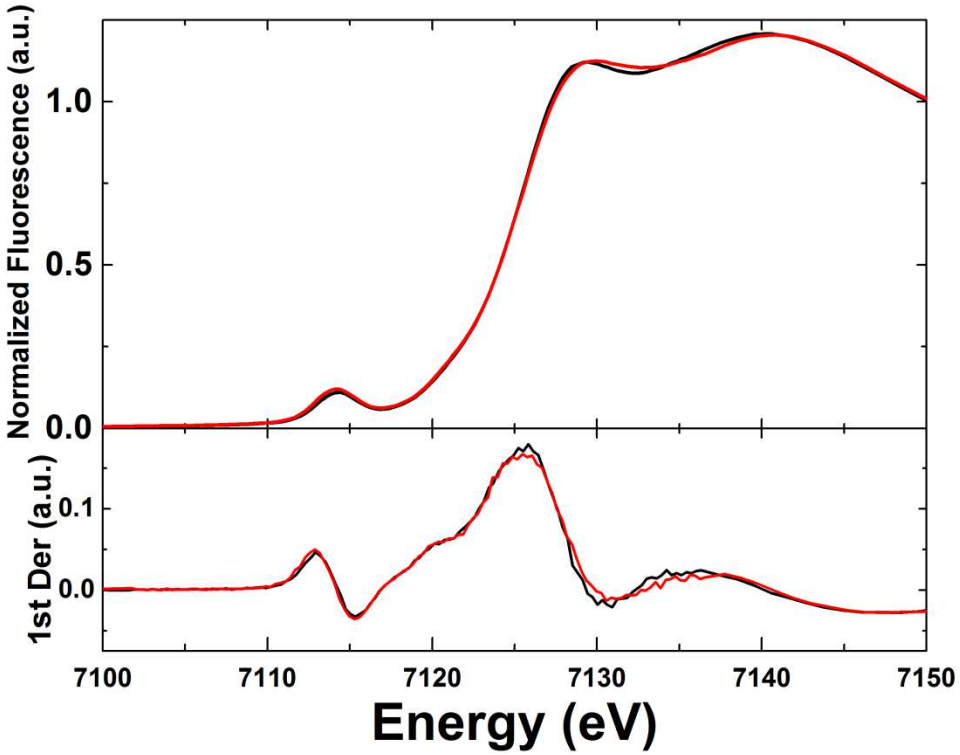

Figure 2.9: XAS spectra of **3** (black) and **4** (red), indicating that the species are very similar.

The generation of **4** by the protonation of **3** allowed for the comparison of their XAS spectra, which showed very little difference. This indicates that **3** and **4** are very similar and likely do not have complicating factors when comparing HAT reactivity.

2.3.3 Determination of $E_{p,c}$ Values of Fe^{IV}(O)TMC(X) Acid-Base Pairs by Cyclic Voltammetry

From previously reported Fe^{IV}(O)TMC(X) cyclic voltammograms,[26] it was known that iron(IV)-oxo complexes only show reductive peaks, which are occur at more negative potentials than expected when compared with their reactivity with certain substrates. With irreversible peaks such as these, there are two explanations. One explanation is that a chemical reaction occurs after the reduction, so the oxidative peak is not detected. The second is that the reduction rate is so slow that the peak separation is beyond the solvent window and therefore cannot be detected or both. Certain studies with **6** show a more quasi-reversible peak at faster scan rates.[58] Also, **6** was able to oxidize ferrocene, which would impossible if the $E_{p,c}$ (-0.32 V vs. Fc^{+}/Fc) represented a value close to the $E_{1/2}$. Therefore, the $E_{p,c}$ values of Fe^{IV}(O)TMC(X) are lower than the E_{red} and do not reflect the true oxidative potential of the iron(IV)-oxo complexes.

While these values do not represent the full oxidative potential of iron(IV)-oxo complexes, the $E_{p,c}$ is often easier to obtain than the actual E_{red}, (vide infra). These $E_{p,c}$ values cannot be used to assess true redox potential or used in calculations of thermodynamic parameters; however, it is possible to use $E_{p,c}$ values in a relative fashion for comparison, as long as the assumption that the kinetics at the electrode are similar for all species being compared. Using only TMC-based ligands for iron(IV)-oxo complexes allows for a similar enough set of complexes for comparison with such a method.

An interesting feature occurred in the cyclic voltammogram of **1**: there was a second reduction peak. Species **1** is known to form **2** upon addition of base, which, as stated before, is proposed to be the conjugate base. To test whether this second feature was related, the vial of solution was cooled to -40 °C. After an initial scan, 1.4 eq. of tetrabutylammonium hydroxide was added. This increased the current associated with the lower potential $E_{p,c}$ while the higher potential $E_{p,c}$ decreased in current. A similar cyclic voltammogram was recorded with the addition of tetrabutylammonium methoxide as the

base. As a control, tetrabutylammonium hydroxide was added to **5**, which does not form a detectable conjugate base, and the $E_{p,c}$ decreased in current, indicating that a typical Fe^{IV}(O)TMC(X) complex should be destabilized by addition of base, as would be predicted given that the reduced Fe^{III}-O^- would be even more unstable with fewer protons available. The increase of the second $E_{p,c}$ of **1** with the addition of base indicates **2** is being formed, as this is the dominant species at -40 °C with the addition of base.

Given that Fe^{III}-O^- moiety is a very basic species formed in a reducing environment, it was postulated that some of the **1** at the surface of the electrode was reduced to an Fe^{III}-O^- species, which then could abstract a proton from the remaining **1** in solution to form **2**. If this were true, addition of acid would prevent the formation of the conjugate base. Indeed, upon addition of pyridinium triflate, the higher $E_{p,c}$ increased slightly in current, but the second peak became almost non-existent. When the same experiment is carried out with **5**, the $E_{p,c}$ increased in current similarly to the first peak seen in **1**. This indicates that upon the reduction of **1** to an Fe^{III}-O^- species, the Fe^{III}-O^- species will abstract a proton either from solution, if possible, or from remaining **1** to form **2**. Thus, both **1** and **2** had $E_{p,c}$ values that could be utilized for reactivity studies.

Complex **3** showed a peak at -0.92 V vs. Fc^+/Fc under the same conditions as were reported for previous Fe^{IV}(O)TMC(X) complexes.

The $E_{p,c}$ value for **4** could not be measured due to interference of acid and water in reduction potentials of iron(IV)-oxo complexes. As reported in Wang *et al.*, the reductive peak becomes reversible upon the addition of enough water and increases in potential. This is likely due to the ease at which an iron(III)-hydroxo is formed compared to an iron(III)-oxide. Without a way to synthesize **4** independently, it was impossible to obtain an accurate $E_{p,c}$ value.

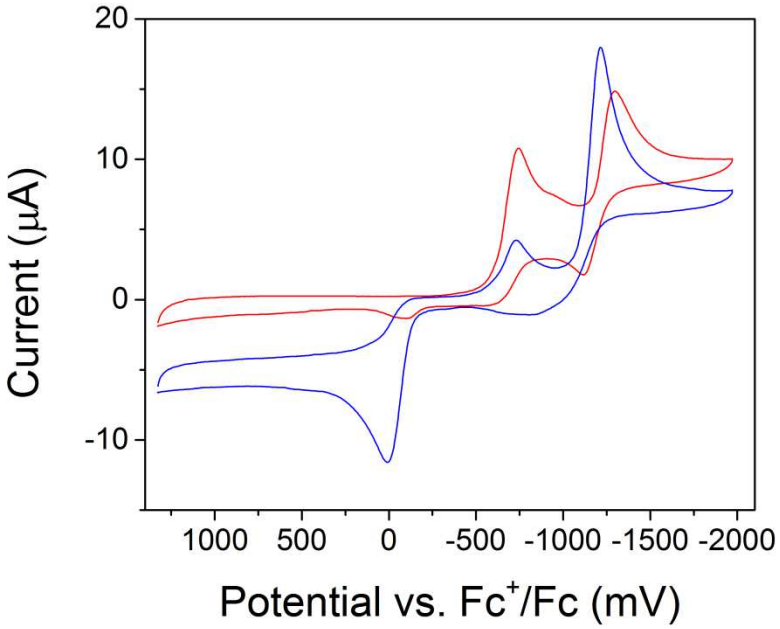

Figure 2.10: Cyclic voltammograms at -40 °C of a 1 mM solution of **1** (red) and after the addition of 1.4 eq of tetrabutylammonium hydroxide (blue).

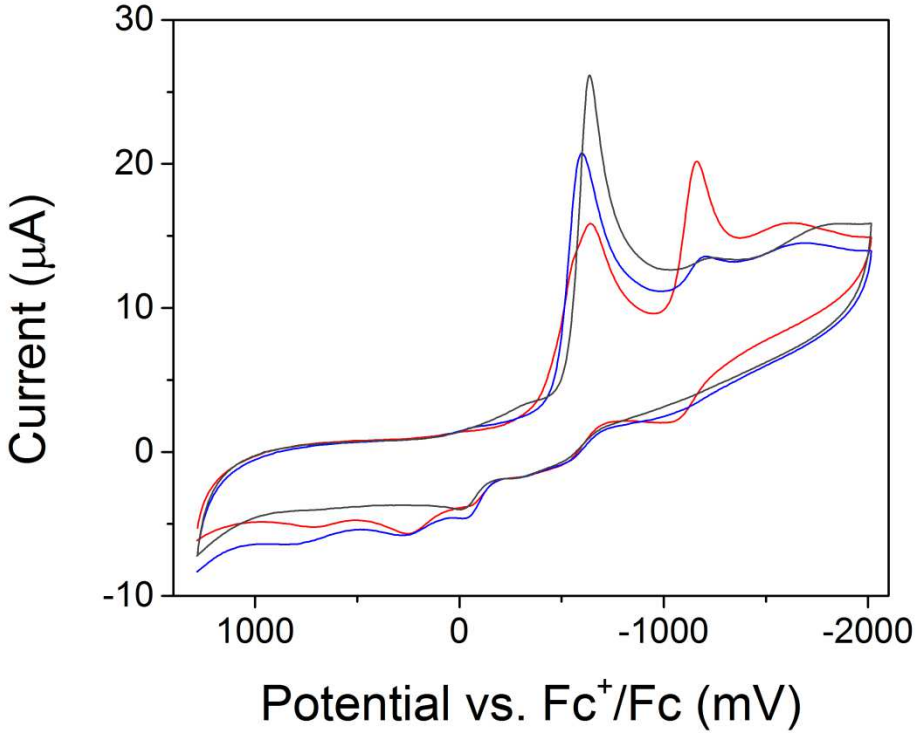

Figure 2.11: Cyclic voltammograms at room temperature of a 1mM solution of **1** (red) and after the addition of 0.1 eq. pyridinium triflate (blue) and 0.2 eq. of pyridinium triflate (grey).

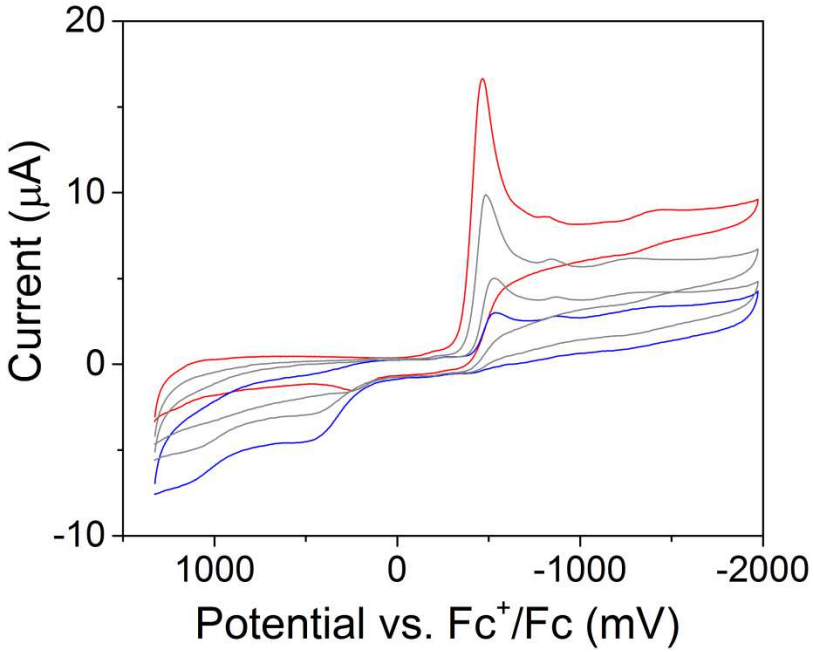

Figure 2.12: Cyclic voltammograms at -40 °C of a 1 mM solution of **5** (red) and after the addition of 0.4 eq of tetrabutylammonium hydroxide (grey) until a final concentration of 1.2 eq of tetrabutylammonium hydroxide (blue).

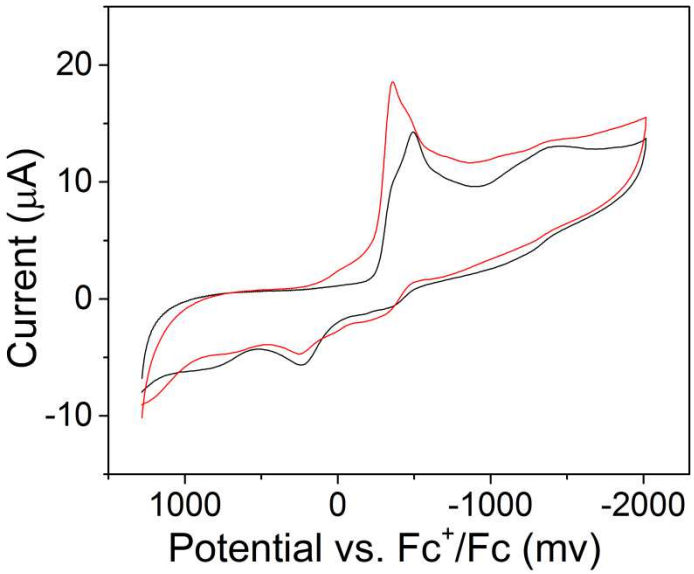

Figure 2.13: Cyclic voltammograms at room temperature of a 1mM solution of **5** (black) and after the addition of 0.2 eq. pyridinium triflate (red).

2.3.4 Determination of Redox Potential of Fe^{IV}(O)TMC(X) Acid-Base Pairs by Chemical Reduction

Determining redox potentials for iron(IV)-oxo species is complicated by the irreversible nature of the cyclic voltammograms for iron(IV)-oxo complexes. The irreversible nature is likely caused by the instability of the reduced form, Fe^{III}-O^{-}. The instability could decrease the rate of electron transfer to the iron(IV)-oxo complex and, when formed, decays rapidly so no return peak is observed. However, Fukuzumi has reported success in using ferrocene based reductants for the purpose of determining redox potentials of Fe^{IV}(O)TMC(X) species.[50] Addition of varying amounts of reductant to solutions of the same concentration of Fe^{IV}(O)TMC(X) allows for the equilibrium constant for electron transfer to be found and therefore the redox potential of the iron(IV)-oxo complexes. This is preferable to the determination by cyclic voltammetry because the redox potential can be obtained and not just the $E_{p,c}$.

In reproducing Fukuzumi's results with **6**, a value of 3 for K_{et} was found instead of 2 that was reported. Although larger spread of values was seen, this affects the value of the redox potential very little (0.39 V vs SCE and 0.40 V vs SCE) (Figure 2.14). Given the reproducibility of the data, it seemed that the method could be used to determine the redox values of the different Fe^{IV}(O)TMC(X) complexes.

However, the Fe^{IV}(O)TMC(X) complexes tried showed a large amount of scatter and error in the data. The error was partly due to decamethylferrocenium absorbs in the same region as **1**; this was taken into account by subtracting out the absorbance that was due to the **1** from the 780 nm peak forming from Fc^{*+}, but this increased the error. Instead, the values were determined based on the absorbance of the iron(IV)-oxo species, with the rest calculated assuming mass balance. This was first tried with the data for **6** (Figure 2.15), which showed good agreement with K_{et} =2, in good agreement with the previously reported results. When the same method was applied to **1**, K_{et} was found to be 0.72, which gives a redox potential of -0.09 V vs SCE (-0.46 V vs. Fc^{+}/Fc). This value is higher than the $E_{p,c}$ value reported (-0.63 V vs. Fc^{+}/Fc) but not as dramatic a difference as reported for other Fe(O)TMC(X) species. This value is lower than all other redox potentials given for TMC-based iron(IV)-oxo complexes investigated using ferrocene

derivatives by the Fukuzumi group.[50] The value is consistent with the anionic nature of the appended ligand and the more electron-donating methylene group as compare to the trifluormethyl group of trifluoroacetate, which had a value of 0.13 V vs SCE.[50]

The reduction of **2** showed a curve instead of a line for K_{et} with varying amounts of cobaltocene. Cobaltocene required the use of tetrabutylammonium methoxide as the base, solubilized in methanol, to generate **2** because cobaltocene would react with any excess water from the tetrabutylammonium hydroxide. A line could be fit, which indicated that $K_{et} \approx 6.6$, which would correlate with a reduction potential of ~ -1.5 V vs. SCE (-1.9 vs. Fc^+/Fc). This number is actually lower than the $E_{p,c}$ value (-1.16 V vs Fc^+/Fc). The K_{et} was determined at -40 °C, whereas the $E_{p,c}$ value was determined at 0 °C, but still this is a large difference towards a more negative value. As **2** was not generated by the same method in both cases, this may account for some of the differences.

The difference in reduction potentials between **1** and **2** using this method is larger (1.4 V) than the $E_{p,c}$ values (0.53 V) (vide supra). This may be due to the errors in measurement from the K_{et} determinations. The redox potentials also change based on the redox potential chosen for the decamethylferrocene or cobaltocene from the literature, which has some reported variation. There is also the issue in each of two equilibria: that between the $Fe^{IV}(O)$ and the reductant and the equilibria between **1** and **2**. Considering reducing **1** seems to allow for formation of **2** (vide supra), this may lead to error in the measurements. However, the general trend reported with the $E_{p,c}$ values is maintained, as **2** is much harder to reduce than **1**, and correspondingly the ligand of **2** is more electron-donating.

Addition of Fc* to **3** showed some curvature, although a line could be fit for a $K_{et} = 1.3$, which gave a redox potential of -0.07 V vs SCE (-0.44 V vs. Fc^+/Fc). There seems to be more error in this measurement, as the fit does not pass close to zero, and the errors in both the slope and the intercept are greater than the values. There seems to be even more unreliability in these measurements than the others measured in these studies, so the value of -0.07 V is more tentatively suggested.

The conjugate acid **4**, generated by the addition of perchloric acid to **3**, showed strange reactivity with diacetylferrocene. From UV-vis spectra, the formation of diacetylferrocenium was instantaneous as well as the reformation of **3**. The ferrocenium species decayed as an increase of **3**. Likely perchloric acid, which has water present, interfered with the reaction. As **4** could not be synthesized independently of **3** in the presence of strong acid, the approximate redox potential could not be determined.

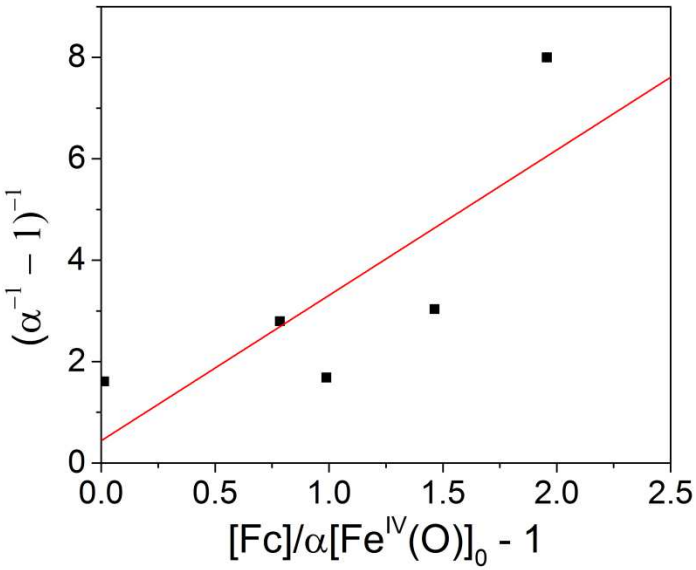

Figure 2.14: The linear fit that provides K_{et} for **6** using the equation rearrangement from Fukuzumi.[58] $K_{et} = 3$, in good agreement with what was previously reported.

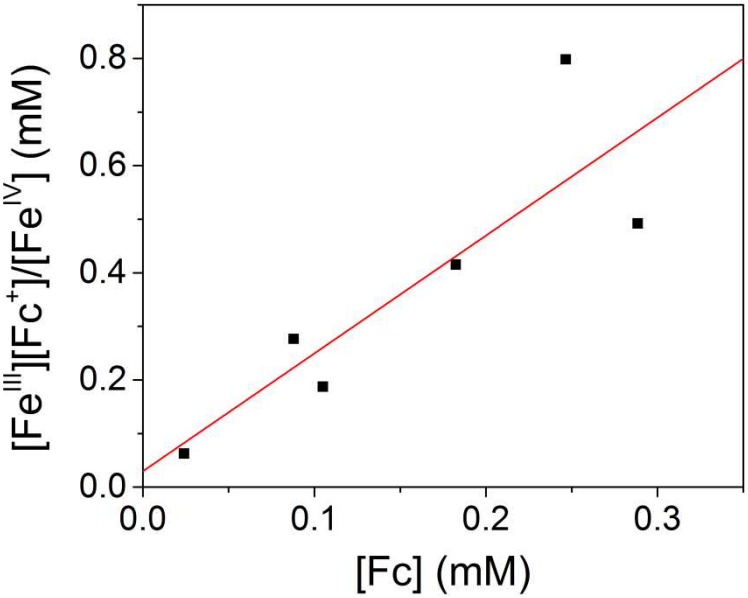

Figure 2.15: The linear fit that provides K_{et} for **6** using the unmodified equation for equilibrium. $K_{et} = 2$, in good agreement with what was previously reported.

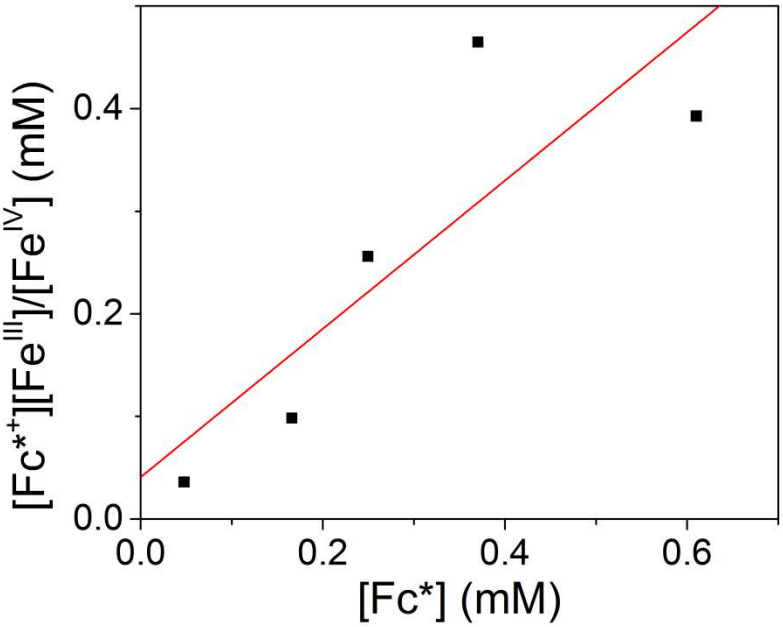

Figure 2.16: Fitting of titration data of **1** with Fc* at 25 °C. While a straight line can be fit there is a lot of scatter. The linear fit gives a $K_{et} = 0.72$.

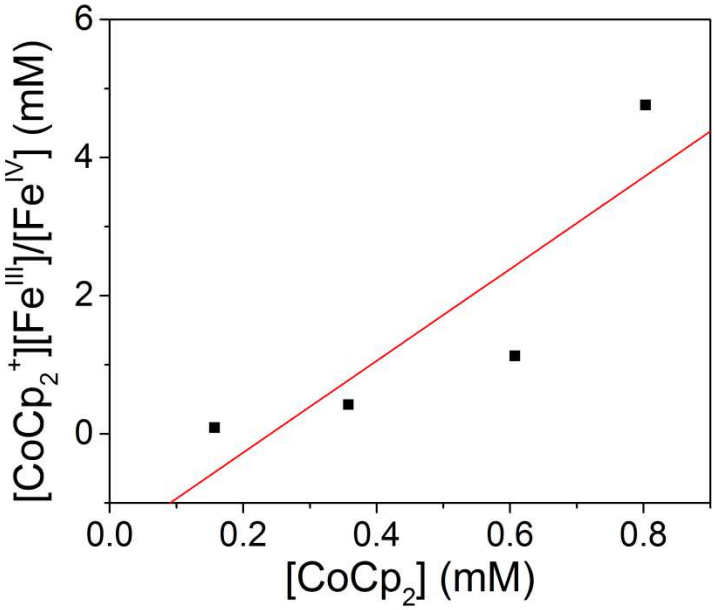

Figure 2.17: Titration data of **2** with $CoCp_2$ at -40 °C. Fitting with a line shows the scatter. The linear fit gives $K_{et} = 6.6$.

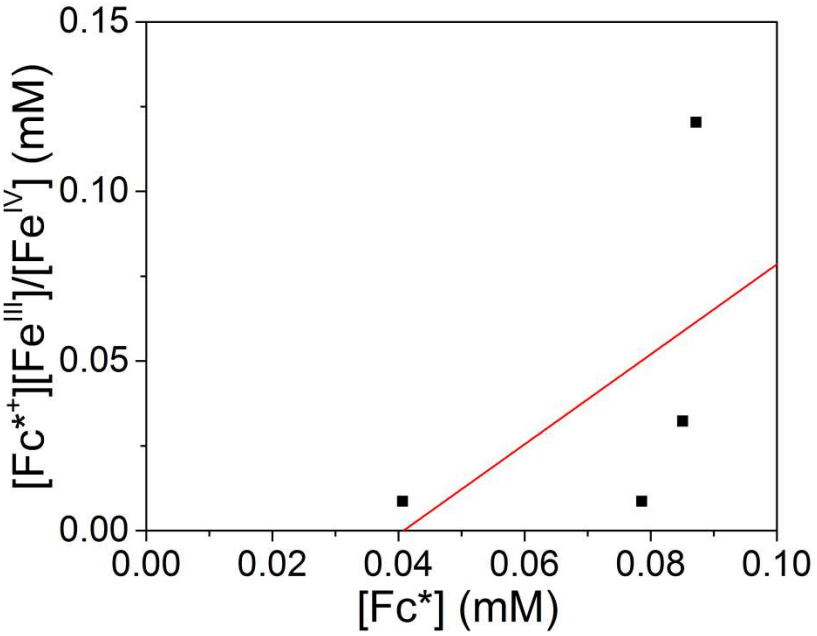

Figure 2.18: Fitting of titration data of **3** with Fc* at 25 °C, the error of the slope and the intercept are greater than the slope and intercept, respectively. The linear fit gives a $K_{et} = 1.3$.

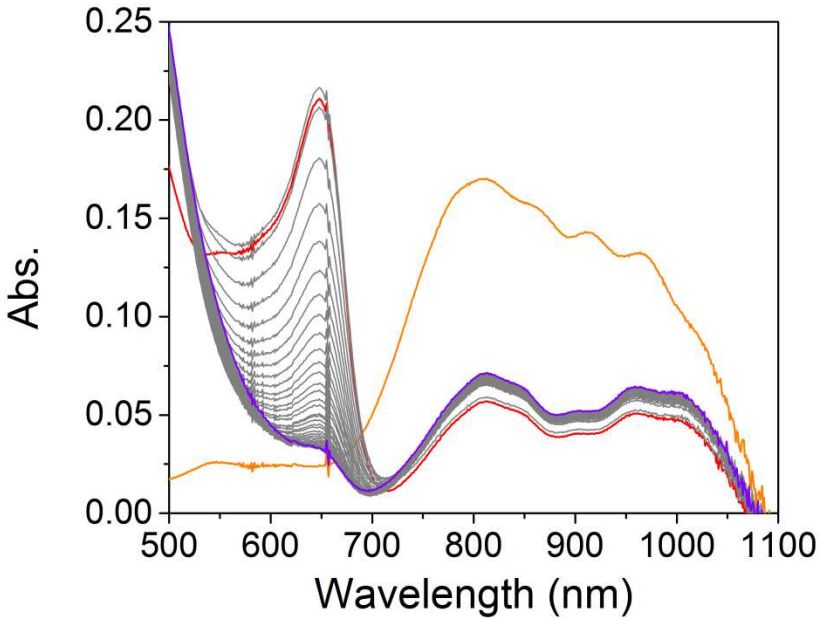

Figure 2.19: UV-vis absorption spectra of **4** (orange) after the addition of diacetylferrocene (red) at 25 °C. The peak associated with the diacetylferrocene forms instantaneously, and then decays as more **3** forms based on the near-IR feature.

2.3.5 Reactivity of Fe(O)TMC(X) Acid-Base Pair

2.3.5.1 Oxygen Atom Transfer

Oxygen atom transfer (OAT) involves the transfer of an oxygen atom from the iron(IV)-oxo to a substrate, as well as the transfer of two electrons to the iron. Thioanisole or phosphine derivatives are often used, with phosphine derivatives being chosen when reaction rates are slow. In the previously reported study on Fe^{IV}(O)TMC(X) complexes, triphenylphosphine was chosen for this reason.

To be consistent with this study, the reaction with triphenylphosphine was first attempted, except in the case of **4**, where the pK_a of perchloric acid used to generate the species was similar to that of PPh_3. Species **1** and **5** reacted with triphenylphosphine, with triphenylphosphine oxide yields of 90% and 93%, respectively. Species **2** reacted too slowly with this substrate for an accurate rate to be determined. Instead, **2** was reacted with methyldiphenylphosphine and produced methyldiphenylphosphine oxide in 83% yield. Species **1** was reacted with the same substrate, showing a rate over an order of magnitude faster (Table 2.1). From these reactions, the rate of reactivity increased in the order **2** < **3** < **1** < **5**, with **3** and **1** being over an order of magnitude different, as well as **1** and **5**. Over a hundred-fold difference in rates is present between complex **3** and **5**, indicating how strong an influence the axial ligand has on reactivity of iron(IV)-oxo complexes in this series.

The reactions with triphenylphosphine allowed for comparison of reactivity among the TMC-based iron(IV)-oxo complexes. From the previous study, there was a correlation between the $E_{p,c}$ values and the k_2 for OAT. When $E_{p,c}$ values were plotted against log(k_2), a linear, electrophilic trend was observed. The electrophilic trend indicated that the increasing electron-donating power of the axial ligand inhibited OAT. This result was unsurprising as OAT involves a two-electron transfer to the iron, so the less electron density around the iron, the easier the transfer of oxygen to the substrate.

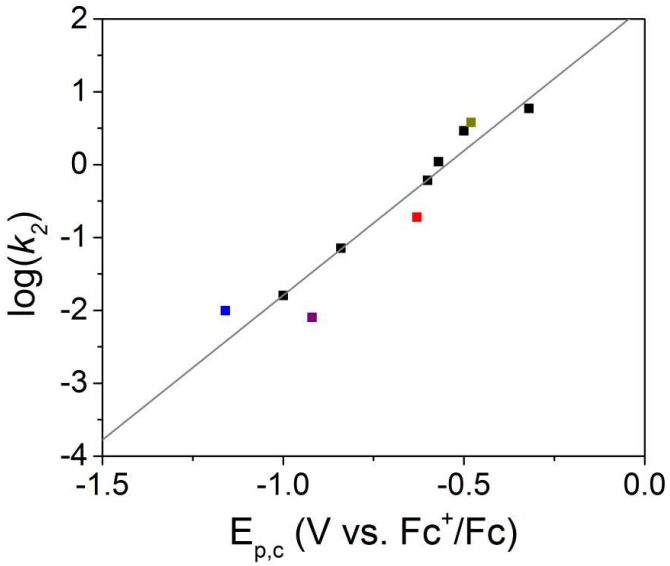

Figure 2.20: Comparison of the trendline (grey line) generated from the Sastri *et al*. study of $E_{p,c}$ vs log(k_2) of PPh_3 at 0 °C. Note that the complexes from this study (**1**, red; **2**, blue, **3**, purple, **5**, brown) fall close to the line generated previously. The rate constant of **2** had to be estimated from the rate with $PMePh_2$ and comparing that with the rate of **1** and $PMePh_2$.

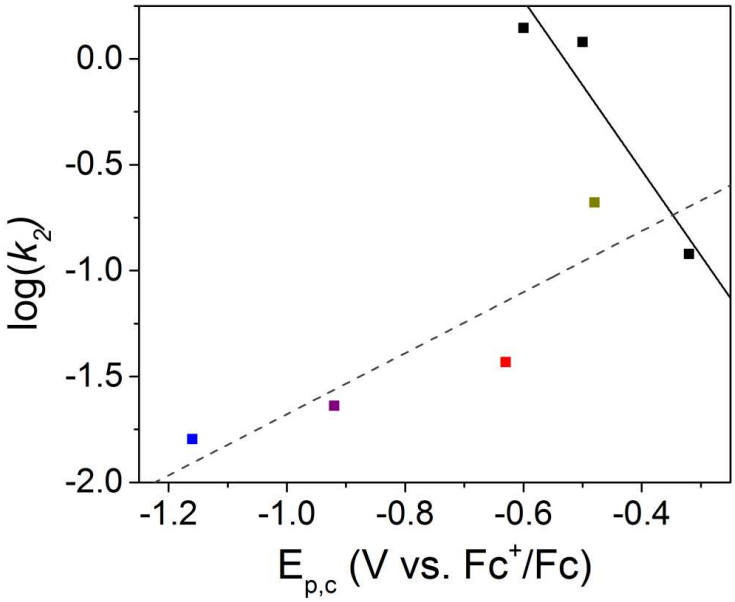

Figure 2.21: Comparison of the trend of $E_{p,c}$ vs log(k_2) of 1,4-cyclohexadiene at 0 °C from Sastri *et al.* (black line) from the complexes reported therein (black squares) and the trendline formed from the complexes in this study (**1**, red; **2**, blue, **3**, purple, **5**, brown). There is no overall correlation of $E_{p,c}$ value and rate constant for this HAT reaction.

Our results for OAT were consistent with what was presented previously. The values for **1, 2**, **3**, and **5** are close to the line generated from the previously reported Fe^{IV}(O)TMC(X) complexes. Species **2** was estimated from comparing the k_2 from $PMePh_2$ for **2** with that of **1**; a predicted k_2 for the reaction with PPh_3 could be generated with the use of the k_2 for **1** from this reaction.

Overall, these findings support the conclusion that OAT rates for iron(IV)-oxo complexes are correlated with reduction potentials. This correlation has been noted in several papers,[26,28,29] indicating that likely the electron density at the iron directly affects the rate of reaction of OAT.

2.3.5.2 Hydrogen Atom Transfer

Reaction of 1,4-cyclohexadiene and complexes **1**, **2**, **3** and **5** allowed HAT reactivity to be probed. Benzene was obtained as the major product in the cases where product analysis was conducted (reactions with **1**, **2**, and **5)**, in 60-80% yield. The k_2 values of **1**, **2**, and **3** were all on the same order of magnitude, with **5** being an order of magnitude more reactive. Interestingly, while **1** has a similar in $E_{p,c}$ value to Fe^{IV}(O)TMC(N_3), the latter was approximately 40 times more reactive. However, even though **1** and **2** had reduction potentials 0.53 V apart, **1** was only twice as reactive as **2**. While no $E_{p,c}$ data could be gathered for **4**, **4** is twice as fast as **3**, similar to the difference in the reactivity between **1** and **2**.

All these observations are counter to what has been reported previously. In Sastri *et al*., the four complexes showed increased reactivity for HAT correlated with a decrease in $E_{p,c}$ value.[26] This anti-electrophilic trend indicated that the greater the electron donating power of the axial ligand, the more reactive the iron(IV)-oxo moiety would be to HAT. However, our complexes create a new trend line that is opposite to the one proposed before. Instead, our complexes follow an electrophilic trend.

Our results differ from the prevailing model of two-state reactivity (TSR), which indicates that the smaller the gap between the triplet state and the quintet state for the intermediate, the more reactive the iron(IV)-oxo species will be with respect to HAT. The gap between the triplet and the quintet states is governed by the electron donating power of the ligand. Thus, based on this model, **2** should be more reactive than **1**, yet the

opposite is true; in fact, there is very little difference in reactivity of these two complexes. DFT calculations indicate that the only significant bond-length difference between these two complexes is the ligands in the axial position, as would be expected from changes in the *trans* ligand. The electron donating power of the ligand *trans* to the oxo moiety should correlate directly with a smaller triplet-quintet gap, yet the reactivity does not reflect this. Therefore TSR cannot explain the reactivity differences seen between this acid-base pair.

While there is no overall trend for HAT with all the TMC-based complexes, it is interesting that both acid-base pairs exhibit only a two-fold difference in rate constants. Since each pair is more similar to one another than the TMC-based complexes reported previously, it stands to reason that these complexes are more likely useful in indicating how axial ligand basicity changes the reactivity. While structurally similar, these complexes differ in charge, yet little reactivity difference is seen. Other factors likely influence the reactivity of these complexes more than the charge of the ligand.

Table 2.1: Reaction rates of different iron(IV)-oxo complexes from this chapter.

Complex	$t_{1/2}$	k_2 [M^{-1} s^{-1}] in CH_3CN, 0 °C			$E_{p,c}$ (V *vs* Fc^+/Fc)	
		CHD[a]	PPh_3	$PMePh_2$	25 °C	-40 °C
1	5 days (25 °C)	0.037(2)	0.19	5.9(3)	-0.63	-0.74
2	~ 1.5 hrs (0 °C)	0.016(1)	<0.004[d]	0.32(2)	-1.16	-1.23
3	48 (25 °C)	0.023(1)	0.006	N/A	-0.92	N/A
5	7 hrs[c] (25 °C)	0.22(1)	3.8	N/A	-0.48	N/A

2.4 Conclusion

HAT reactivity allows us to connect the reactivity of the synthetic iron(IV)-oxo model complexes to the reactivity of their nonheme iron enzyme counterparts. While previous studies have correlated decreasing reduction potential of iron(IV)-oxo complexes with an increase in HAT rate, the complexes had differences with the tethering of the axial ligand to the TMC-framework, the solvent systems used, and the type of the atom coordinated to the iron at the axial position.[26] Two acid-base iron(IV)-

oxo pairs were identified and characterized. By cyclic voltammetry, the $E_{p,c}$ values for **1** and **2** were obtained. The reactivity of these complexes were compared with the data reported in Sastri *et al*.[26] While new OAT data fit into the previously reported trend of increasing reactivity with increasing $E_{p,c}$ values, the new HAT data did not follow the previous trend of decreasing reactivity with increasing $E_{p,c}$ value. The acid-base pair allowed for the unique opportunity to compare reactivity of two very similar complexes. The structures of **1** and **2** were very similar based on DFT calculations. However, **1** was more reactive than **2** even though it had a higher reduction potential. This indicates that the TSR model is unable to explain all HAT reactivity seen in iron(IV)-oxo species, and likely, a new model will have to be formulated that encompasses all iron(IV)-oxo complexes.

Chapter 3

Reactivity of Iron(IV)-oxo Species Axially Ligated with Carboxylates

This work is based on a paper in progress by: Jennifer O. Bigelow, Jason England, Marlène Martinho, Erik R. Farquhar, Jonathan R. Frisch, Victor J. Young, Jr., Eckard Münck,* and Lawrence Que, Jr.*

3.1 Introduction

Nonheme mononuclear iron enzymes are essential for a wide variety of reactions in the biological world that utilize molecular oxygen as an oxidant.[1,2] Despite this wide array of reactivity, many have a common motif: a 2-His-1-carboxylate facial triad.[1] This motif allows for a similar, reactive high valent iron-oxo intermediate to form in many cases. [6,8,9,11–13] This high-valent species has been implicated as the reactive intermediate. An iron(IV)-oxo intermediate has been trapped and characterized in several enzymes.[4,5,10,11] This intermediate is proposed to abstract a hydrogen atom from the substrate; a radical rebound mechanism can follow, where the hydroxo moiety reacts with the newly formed radical to form the product.[1] However, the exact factors affecting the reactivity of this iron(IV)-oxo species are still unknown.

While much has been investigated with the actual enzymes, modifications are more easily achieved in synthetic model systems. With these model complexes, factors such as spin state, electronics, and sterics can be modified to investigate how these different components can affect reactivity.[16,26,59,60] The most systematic of these studies involved iron(IV)-oxo complexes using tetramethylcyclam (TMC)-based compounds. Initial work by Sastri *et al*. indicated that oxygen atom transfer (OAT), a two-electron process, was correlated with the electron-donating capability of an axial ligand, whereas hydrogen atom transfer (HAT), was inversely correlated with electron donating ability of the axial ligand.[26] This difference could be explained by the Two-State Reactivity (TSR) model.[26,41]

The original explanation of TSR indicated that the difference in energy between the ground $S = 1$ and the excited $S = 2$ states of the Fe^{IV}=O species controlled the reactivity of the iron(IV)-oxo complexes.[26,41] The smaller the gap, the more contribution of the $S = 2$ transition state to the reaction, which was lower in energy than the $S = 1$ transition state. The gap was controlled by the axial ligand electron donating ability, so that the complexes with the more electron donating ligands were more reactive.

The TSR model was recently challenged by a conjugate acid-base pair (**1** and **2**) utilizing the same TMC framework.[60] While **2** had an axial ligand much more electron-donating than **1** based on cyclic voltammetry, the HAT rates of **1** were faster than **2**. This

Scheme 3.1: Conjugate acid-base pair from a previous study

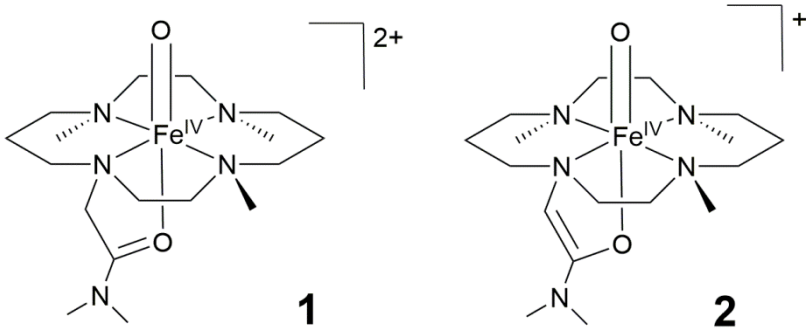

Scheme 3.2: Iron(IV)-oxo complexes used in this study

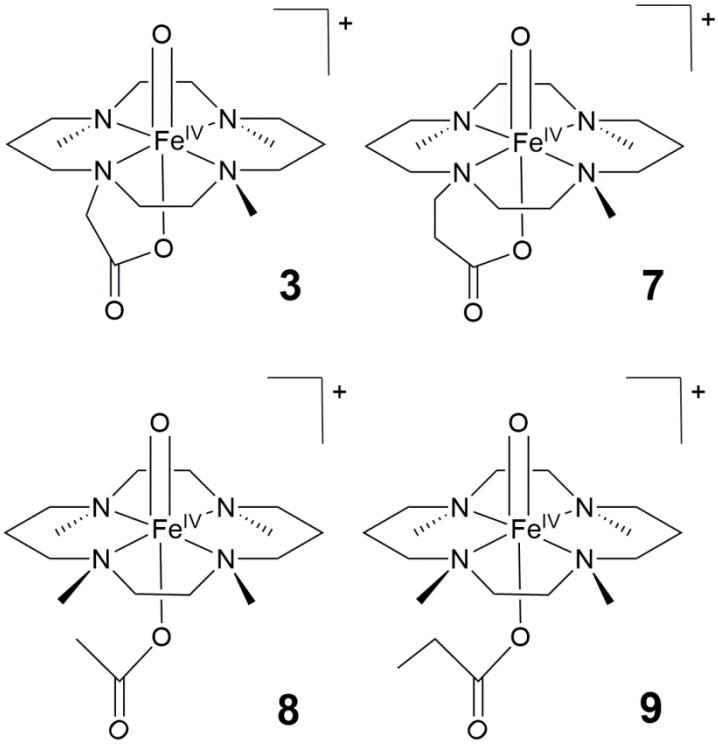

case of two very similar iron(IV)-oxo complexes that only differed by the loss of a proton indicates that reactivity of these complexes is not just based on electron-donating ability of the axial ligand alone.

In response to this, a modified version of TSR was recently presented wherein tunneling accounts for the anti-electrophilic response.[61] Tunneling contributions indicate that the reaction primarily proceeds through the $S = 2$ transition state, as the KIE values are non-classical, but in the range of 10-60. The $S = 1$ transition state would result in KIE values in the hundreds. While all the complexes have non-classical KIE values, a noticeably larger one is proposed for $[Fe(O)TMCS]^+$, which originally contributed to the anti-electrophilic trend. The study predicts that more electron-donating ligands will have higher KIE values for HAT, while OAT cannot proceed through this path because of the larger size of the oxygen molecule. This explanation indicates that KIE will have a more important role in predicting reaction rates than before.

Herein, we continue the investigation of TMC-based iron(IV)-oxo complexes with a series of axially bound carboxylate ligands. These ligands vary in the nature of the attachment to the framework, allowing for the flexibility of the ligand framework to be examined. Two complexes involve linked carboxylates: **3**, an acetate and **7**, a propionate, while two complexes have free anions bound axially: **8**, an acetate, and **9**, a propionate. These modifications of the ligand framework greatly affect HAT reactivity. Investigations into this reactivity indicate that likely TSR cannot fully explain the reactivity differences seen among these complexes, but rather the tethering of the ligand has unexpected consequences.

3.2 Experimental

3.2.1 General Considerations

All reagents were purchased from Aldrich and used as received unless noted otherwise. Diethyl ether and tetrahydrofuran were dried by prolonged reflux, under a nitrogen atmosphere, over sodium metal with a benzephenone ketyl indicator and distilled freshly prior to use or bought anhydrous. Acetonitrile, dichloromethane and triethylamine were treated in a similar manner, but using calcium hydride as the drying

agent, or were bought anhydrous. Methanol was dried by reaction of the water present with excess sodium metal and then distilled under a nitrogen atmosphere or bought anhydrous. Iodosobenzene (PhIO),[42] its ^{18}O-labelled isotopomer PhI^{18}O,[62] $Fe(OTf)_2(CH_3CN)_2$,[47] 1,4,8-trimethyl-1,4,8,11-tetraazacyclotetradecane,[63,64] 4,8,11-trimethyl-1,4,8,11-tetraazacyclotetradecane-1-acetic acid tetrahydrochloride salt (TMCAcH·4HCl),[46] and NBu_4OPr[65] were all prepared according to published procedures. $[FeTMC(CH_3CN)](OTf)_2$ was prepared either by a previously published procedure[48,] or by the method outlined in the previous chapter. TMC was purchased from Angene International Limited or Strem. Triphenylphosphine was purified by dissolving in hexane and running through a silica gel column. 9,10-dihydroanthracene (DHA) was purified by a published procedure[66] and d^4-DHA was synthesized by a published procedure.[67]

All moisture and oxygen sensitive compounds were prepared using standard high vacuum line, Schlenk, or cannula techniques. A standard nitrogen-filled glove box was used for any subsequent manipulation and storage of these compounds. NMR spectra were recorded using Varian Inova 500 MHz or 300 MHz spectrometers. Chemical shifts (ppm) were referenced to the residual protic solvent peaks. Elemental analyses were performed by Atlantic Microlab (Norcross, GA). UV-Visible studies were performed using a HP8453A diode array spectrometer equipped with a cryostat from Unisoku Scientific Instruments (Osaka, Japan). Electrospray ionization mass spectrometry experiments were carried out on a Bruker BioTOF II mass spectrometer using a spray chamber voltage of 4000 V and a gas carrier temperature of 60 ºC. FT-IR spectra were recorded in CH_3CN solution at ambient temperatures in a CaF_2 solution cell (International Crystal Labs), using an Avatar 370 spectrometer (ThermoNicolet).

3.2.2 Synthetic Procedures

Dr. Jason England developed the TMCPrAH·4HCl synthesis, along with the method of generating the iron(II) complexes and iron(IV)-oxo complexes, except for **9**.

TMCPrAH·4HCl: To a solution of Me_3cyclam (1.00 g, 4.13 mmol) in acetonitrile (40 mL) was added 20 equivalents of *tert*-butyl acrylate (12.1 mL, 82.5 mmol) and the resulting mixture was allowed to stir under argon for 72 hours. Subsequently, all volatiles were removed under vacuum to provide a yellow oil. ^{1}H-NMR

($CDCl_3$, 500 MHz): δ2.76 (t, 2H, NCH_2CCO_2), 2.54 (m, 4H, NCH_2), 2.44 (m, 12H, NCH_2), 2.35 (t, 2H, CH_2CO_2), 2.22 (s, 3H, NMe), 2.21 (s, 3H, NMe), 2.20 (s, 3H, NMe), 1.64 (p, 4H, $NCCH_2CN$), 1.44 (s, 9H, ^{t}BuO). ^{13}C-NMR ($CDCl_3$, 125 MHz): δ172.28, 54.71, 54.45, 54.25, 53.69, 53.62, 53.42, 50.58, 50.47, 50.22, 43.62, 43.58, 43.29, 33.18, 28.15, 24.40. MS (+ESI): *m/z* 371.5 [$(M+H)^+$].

The ester was dissolved in trifluoroacetic acid (40 mL) and stirred in a sealed flask, at ambient temperature, for 96 hours. Removal of all volatiles yielded a brown oil, from which an off-white solid could be obtained by trituration with diethyl ether overnight. This solid was isolated by filtration, washed with further diethyl ether and air dried. ^{1}H-NMR (D_2O, 500 MHz): δ3.51 (m, 2H, NCH_2), 3.43 (m, 4H, NCH_2), 3.20 (m, 6H, NCH_2), 3.12 (t, 2H, NCH_2), 2.97 (t, 2H, NCH_2CCO_2), 2.86 (t, 2H, NCH_2), 2.83 (s, 3H, NMe), 2.82 (s, 3H, NMe), 2.78 (s, 3H, NMe), 2.60 (t, 2H, CH_2CO_2), 2.01 (m, 2H, $NCCH_2CN$), 1.83 (m, 2H, $NCCH_2CN$). MS (+ESI): *m/z* 315.2 [$(TMCPrA+2H)^+$]. Anal. Calcd. (found) for $C_{24}H_{38}F_{12}N_4O_{10}$: C, 37.41 (37.42); H, 4.97 (4.94); F, 29.59 (29.37); N, 7.27 (7.40); O, 20.76 (20.94).

Dissolution of the trifluoroacetate salt in methanol and addition of concentrated hydrochloric acid caused precipitation of a solid, which was isolated by filtration, washed with methanol, followed by diethyl ether, and air dried to give the title compound as a white powder (2.44 g, 77 % overall). ^{1}H-NMR (D_2O, 500 MHz): δ3.58 (m, 2H, CH_2), 3.50 (m, 4H, CH_2), 3.26 (m, 8H, NCH_2), 3.07 (t, 2H, NCH_2), 2.99 (t, 2H, NCH_2CCO_2), 2.86 (s, 3H, NMe), 2.85 (s, 3H, NMe), 2.81 (s, 3H, NMe), 2.65 (t, 2H, CH_2CO_2), 2.05 (m, 2H, $NCCH_2CN$), 1.90 (m, 2H, $NCCH_2CN$). Anal. Calcd. (found) for $C_{16}H_{38}Cl_4N_4O_2.3H_2O$: C, 37.36 (37.76); H, 8.62 (8.42); Cl, 27.57 (27.29); N, 10.89 (10.87).

Synthesis of Iron(II) Complexes (referred to by the iron(IV)-oxo complex #')

[**3'**][BPh_4]: To a methanolic suspension of TMCAcH.4HCl (0.63 g, 1.41 mmol) was added 4 equivalents of sodium methoxide (0.30 g, 5.63 mmol). After 15 minutes of stirring, all volatiles were removed to yield a residue, to which dichloromethane was added. This dissolved the monoprotonated ligand, but not the sodium chloride by-product, which was removed by filtration. The dichloromethane extracts were reduced to

dryness to provide TMCAcH as a waxy solid, which was then dissolved in methanol, treated with triethylamine (0.65 g, 6.40 mmol) and $Fe(OTf)_2(CH_3CN)_2$ (0.56 g, 1.28 mmol), and stirred for 12 hours. Subsequent addition of sodium tetraphenylborate (0.44 g, 1.28 mmol) caused precipitation of a white powder, which was isolated by filtration, washed with methanol and diethyl ether, and dried under vacuum to give 0.77 g of product (89 % yield). ^{1}H-NMR (CD_3CN, all peaks appear as broad singlets): δ342.9 (1H, CH_2), 337.3 (1H, CH_2), 335.8 (1H, CH_2), 322.6 (1H, CH_2), 193.2 (1H, CH_2), 167.0 (1H, CH_2), 155.2 (1H, CH_2), 146.3 (2H, CH_2), 131.8 (3H, N*Me*), 96.0 (3H, N*Me*), 88.2 (2H, CH_2), 81.7 (3H, N*Me*), 63.1 (1H, CH_2), 35.3 (1H, CH_2), 22.9 (3H, N*Me*), 7.4 (8H, BPh_4), 7.0 (8H, BPh_4), 6.9 (4H, BPh_4), -13.5 (1H, CH_2), -30.1 (1H, CH_2), -58.1 (1H, CH_2). MS (+ESI): *m/z* 355.3 [$(M\text{-}BPh_4)^+$]. Anal. Calcd. (found) for $C_{39}H_{51}BFeN_4O_2$: C, 69.45 (69.59); H, 7.62 (7.66); N, 8.31 (8.18). The analogous [**3'**][$B(C_6F_5)_4$] could be synthesized through a similar procedure, except replacing sodium tetraphenylborate with lithium tetrakis(pentafluorophenyl)borate diethyl ether complex.

[**7'**][BPh_4]: this complex was prepared in an analogous fashion to [**3'**][BPh_4], using 0.60 g (1.30 mmol) of TMCPrAH.4HCl and 0.21 g (5.21 mmol) of sodium hydroxide to provide the ligand TMCPrAH; and 0.60 g (5.92 mmol) of triethylamine, 0.52 g (1.18 mmol) of $Fe(OTf)_2(CH_3CN)_2$ and 0.41 g (1.18 mmol) of sodium tetraphenylborate in the subsequent complexation. The product was obtained as a white powder in 78 % yield (0.70 g). ^{1}H-NMR (CD_3CN, all peaks appear as broad singlets): δ 308.7 (1H, CH_2), 294.8 (2H, CH_2), 282.7 (1H, CH_2), 275.8 (1H, CH_2), 153.9 (1H, CH_2), 148.4 (1H, CH_2), 132.6 (3H, N*Me*), 121.0 (1H, CH_2), 112.1 (1H, CH_2), 103.1 (3H, N*Me*), 97.1 (3H, N*Me*), 68.0 (2H, CH_2), 51.2 (1H, CH_2), 34.2 (1H, CH_2), 26.9 (1H, CH_2), 20.7 (1H, CH_2), 15.6 (1H, CH_2), 12.6 (1H, CH_2), 7.4 (8H, BPh_4), 7.0 (8H, BPh_4), 6.9 (4H, BPh_4), -1.4 (1H, CH_2), -5.8 (1H, CH_2), -16.0 (1H, CH_2), -19.3 (1H, CH_2). MS (+ESI): *m/z* 369.1 [$(M\text{-}BPh_4)^+$]. Anal. Calcd. (found) for $C_{40}H_{53}BFeN_4O_2$: C, 69.78 (69.83); H, 7.76 (7.78); N, 8.14 (8.02). The analogous [**7'**][$B(C_6F_5)_4$] could be synthesized through a similar procedure, except replacing sodium tetraphenylborate with lithium tetrakis(pentafluorophenyl)borate diethyl ether complex.

[**8'**][BPh_4]: A mixture of TMC (0.20 g, 0.78 mmol) and iron(II) acetate (0.14 g, 0.78 mmol) were stirred together in methanol (10 mL) for 12 hours. Subsequent to filtration, the filtrate was treated with sodium tetraphenylborate (0.27 g, 0.78 mmol), which caused a white precipitate to form. This solid was isolated by filtration, washed with methanol (2 × 5 mL) and dried under vacuum to give the product as a white powder (0.45 g, 84 %). ^{1}H-NMR (CD_3CN, all peaks appear as broad singlets): δ 274.3 (4H, NCH_2), 109.7 (12H, N*Me*), 55.3 (4H, NCH_2), 40.1 (4H, NCH_2), 7.3 (8H, BPh_4), 7.0 (8H, BPh_4), 6.9 (4H, BPh_4), -9.4 (2H, CCH_2C), -10.2 (2H, CCH_2C). MS (+ESI): *m/z* 371.3 [(M-BPh_4)$^+$]. Anal. Calcd. (found) for $C_{40}H_{55}BFeN_4O_2$: C, 69.57 (70.03); H, 8.03 (8.10); N, 8.11 (8.14).

Iron(IV)-oxo Complex Synthesis

Synthesis of **3** and **7**: To acetonitrile solutions of iron(II) complex was added excess PhIO (approximately 3 equivs) and the resultant mixture was stirred together at ambient temperatures for 5 – 20 minutes. Subsequent removal of unreacted oxidant provided solutions of the desired complexes, suitable for spectroscopic and kinetic studies.

Synthesis of **8** and **9**: To preformed acetonitrile solutions of [Fe^{IV}(O)TMC(CH_3CN)]$^{2+}$ was added 2.5 – 5 equiv of tetrabutylammonium acetate or tetrabutylammonium propionate, dissolved in acetonitrile. This reaction proceeded smoothly at temperatures ≥ -20°C, but was prohibitively slow at lower temperature.

3.2.3 X-ray Crystallography

([**8'**][BPh_4] characterization was carried out by Victor Young)

Diffraction quality crystals of [**8'**][BPh_4] were grown by vapor diffusion of diethyl ether into concentrated CH_3CN solutions of complex. A crystal (approximate dimensions 0.25 x 0.21 x 0.13 mm^3) was placed onto the tip of a 0.1 mm diameter glass capillary and mounted on a Bruker CMOS diffractometer for a data collection at 123(2) K.[1] A preliminary set of cell constants was calculated from reflections harvested from three sets of 20 frames. These initial sets of frames were oriented such that orthogonal wedges of reciprocal space were surveyed. This produced initial orientation matrices determined from 782 reflections. The data collection was carried out using CuKα

radiation (graphite monochromator) with a shutterless data collection procedure. A randomly oriented region of reciprocal space was surveyed to the extent of one sphere and to a resolution of 0.84 Å. The intensity data were corrected for absorption and decay (SADABS).[2] Final cell constants were calculated from the xyz centroids of 9904 strong reflections from the actual data collection after integration (SAINT).[3]

For [**7'**][$B(C_6F_5)_4$], a concentrated solution in CH_3CN was layered with diethyl ether and put in a -40 C freezer for two years. Selected single crystals were placed onto the top of 0.1 mm diameter glass capillaries and mounted on a Bruker SMART V5.054 CCD area detector diffractometer for data collection. A preliminary set of cell constants was collected from reflections harvested from three sets of 20 frames. These initial sets of frames were oriented such that orthogonal wedges of reciprocal space were surveyed and then used to produce initial orientation matrices. Data collection was carried out using MoKα radiation (graphite monochromator). A randomly oriented region of reciprocal space was surveyed to the extent of one sphere, with four major sections of frames being collected using 0.30° steps in ω at four different ϕ settings and a detector position of -28° in 2θ. The intensity data were corrected for absorption and decay (SADABS). Final cell constants were calculated from the actual data collection after integration (SAINT).

The structures were solved and refined using Bruker SHELXTL. Space groups were determined based on systematic absences and intensity statistics. In all cases, a direct-methods solution was calculated, which provided most non-hydrogen atoms from the E-map. The remaining non-hydrogen atoms were located by full-matrix least squares/ difference Fourier cycles. All non-hydrogen atoms were refined with anisotropic displacement parameters. All hydrogen atoms were placed in ideal positions and refined as riding atoms with relative isotropic displacement parameters.

3.2.4 Resonance Raman Spectroscopy

Collection and analysis was performed by Jonathan Frisch.

Resonance Raman spectra were obtained using a liquid nitrogen cooled CCD detector (model LN/CCD-1340 × 400PB, Princeton Instruments) attached to a 1-m polychrometer (model MC-100DG, Ritsu Oyo Kogaku). An excitation wavelength of 406.7 nm was provided by a Kr^+ laser (Spectra Physics BeamLok 2060-RM) with *ca.* 20

mW power at the samples. All measurements were carried out in frozen solution with samples mounted on a brass cold finger. Raman shifts were calibrated with indene, and the accuracy of the peak positions of the Raman bands was ± 1 cm^{-1}. Samples of **3**, **7**,and **8** were prepared from 10 mM solutions of the corresponding iron(II) precursors, as described above. Samples of the ^{18}O-labelled isotopomers of **3** and **7** were generated by reaction with 2 equiv of $PhI(OAc)_2$, in the presence of 100 equiv of $H_2{}^{18}O$. In the case of **8**, generation of the precursor $[Fe^{IV}(O)TMC(CH_3CN)]^{2+}$ using $PhI^{18}O$ was found to preferable.

3.2.5 Mössbauer Spectroscopy

Data collection and analysis performed by Marlène Martinho and Eckard Münck.
The Mössbauer spectra were recorded with a home built spectrometer, using a Janis Research (Wilmington, MA) Super Varitemp dewar. Isomer shifts are quoted relative to Fe metal at 298 K.

3.2.6 DFT Calculations

Calculations performed by Marlène Martinho and Eckard Münck, except for **9**.

Gaussian was used for the calculations of **3**, **7**, and **8**, using a B3LYP functional with the basis set 6-311G and default settings for geometry optimizations. The initial coordinates were based on the crystal structure of [**8'**][BPh_4], as no iron(IV)-oxo complex was crystallized..

The structure for **9** was calculated by modifying the structure from **8** and using a mixed basis set with def2-SVP for all atoms except iron, for which def2-TZVP was used. The model was calculated in the triplet ground state using a b3-lyp functional, with an energy convergence of 10^{-7}.

3.2.7 Kinetic Experiments

PPh_3 reactions were conducted by Jason England, except for those of **9**.

Acetonitrile solutions of the iron(IV)-oxo complexes were generated as mentioned in the synthetic section. Stock solutions of 0.5 mM **3**, 1 mM **7**, 1 mM **6** were generated for each k_2 set with 1,4-cyclohexadiene. Displacement of the axial acetonitrile was achieved by addition of 2.5-3 equivalents of the proper tetraalkylammonium salt 2-4 minutes before addition of the substrate. Addition of the salt before temperature

equilibration was necessary for the lower temperature reactions. Each k_2 was generated from 4-5 time traces with differing concentrations of 1,4-cyclohexadiene. For NBu_4OPr substituted complex at 0 °C, high concentrations were too fast so 5-25 eq. was the range of substrate used; however, for all other runs, 10 eq. was the minimum substrate concentration. Dihydroanthracene reactions were conducted at 0.5 mM or 1 mM for the complexes. For the calculation of the Eyring parameters, all reactions were recorded at four temperatures with a span of 30 K. Each temperature was repeated 3 times, and fit with the exponential form in Origin 9.1 with $1/k_2^2$ weighting.

3.2.8 Cyclic Voltammetry

Scans were conducted at room temperature under a nitrogen atmosphere in a glove box or in a septumed vial under argon that had been sparged for 15 minutes. Scan rate of 100 mV/s was employed, unless otherwise noted. The electrolyte was 0.1 M NBu_4PF_6. The electrodes used were a glassy carbon electrode for the working electrode, a platinum wire for the auxiliary electrode, and a Ag/Ag^+ reference electrode with 0.1 M NBu_4PF_6 and 0.01 M $AgPF_6$ acetonitrile solution.

The iron(II) complexes were generated at 1 mM concentrations for the cyclic voltammograms. **3** and **7** were generated by addition of excess iodosylbenzene to a 1 mM acetonitrile solution of iron(II) complex, as reported in the synthesis section. **8** and **9** were generated by first generating **6** and then adding the appropriate tetraalkylammonium carboxylate salts at 3 minutes before scanning.

3.3 Results and Discussion

3.3.1 Characterization

3.3.1.1 X-ray Crystal Structures of Fe(II) Complexes

The crystal structures of [**7'**][$B(C_6F_5)]_4$ and [**8'**][BPh_4] both show 5-coordinate geometries in-between square pyramidal and trigonal bipyramidal ($\tau = 0.42$ and 0.46, respectively). Both cyclam rings are in the *trans*-I conformation (Figures 3.1 and 3.2). The bond lengths of the crystal structures and the paramagnetically shifted ^1H NMR spectra indicate that these are high-spin iron(II) complexes.

While [**7'**][$B(C_6F_5)]_4$ and [**8'**][BPh_4] could be crystallographically characterized, **3'** was highly disordered due to the co-crystallisation of enantiomers. Still, we were able to determine [**3'**][$B(C_6F_5)_4$] had 5-coordinate *trans*-I conformation (Figure 3.3). The same ligand, TMCAc, had been used previously by Wieghardt and co-workers to form iron complexes with *trans*-III geometries.[46] However, the Wieghardt complexes were synthesized from iron(III) starting materials, while [**3'**][$B(C_6F_5)_4$] has an iron(II) center. The larger iron(II) center may force the complex to adopt the *trans*-I conformation.

3.3.1.2 Spectroscopic Characterization

Upon addition of iodosylbenzene to **3'** and **7'** in CH_3CN, each formed a new species. These species exhibited near IR features similar to other reported S =1 iron(IV)-oxo complexes. These features are likely due to d-d transitions, which has been previously been reported as the source of the near IR features for iron(IV)-oxo complexes.[68] For **8'**, use of iodosylbenzene yielded similar features, but a higher yield was obtained with addition of NBu_4OAc to **6**. A similar method was used to generate **9**. All spectra exhibited a double-hump feature, which seems to be characteristic of iron(IV)-oxo species with axially ligated carboxylates.

Additional characterization of these complexes also indicated the formation of iron(IV)-oxo species. The electroscpray mass spectra of **3**, **7**, and **8** showed *m*/z values and isotope patterns consistent with the predicted formulas (Figures 3.S1-3.S3 in the appendix). Vibrations from 822-833 cm^{-1} were observed by resonance Raman spectroscopy (Table 3.1). These vibrations downshifted by 32-37 cm^{-1} upon ^{18}O-labeling, in accordance with Hooke's law. Moreover, the ^1H NMR indicated a single paramagnetic species of C_1 symmetry (Figure 3.S5-3.S6 in the appendix). Initial data for **9** indicates similar ^1H NMR spectrum.

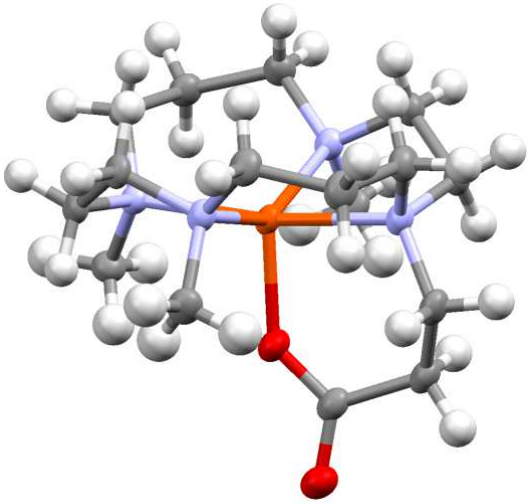

Figure 3.1: Crystal structure of [**7'**][$B(C_6F_5)_4$] with the counterion $[B(C_6F_5)_4]^-$ removed for clarity. Hydrogen atoms placed at idealized locations, ellipsoids at 50% probability.

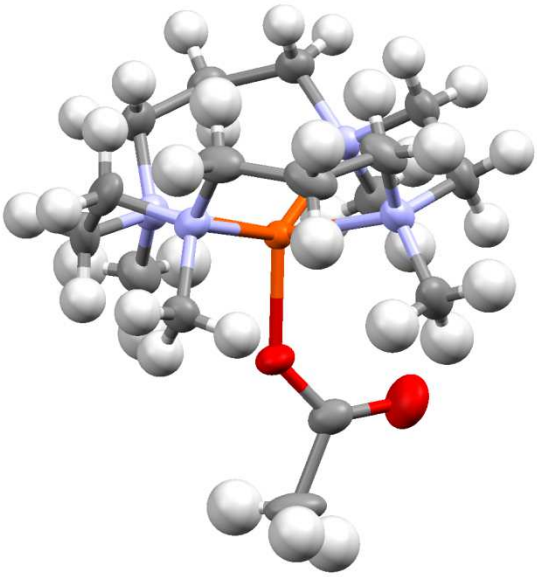

Figure 3.2: Crystal structure of [**8**'][BPh_4] with counterion $[BPh_4]^-$ removed for clarity. Hydrogen atoms placed at idealized positions, ellipsoids at 50% probability.

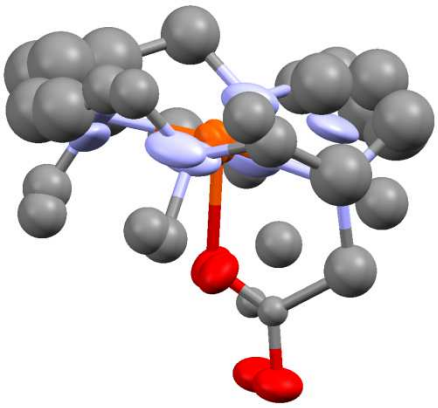

Figure 3.3: Disordered structure of [**3'**] with hydrogens and counterion removed for clarity. While there is disorder, the structure shows the three methyl groups *syn* to the acetate. Ellispoids are at 50% probability.

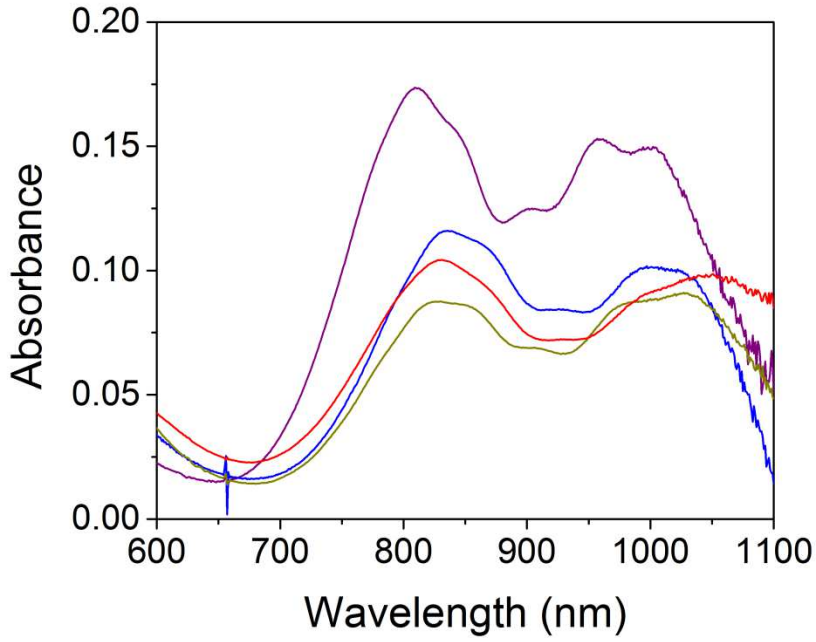

Figure 3.4: The electronic spectra of iron(IV)-oxo species recorded in CH_3CN solution at 0°C: **3** (purple), **7** (dark yellow) **8** (blue), and **9** (red).

Table 3.1: Spectroscopic properties of the iron(IV)-oxo carboxylate series

Complex	**λ_{max}, nm (ε_{max}, M^{-1} cm^{-1})**	**$\nu_{Fe=O}$ (cm^{-1})**	ΔE_Q (mm/s)[b]	δ (mm/s)[b]
3	811 (180) 962 (160)	831	0.74 (-0.14)	0.13 (0.14)
7	831 (110)[#] 1033	822	0.82 (0.13)	0.17 (0.17)
8	831 (160) 997 (140)	826	0.99 (0.38)	0.19 (0.18)
9	830	N/A	N/A*	N/A

Estimation based on quantification of $OPPh_3$ after reaction with PPh_3.

*No Mössbauer data

3.3.1.3 Mössbauer Spectroscopy

(This work and analysis was contributed by Marlène Martinho and Eckard Münck)

Zero-field Mössbauer studies of **3**, **7**, and **8** show that they exhibit quadrupole doublets indicative of an integer spin ground state, with isomer shifts δ typical of iron(IV). Fitting of the high-field spectra of these complexes provided zero-field splitting and hyperfine parameters similar to those of previously reported S = 1 oxoiron(IV) complexes. Unsurprisingly, the zero field spectrum of **3** displayed a doublet with δ = 0.13 mm s^{-1} and ΔE_Q of 0.74 mm s^{-1}, typical of an anion bound oxoiron(IV) complexes with TMC-based ligands. Notably, an increase was observed in both δ and ΔE_Q upon increasing the length of the pendant donor arm to the propionate-appended complex **7** (δ = 0.17 mm s^{-1} and ΔE_Q = 0.82 mm s^{-1}), and moving to the non-appended acetate complex **8** (δ = 0.19 mm s^{-1} and ΔE_Q = 0.99 mm s^{-1}). Given that the magnitude of ΔE_Q can crudely be viewed as a reflection of the degree of asymmetry in the electron density around the iron center and δ is inversely related to the electron density at the iron nucleus, the smaller ΔE_Q and δ seen in the TMCAc complex is partially a reflection of the slightly greater donor strength of the appended acetate, relative to the other carboxylate bound complexes **7** and **8**. This is presumably a consequence of the small 5-member chelate ring formed by coordination of the appended acetate in **3** and any conformational changes in the cyclam ring that result. This slightly greater donor strength is also observed in cyclic voltammetry experiments (*vide infra*).

3.3.2 Reactivity

In previous work, a series of TMC-based iron(IV)-oxo complexes had been found to exhibit an anti-electrophilic pattern to HAT reactivity, which was explained by the Two-State Reactivity model, but subsequent work has shown that the reactivity of TMC-based iron(IV)-oxo complexes is more complicated.[26–28,60] Given that no single trend based on the electrophilic nature of the complexes was found, we set out instead to investigate how changing structural components of the TMC framework affects reactivity with a series of axially bound carboxylate complexes.

As previous work connected the electron donating power of the axial ligand with $E_{p,c}$ peak from cyclic voltammetry,[26] the same method was chosen to compare the new carboxylate series. It was found that of **3**, **7-9** exhibited $E_{p,c}$ values very similar to each other (see Table 3.2) with the complex with the appended acetate having the lowest value of -920 mV vs Fc^+/Fc and the free acetate anion complex having the highest value at -790 mV vs Fc^+/Fc. While there is some difference among these complexes, the span of 130 mV is small, indicating that the electron donating power of the carboxylate changes little with the structural changes.

Oxygen atom transfer (OAT) reactivity within the carboxylate series in the reactions with PPh_3 showed two orders of magnitude difference between the slowest complex (**3**) and the fastest (**9**) (Table 3.2). The appended complexes were slower, with **3** having a k_2 of 0.006 M^{-1} s^{-1} and **7** a k_2 of 0.071 M^{-1} s^{-1}, while the free anion complexes showed similar k_2 of 0.57 M^{-1} s^{-1} for **8** and 0.64 M^{-1} s^{-1} for **9**. A comparison with $E_{p,c}$ values indicates that a higher OAT rate corresponds to a higher redox potential. This electrophilic trend for these carboxylate complexes is similar to what has been reported before for other iron(IV)-oxo complexes, especially those employing the TMC framework (Figure 3.5).[26,28] The consistency in OAT towards the electrophilicity of iron(IV)-oxo moieties shows that electrophlicity of iron(IV)-oxo TMC-based complexes is predictive of OAT reactivity.

Surprisingly, HAT reactivity was also found to be correlated with $E_{p,c}$ values. For 1,4-cyclohexadiene (CHD), the order of reactivity was **3** (0.023(1) M^{-1} s^{-1}) < **7** (0.33(6) M^{-1} s^{-1}) < **8** (3.6(2) M^{-1} s^{-1}) < **9** (4.3(2) M^{-1} s^{-1}). A similar trend was seen in the reactivity of 9,10-dihydroanthracene (DHA), with an order of **3** (0.044) M^{-1} s^{-1}) < **7** (0.66(4) M^{-1} s^{-1}) < **9** (10.9(6) M^{-1} s^{-1}) < **8** (13(1) M^{-1} s^{-1}). While the order of reactivity of **8** and **9** switches between CHD and DHA, the rate constants are almost within error of each other, indicating that the extra methylene group does not change reactivity much. However, there was a hundred-fold increase in the reactions with DHA and CHD from the appended acetate complex, **3** to the free anion acetate, **8** (Table 3.2). This difference does not follow the anti-electrophilic trend proposed previously (Figure 3.6), as **3** has the

least electrophilic iron(IV)-oxo moiety and is the least reactive. This indicates that electron donating power of the axial ligand is not the reason for the reactivity differences.

While TSR has been proposed previously to explain the differences in reactivity, there are other models about what controls the reactivity of iron(IV)-oxo complexes. Bond strength, for example, is often correlated with reactivity. Probing this can be accomplished with resonance Raman spectroscopy. Iron(IV)-oxo frequencies were obtained for **3** (831 cm^{-1}), **7** (822 cm^{-1}) and **8** (826 cm^{-1}). The resonance Raman frequencies, when compared to reactivity show no trend, with the most reactive species, **8**, having the intermediate frequency. The frequencies are also very similar, which may indicate similar bond strength between the iron(IV)-oxo species. From resonance Raman spectroscopy, there is no evidence that Fe-O bond strength determines the reactivity.

Steric factors could be different among these complexes. We investigated this by use of DHA as well as CHD, where DHA is bulkier, though it has a BDE of 76.3 kcal/mol, which is practically indistinguishable from the BDE of 76.0 kcal/mol of CHD. However, little difference was seen in the reactivities of each of these complexes with these two substrates (Figure 3.7). It seems unlikely that sterics is the major cause in the changes in reactivity.

A recent addendum to TSR theory indicates that tunneling plays a major role in determining the reactivity of these different TMC-based complexes, and may account for the reverse of an expected electrophilic trend. While not applicable in OAT, the hydrogen atom is small enough that HAT rates may increase due to a tunneling contribution. This contribution alters what is expected from different iron(IV)-oxo complexes. To test how much tunneling is affecting the reactivity, we performed KIE studies on the carboxylate complexes with DHA. All had KIE values greater than 7, indicative of tunneling. However, the KIE values fall within a small range (15-30) indicating that tunneling contributes similarly to the HAT reactivity of all complexes. While the most reactive complex, **8**, does have a KIE value of 30, the lowest value of 15 is for both the second most reactive species **9** and the estimation for the least reactive species **3**. The KIE values also do not follow the predicted anti-electrophilic trend. Instead of the most electron-donating ligands having the highest KIE value, the highest KIE found here was due to the

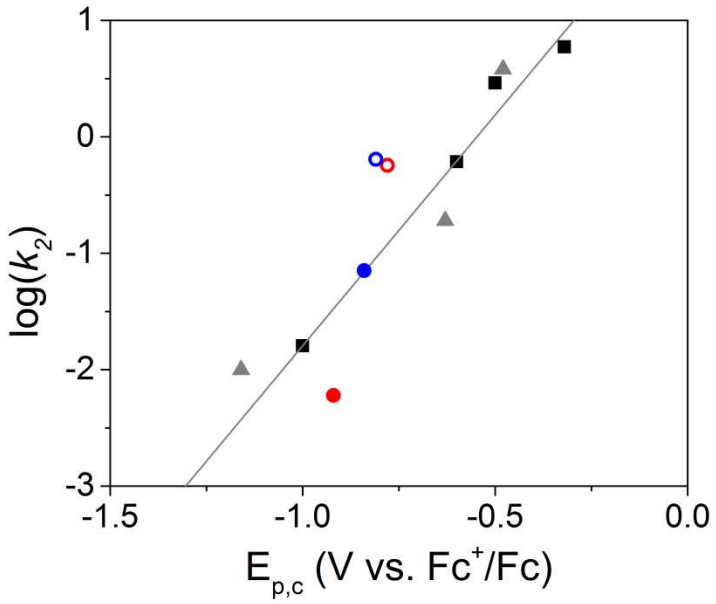

Figure 3.5: Log of the rate constant of OAT from TMC-based iron(IV)-oxo complexes versus the reductive peak from cyclic voltammetry. Black, Sastri *et al.*; grey, England *et al.*; red filled, **3**; blue filled, **7**; red open, **8**; blue open, **9**.

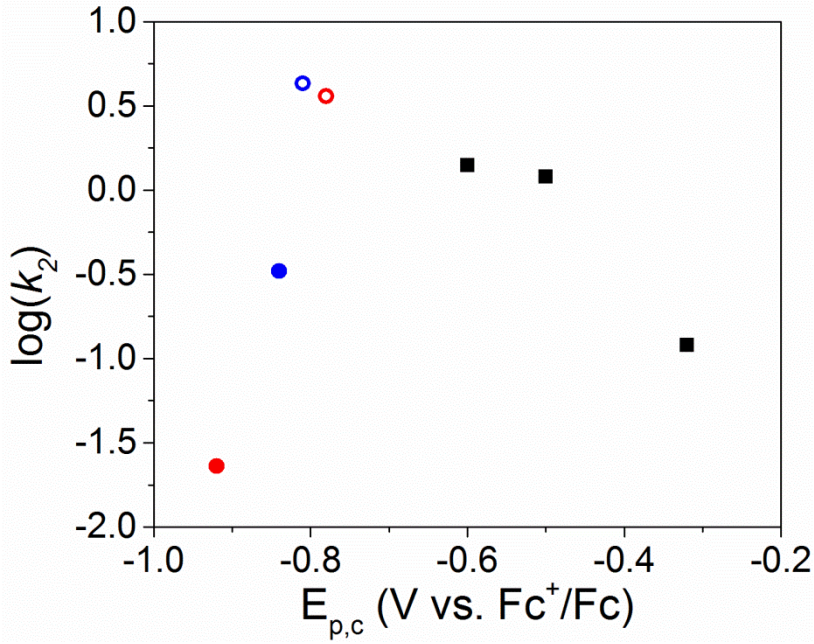

Figure 3.6: Log of HAT rate constants of 1,4-cyclohexadiene with iron(IV)-oxo species from this study (circles) and a previous study (black squares) versus $E_{p,c}$ shows no correlation between iron(IV)-oxo TMC-based complexes: red filled, **3**; blue filled, **7**; red open, **8**; blue open, **9**.

least electron-donating ligand, as indicated by $E_{p,c}$ values. While there are some differences, small changes in the reaction rate create large differences in KIE. The large reactivity difference between the free anion complexes compared to the tethered complexes cannot be explained by invoking tunneling.

These tests of previous models indicate that the reactivity of these complexes is controlled by a factor outside of tunneling, sterics, or bond strength. We instead turned to computational and experimental methods of understanding the transition states of these complexes to better understand what factor contributes to the hundred-fold difference in reactivity.

3.3.3 Transition State Investigations

The Eyring equation provides a useful way to experimentally probe the difference between the ground state and the transition state energy. While this is the best way to gather information about the transition state experimentally, several concerns arise with the experimental implementation and reliability of the parameters obtained. To avoid these concerns, we followed the best practices outlined previously.[69] A short explanation of the new way of fitting the data is instructive for others who attempt to calculate Eyring parameters, as several literature sources have utilized less reliable methods.

Although it is generally known that linearization of exponential equations leads to less reliable parameters, this has been shown to be less important for the Eyring equation.[69] Comparing the parameters calculated in three different ways from our own study shows that little error is indeed present, as has been mentioned previously, but to err on the side of caution, the best fit with the exponential equation was chosen. These parameters are all calculated at four different temperatures over a range of 30 K and repeated three times. As can be seen in Table 3.4, the errors for the entropy of activation are in the range expected as compared to those from the enthalpy of activation ($\text{error}\Delta H^{\ddagger} \approx 0.003\ K^{-1}\text{error}\Delta S^{\ddagger}$).[70] These values have been carefully and rigorously determined, allowing for the full use of errors in analysis.

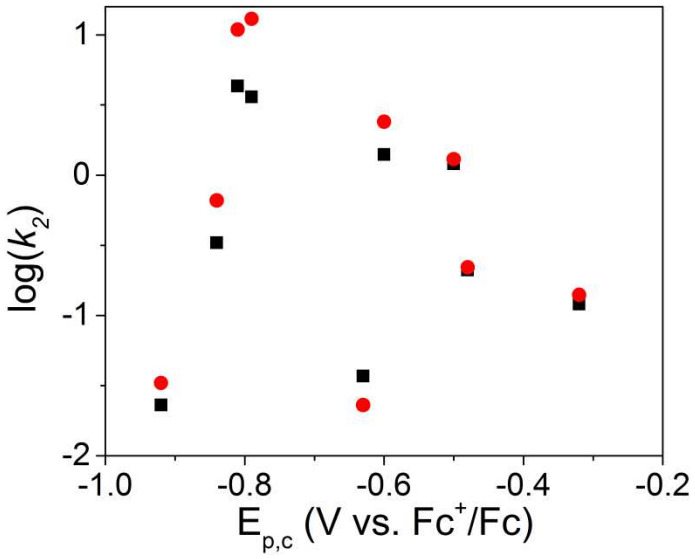

Figure 3.7: The log of HAT rate constants for all published iron(IV)-oxo TMC-based complexes (in order of decreasing $E_{p,c}$ value: **6**, **5**, $[Fe^{IV}(O)TMC(OOCCF_3)]^{2+}$, $[Fe^{IV}(O)TMC(N_3)]^{2+}$, **1**, **8**, **9**, **7**, **3**) with 1,4-cyclohexadiene (black) and 9,10-dihydroanthracene (red). The rates between DHA and CHD are similar for each complex.

Table 3.2: Reactivity and electrochemistry of the carboxylate series

Complex	k_2 PPh_3 ($M^{-1}s^{-1}$)	k_2 1,4-CHD ($M^{-1}s^{-1}$)	k_2 DHA ($M^{-1}s^{-1}s^{-1}$)	$E_{p,c}$ (V)	KIE DHA
3	0.006	0.023(1)	0.033(4)	-0.92	~15*
7	0.071	0.33(6)	0.66(4)	-0.84	*21*
8	0.57	3.6(2)	13(1)	-0.79	*30*
9	0.64(2)	4.3(2)	10.9(6)	-0.81	*15*

* Only estimation based on 100 eq. d^4-DHA due to long reaction time

Table 3.3: DFT geometry values

Complex	Fe=O	Fe-Ocarb	Angle O=Fe-O	Average Fe-N distance
3	1.67	1.93	176	2.10
7	1.67	1.90	179	2.12
8	1.66	1.96	174	2.13
9	1.66	1.96	174	2.13

Table 3.4: Eyring Parameters Determined with Exponential equation

Complex	$\Delta S^{\ddagger}$ (J*mol^{-1}*K^{-1})	$\Delta H^{\ddagger}$ (kJ/mol)
3	-119 ± 6	43 ± 2
7	-108 ± 7	39 ± 2
8	-115 ± 6	32 ± 2
9	-108 ± 5	34 ± 2

Table 3.5: Eyring Parameters Determined with Linear Equation

Complex	$\Delta S^{\ddagger}$ (J*mol^{-1}*K^{-1})	$\Delta H^{\ddagger}$ (kJ/mol)
3	-119 ± 5	43 ± 2
7	-106 ± 6	40 ± 2
8	-114 ± 6	33 ± 2
9	-106 ± 5	34 ± 1

The importance of using the exponential equation instead of the linear equation can be seen with comparison of the entropy of activation. With the normally used linear equation, $\Delta S^{\ddagger}$ = -106 ± 6 J/mol·K for **7** and $\Delta S^{\ddagger}$ = -106 ± 5 J/mol·K for **9**, which is different from the value for **3** of -119± 5 J/mol·K (Table 3.5). This would suggest some entropic component to the reactivity. However, when the exponential equation is used, the entropy of activation is within error for all complexes (Table 3.4). The error for this value is small for each, but all complexes are within error of each other, indicating that the major difference in activation energy is not from the entropic component.

Using the more reliable determination method, the entropy of activation parameter is large and negative for all complexes from -108(7) to -119(6) J/mol·K, which is consistent with a bimolecular reaction. As they are all within error of each other, this indicates that the entropic component is not what controls the reactivity of these complexes.

Instead, both free anion complexes show lower enthalpies of activation (32(2) kJ/mol for **8** and 34(2) kJ/mol for **9**) than the appended complexes (43(2) kJ/mol for **3** and 39(2) kJ/mol for **7**). The difference seen between the reactivity of the appended and the unappended complexes is therefore due to these enthalpic differences.

To gain insight into what causes the differences in enthalpy of activation, we turned to DFT. Calculations indicate that the iron-oxo bond lengths are the same within error (1.66 – 1.67 Å), the O-Fe-O bond angle is nearly 180 ° for all complexes (174 –

179), and the average Fe-N distance varies little (2.10 – 2.13 Å). The largest change is seen in the axial carboxylate ligand, from 1.90 – 1.96 Å, which is still small. This distance also does not correlate with reactivity. Instead, **7** has the shortest Fe-$O_{carboxyate}$ bond length at 1.90 Å, **3**, the next longest at 1.93 Å, and **8** and **9** are the longest at 1.96 Å. Given these similar geometries, it seems unlikely that the geometry of the reactant ground state is responsible for the differences in reactivity.

For these reasons, we propose it is the attachment of the axial ligand that increases the enthalpy of activation. As the geometries are minimally different in the ground state between the appended and unappended complexes, it is likely the geometry of the transition state that is affected. More bonding interactions are likely to be weakened in the transition state. This can be accomplished if the iron(IV)-oxo moiety has to lift out of the N-plane of the TMC ligand as the Fe=O moiety abstracts an H-atom from the substrate. With the unappended anionic axial ligands, this shift is easily accomplished as only minor steric interactions would interfere. However, with a constrained system, such as the appended ligand, the bond between the axial ligand and the iron might need to weaken for the correct transition state to be obtained. This explanation also explains the 10-fold difference in HAT reactivity seen between **3** and **7**, as **7** has a longer appending arm, and therefore is more flexible. Although the enthalpies of activation are within error for these complexes, this change would be a combination of enthalpic and entropic factors, which may appear within error of each other.

The difference between unappended and appended ligands shows up in the currently reported iron(IV)-oxo species utilizing the TMC-framework. If species are divided up into those with appended ligand and those without, the anti-electrophilic trend reported by Sastri *et al*. holds only for the free anion complexes from this study. However, comparing the other complexes as a group shows no anti-electrophilic trend, and even an electrophilic trend if only complexes with axial ligands that form five-membered rings are considered. These subset shows the importance of comparing related complexes, as even connecting the anion to the ligand framework alters reactivity greatly.

3.4 Conclusion

We have synthesized a series of TMC-based iron(IV)-oxo complexes with axially coordinated carboxylate ligands. There was over a hundred-fold OAT and HAT reactivity difference between the slowest iron(IV)-oxo species, **3**, and the fastest, **8** and **9**. No anti-electrophilic HAT trend was seen with reduction potential, the second TMC-based series to contradict the original correlation between HAT and $E_{p,c}$ values. While tunneling was a factor in HAT for all the complexes, a small range of values (15-30) was obtained, with no trend related to the increase in reactivity. Instead, Eyring parameters revealed a significant difference between the enthalpies of activation for the appended carboxylate complexes versus the unappended carboxylate complexes. The increase in enthalpy of activation for the appended complexes is proposed to be due to the iron(IV)-oxo moiety rising out of the plane. This weakens the axial bond in the appended complexes, as the appending does not allow as great a movement of the axial ligand. Therefore, the design of new ligands must not only focus on the axial ligand electron-donating capability, but also the connection, or lack of one, towards the overall ligand framework.

Chapter 4

Evidence of Radical Formation in Oxygen Activation of Nonheme Iron Model Complexes

4.1 Introduction

Nonheme monoiron enzymes activate dioxygen to form putative iron(IV)-oxo intermediates that are proposed to break the strong C-H bonds of a variety of substrates.[1,71,72] Iron(IV)-oxo intermediates have been trapped in enzymes[4,6,9,12,13] and shown to convert substrates to their final product. These iron enzymes generate the iron(IV)-oxo intermediate by the cleavage of dioxygen, presumably through a peroxo intermediate.[1] Mimicking the oxygen activation of these nonheme iron enzymes with synthetic model complexes is one step towards the goal of using oxygen for the activation of strong C-H bonds using synthetic catalysts.

A proposal for activation of oxygen in nonheme iron enzymes involves the initial binding of dioxygen to the iron(II) center to form an iron(III)-superoxo complex; this superoxo complex can bind to a carbon or hydrogen atom to form the putative iron(III)-peroxo intermediate. The iron(III)-peroxo intermediate decays through either homolytic cleavage or, upon the addition of a proton and an electron, heterolytic cleavage. The decay product is the iron(IV)-oxo intermediate.

While synthetic model complexes have been proposed to activate dioxygen in this way as shown in Scheme 4.1,[33,36,38] recent studies implicated peroxyl radical formation as part of the mechanism for the activation of dioxygen,[73,74] where the formation of either peroxyl radicals or their peroxide products are responsible for the iron(IV)-oxo complex formation. For example, in a reaction with isopropanol, $[Fe^{IV}(O)TMC(NCCH_3)]^{2+}$ (**6**) was generated in the presence of dioxygen through two proposed mechanisms.[73] Although initial formation of some iron(IV)-oxo complex from a peroxo intermediate was proposed (Scheme 4.2), only a small amount of the oxoiron(IV) species formed through this mechanism. The small amount of **6** initiated a radical pathway by abstracting a hydrogen atom from isopropanol to form hydroxyisopropyl radicals and an iron(III)-hydroxo species. The hydroxyisopropyl radical reacts with oxygen to form a peroxyl radical. This species then decays to a hydroperoxyl radical and acetone. The hydroperoxyl radical abstracts a hydrogen atom from another isopropanol to generation hydrogen peroxide and hydroxyisopropyl radical. The majority the iron(IV)-oxo complex

formed was proposed to be the result of the reaction of $[Fe^{II}TMC(NCCH_3)]^{2+}$ (**10**) with hydroperoxide generated from hydroxyisopropyl radicals.

Likewise, Comba found that the reaction rates of iron(II)-bispidine complexes with dioxygen and 1,2-dimethylcyclohexane depended on the purity of the substate and the presence of radical scavengers, or of radical initiators.[74] While this work was in progress, the Nam and Fukuzumi groups also investigated the $Sc(OTf)_3$ and $NaBPh_4$ system with oxygen and showed that it likely also was radical based.[39] While they did react triflic acid with $NaBPh_4$ in the presence of **10** and O_2, the reaction was not extensively investigated.[39]

Because of these new findings, we reinvestigated the reaction of **10** and oxygen under two reaction conditions: in the presence of strong acid with BPh_4^- and in the presence of cycloalkenes. These systems showed sensitivity to radical initiators, traps, and/or substrate purity, like those reported by Nam, Fukuzumi, and Comba. Taken together, the accumulated data indicate a universal mechanism of dioxygen reacting with autoxidizable substrate to generate peroxyl radicals, which are crucial to the formation of the iron(IV)-oxo product in these synthetic systems.

4.2 Experimental

All chemicals were purchased from Sigma-Aldrich unless otherwise stated. $Fe(OTf)_2(CH_3CN)_2$, was prepared according to previously reported procedures.[47] TMC was purchased from Angene International Limited or Strem. $[FeTMC(CH_3CN)](OTf)_2$ was prepared by the method outlined in chapter 2. Galvinoxyl radical was purchased from TCI America. 2,6-di-*tert*-butyl-4-methylphenol was purified according to previously published methods.[75] Cyclohexene was either used directly from Sigma-Aldrich (99 %) as noted or was run through an alumina column prior and vacuum distilled before use. It was stored under argon in a -80 °C freezer. Cyclooctene was purchased from Sigma-Aldrich (99 % or ≥99.5 %) and used with and without alumina column purification as noted.

Scheme 4.1: Previously proposed oxygen activation mechanism for **10** with a hydrogen atom source or a proton source and an electron source.

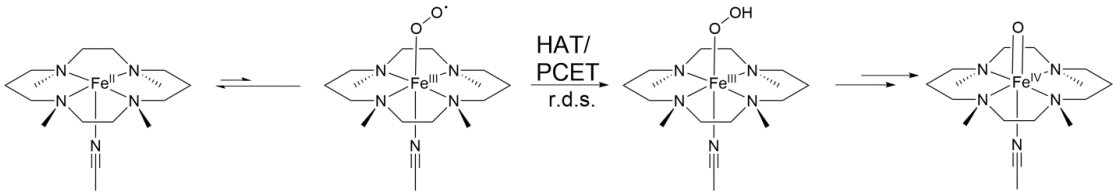

Scheme 4.2: Proposed reactivity of **10** with oxygen in the presence of isopropanol. Reproduced with permission from Morimoto, Y.; Lee, Y.-M.; Nam, W.; Fukuzumi, S. *Chem. Commun.* **2013**, *49* (25), 2500–2502. Copyright © 2013 Royal Society of Chemistry.

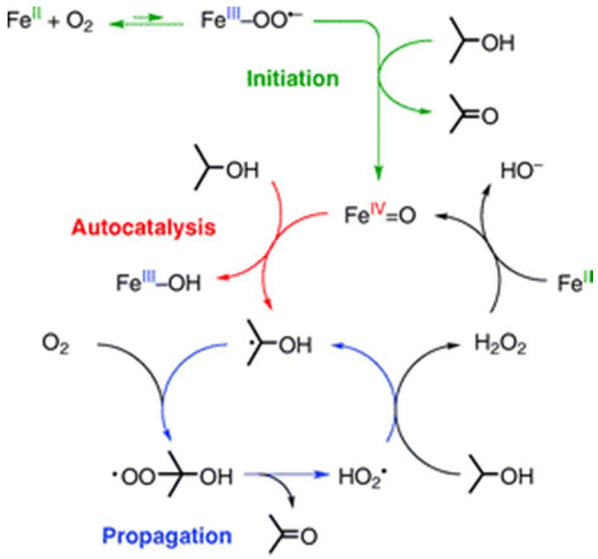

All reactions were recorded using a HP8453A diode array spectrometer with a cryostat from Unisoku Scientific Instruments (Osaka, Japan) that maintained temperature at 0 °C or 25 °C as necessary. A Bruker AV-500 NMR instrument was employed for detecting products. GC analysis of products was conducted using Perkin-Elmer Sigma 3 gas chromatograph (AT-1701 column, 30 m) with a flame ionization detector. Identification of possible impurities of cyclohexene were conducted by the Mass Spectrometry laboratory at the University of Minnesota using a Finnigan MAT 95.

All $FeTMC(OTf)_2$ samples were dissolved in anhydrous acetonitrile. Individual 2 mL samples were either exposed to air for 15 minutes for air saturated conditions or bubbled with oxygen for one minute prior to introduction of the substrates. Perchloric acid (70%) was diluted with acetonitrile for a 0.1 M stock solution. Sodium tetraphenylborate was dissolved in acetonitrile for a 0.1 M stock solution. After reactions, GC determinations were conducted after an esterification procedure used by our lab previously[76] or were determined by ^1H NMR using non-deuterated solvents spiked with 1,1,2,2-tetrachloroethane (D1 = 30 seconds, 64 scans).

4.3 Results and Discussion

4.3.1 Hydrogen Atom Transfer

Previously, Nam reported the reaction of cycloalkenes with **10** under air that showed rapid production of **6**.[38] This rate was shown to depend on the strength of the allylic C-H bond and a kinetic isotope effect (KIE) of 6.3(3) was reported for cyclohexene, showing that C-H bond cleavage was an important component of the rate-determining step.[38] It was postulated that this step involved an incipient iron(III)-superoxo species.[38] However, this species was never detected. With reinvestigation of this system, we detected no superoxo species, but rather found evidence for a radical mechanism.

Addition of cyclohexene directly from a commercial source to **10** under air, using the conditions reported previously, generated **6** with a rate constant of 0.70 M^{-1} s^{-1}, which is similar to the value reported by the Nam group of 1.2 M^{-1} s^{-1}.[38] Addition of the radical scavenger galvinoxyl resulted in the observation of a lag phase (Figure 4.1), indicating

that a radical chain reaction may be occurring. While some initial absorbance at 820 nm was seen (Figure 4.1), this was not due to the formation of **6**; rather, the galvinoxyl radical absorbs in that region as well. This can be seen by comparing the 820 nm absorbance with the other absorbance feature of the galvinoxyl radical at 428 nm, which decreases to the point where the 820 nm absorbance reaches the minimum before increasing again (Figure 4.3). Given this information, a more thorough investigation of a possible radical mechanism was carried out.

Interestingly, as also found in the Comba study on 1,2-dimethylcyclohexane oxidation, purification of the substrate made a significant difference in the reaction rate and the length of the lag phase. Upon passing cyclohexene through an alumina column and vacuum distilling prior to use to remove minor impurities, a lag phase of ~500 s was seen in the reaction in air with **6** (Figure 4.2, black), and the observed sigmoidal time course is typical of autocatalytic reactions.[77] GCMS analysis of the cyclohexene substrate showed far fewer impurities in the purified sample than in the original bottle from our commercial source, suggesting an impurity in the substrate was acting as a radical initiator. ^{1}H NMR showed a peak corresponding to 2-cyclohexen-1-ol in the unpurified substrate, while GCMS analysis indicated a number of impurities, some of which could easily be obscured by cyclohexene peaks in the ^{1}H NMR spectrum.

Indeed, addition of 2-cyclohexen-1-ol or 1,3-cyclohexadiene affected the reaction. Addition of 2-cyclohexen-1-ol to the reaction showed an increase in reaction rate and no lag phase (Figure 4.2, red). Addition of 1 equiv. 1,3-cyclohexadiene showed an even higher reaction rate with no lag phase (Figure 4.2, blue), indicating both compounds could be acting as radical initiators, given their having weaker C-H bonds than cyclohexene. These impurities or similar impurities in the cyclohexene likely act as radical initiators and give the reactivity seen upon exposure to air in the presence of **10**.

The difference observed upon use of radical scavengers and the presence of impurities in the original reaction suggests that peroxyl radicals are generated and a peroxyl radical binds to the iron center of **10** (Scheme 4.3). This is in accordance with what has been seen in the previous studies implicating radicals.[73,74] It is interesting to note that the likely impurities in cyclohexene that induce autoxidation are also the

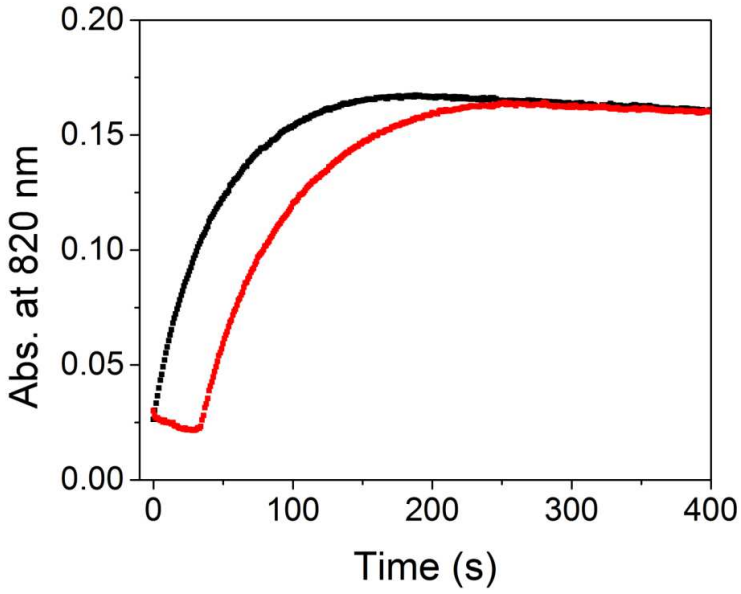

Figure 4.1: Time course at 820 nm of 0.5 mM **10** under air at 25 °C with ~100 eq. cyclohexene in the presence (red) and absence (black) of 13 μM galviinoxyl radical. The slight increase at 820 nm at the start of the reaction with galvinoxyl is due to some absorbance of the radical at 820 nm. The lag time between the two reactions indicates that the galvinoxyl radical delays the reaction, indicating the presence of radical formation prior to formation of **6**.

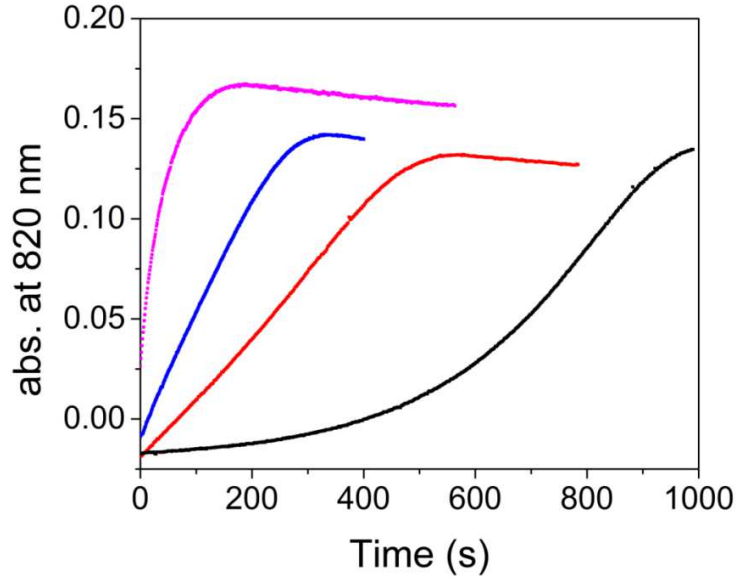

Figure 4.2: Time course of the reactions of ~100 eq. cyclohexene with 0.5 mM **10** under air at 25 °C under varying conditions: magenta, cyclohexene used from new bottle from Sigma-Aldrich; black, cyclohexene purified by passing through an alumina column and vacuum distilling prior to reaction; red, addition of 2 eq. 2-cyclohexene-1-ol with the purified cyclohexene; blue, addition of 1 eq. 1,3-cyclohexadiene with the purified cyclohexene. It should be noted that 1,3-cyclohexadiene can only be purchased with the radical scavenger 2,6-di-*tert*-butyl-4-methylphenol as a stabilizer.

products of autoxidation.

Cyclooctene shows similar results. When radical traps are used, there is a decrease in the rate of formation of **6** (Figure 4.5). Even when using the highest purity available (≥99.5%), there is a distinct difference between when cyclooctene is purified first by an alumina column for the reaction and when a fresh bottle of cyclooctene is used for the stock solution (Figure 4.4). Trace impurities are therefore likely the radical initiators present and may account for the differences in reactivity seen in the original experiments reported by Nam and co-workers.

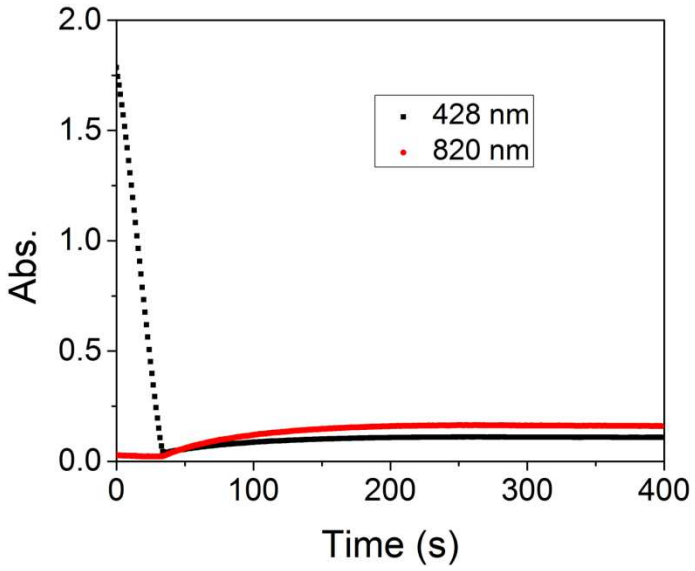

Figure 4.3: Time traces at 428 nm and 820 nm for the reaction of ~100 equiv. cyclohexene with 0.5 mM of **10** in the presence of 13 μM galvinoxyl radical under air at 25 °C. The absorbance at 428 nm is attributed the galvinoxyl radical, which decreases, along with some absorbance at 820 nm, until both disappear, and the feature that corresponds to **6** grows in.

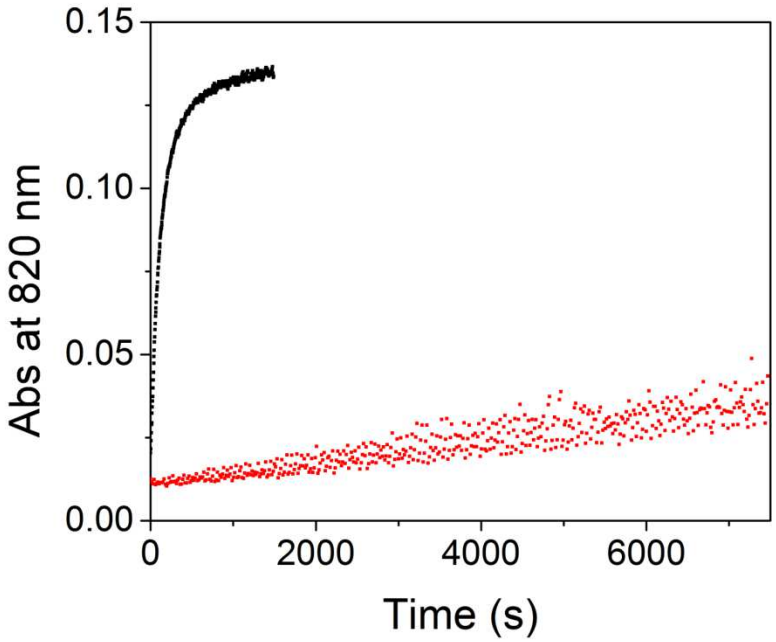

Figure 4.4: Time course at 820 nm of 0.5 mM **10** under air at 25 °C with ~100 eq. cyclooctene when cyclooctene is used without further purification (black) and when cyclooctene is purified by alumina column (red).

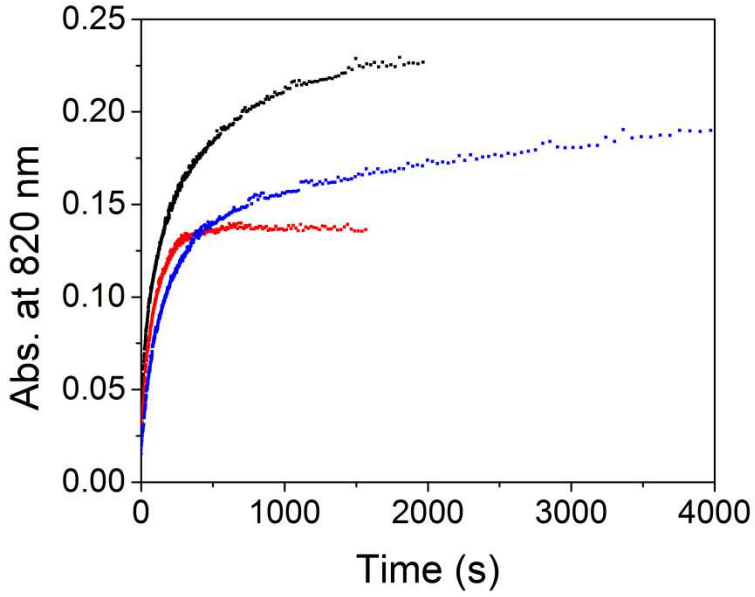

Figure 4.5: Time course at 820 nm of 0.5 mM **10** under air at 25 °C with ~100 eq. cyclooctene in the absence (black) and presence of 1 eq. 2,6-*tert*-butyl-4-methylphenol (red) or 1 eq. diphenylamine (blue). Both the rate of reaction decreases as well as the yield.

Scheme 4.3: Proposed mechanism for **10**, cyclohexene and oxygen.

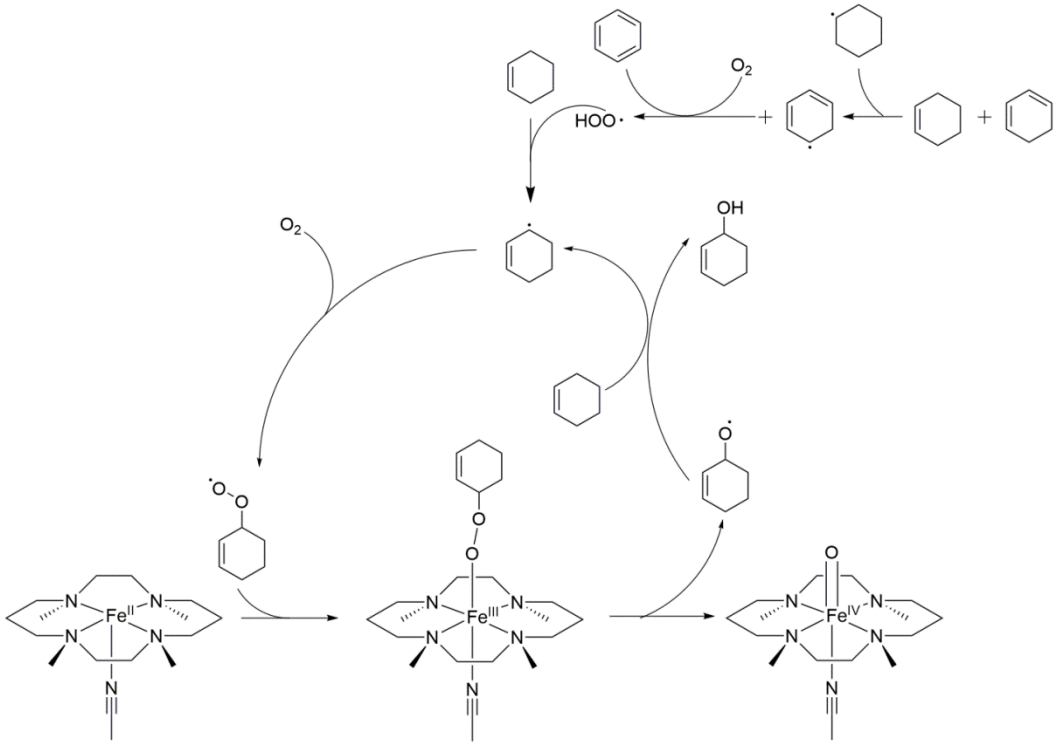

4.3.2 Proton Coupled Electron Transfer

Previously, **6** was reported to form in the reaction of **10** and dioxygen in the presence of $NaBPh_4$ and either $HClO_4$ or $Sc(OTf)_3$.[33,36] As Nam and Fukuzumi recently reported an evaluation of the mechanism with Sc^{3+},[38] the mechanism with perchloric acid will be the focus of the next part.

For the reaction with **10**, $NaBPh_4$, $HClO_4$, and O_2, we conducted some control experiments, the results of which are listed in Table 4.1. Under oxygen saturated conditions at 0 °C, addition of 1 equiv. $NaBPh_4$ and 1 equiv. $HClO_4$ to a 1 mM solution of **10** in CH_3CN afforded **6** in~75%-80% yield based on the intensity of the near-IR band; 0.6 mM biphenyl and ~0.6 mM of phenol were also formed as byproducts based on GC analysis. Surprisingly, comparable amounts of biphenyl(~0.5 mM) and phenol (0.6 mM) were obtained under the same conditions but in the absence of **10**. When no iron or acid was present, $NaBPh_4$ did not react with O_2.

Given the fact that GC analysis relies on an additional esterification step, the products of reaction were also determined by ^1H NMR. Phenol and biphenyl were observed as products when BPh_4^- was exposed to O_2 and strong acid without **10**, and in

relatively similar yields to when **10** is present (see Table 4.1). Interestingly, there were also peaks present that correspond to diphenylborinic acid. TOCSY showed a connection of a 7.75 doublet to peaks from 7.37 to 7.52 ppm (Figure 4.6), which is similar to the values reported for diphenylborinic acid. Diphenylborinic acid has a doublet at 7.69 ppm and multiplets from 7.45-7.48 ppm and a triplet at 7.40 ppm.[78]

Nam and Fukuzumi assigned the 7.75 ppm peak and the multiplet from 7.37-7.52 ppm as arising from triphenylborane,[39] but an authentic standard in CD_3CN did not produce the same peaks (Figure 4.7). Our triphenylborane sample has a multiplet from 7.20-7.26 ppm and a triplet of triplets at 7.15 ppm (Figures 4.8 and 4.9). Given that triphenylborane reacts rapidly with air, the previously reported peaks may be the product of this reaction, rather than triphenylborane itself. Therefore, ^{1}H NMR data likely indicate that another species is formed from the $NaBPh_4$, $HClO_4$ and O_2 reaction, which is likely the diphenylborinic acid.

Although not previously considered in the dioxygen activation study of **10** using $NaBPh_4$ as a reducing agent, tetraphenylborate has been reported to react under acidic conditions with dioxygen in a water-dichloromethane mixture to produce phenol and biphenyl.[79] While no mechanism for the formation of phenol and biphenyl was proposed for the reaction of tetraphenylborate with dioxygen under acidic conditions, previous studies indicated that under acidic conditions, a proton will attack the ipso position to form triphenylborane and benzene.[80] It has also been noted that tetraphenylborate can intramolecularly form biphenyl.[81] Given these data and our own control experiments, the possibility of a radical-based mechanism was explored.

The well-known radical scavenger 2,6-di-*tert*-butyl-4-methylphenol was employed for the $HClO_4$ reaction with BPh_4^-. The addition of 2,6-di-*tert*-butyl-4-methylphenol slowed down the reaction of $HClO_4$, $NaBPh_4$, O_2, and **10,** lowering the yield of **6** to 50% (Figure 4.10). While it is known that 2,6-di-*tert*-butyl-4-methylphenol reacts with **6**,[26] this reaction is slow compared to iron(IV)-oxo formation from $HClO_4$, $NaBPh_4$, and oxygen. With 50 equiv. of 2,6-di-*tert*-butyl-4-methylphenol, over 50% of **6** remains even after two hours in our control experiment, while the radical scavenger reaction occurs in less than 1000 seconds with only one equivalent of 2,6-di-*tert*-butyl-4-

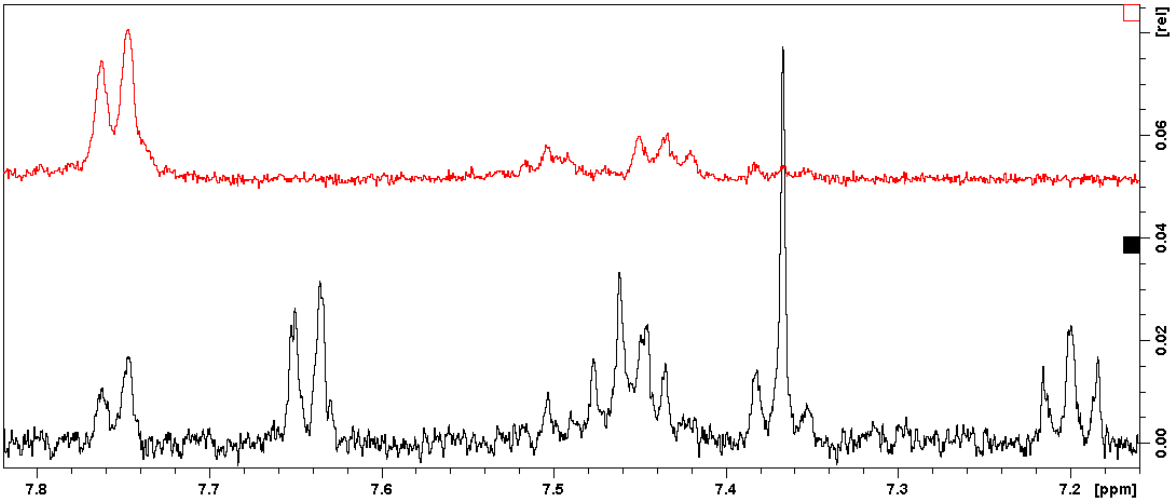

Figure 4.6: ^{1}H NMR spectrum of products from 1 mM $HClO_4$ and 1 mM $NaBPh_4$ in oxygen-saturated CD_3CN at 0 °C (black) and TOCSY spectrum using peak doublet at 7.75 ppm (red)

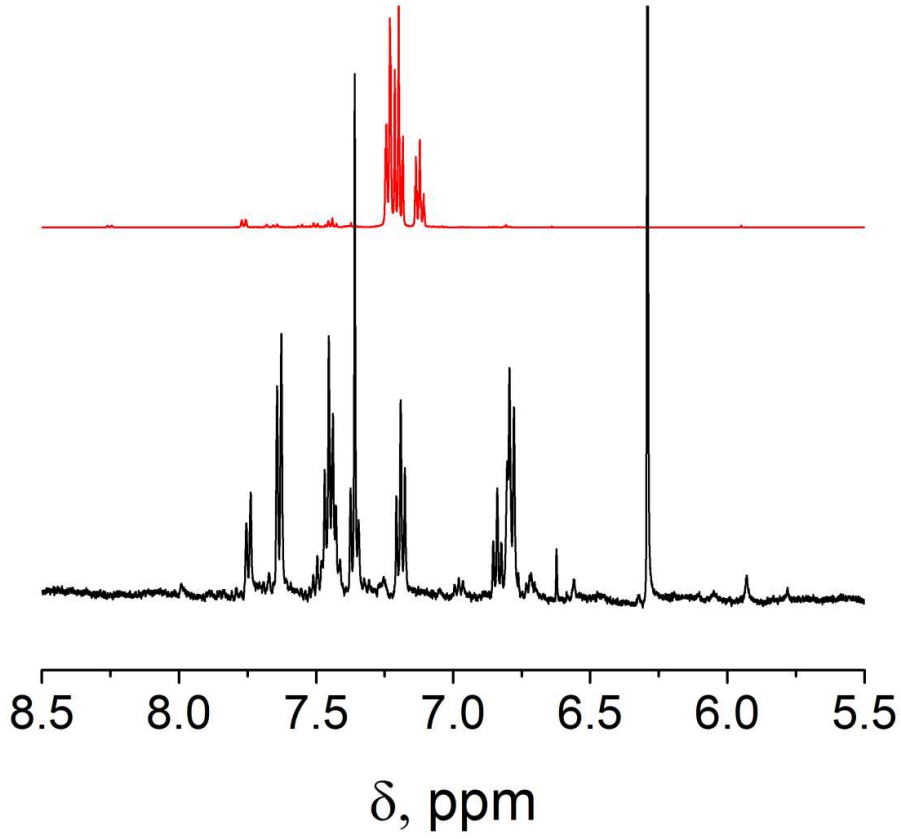

Figure 4.7: ^{1}H NMR spectrum of products from 1 mM $HClO_4$ and 1 mM $NaBPh_4$ in oxygen-saturated CH_3CN at 0 °C (black) compared with a spectrum of an authentic sample of triphenylborane in CD_3CN (red). Triphenylborane does not correspond to any of the peaks detected in the reaction of $HClO_4$, $NaBPh_4$, and oxygen.

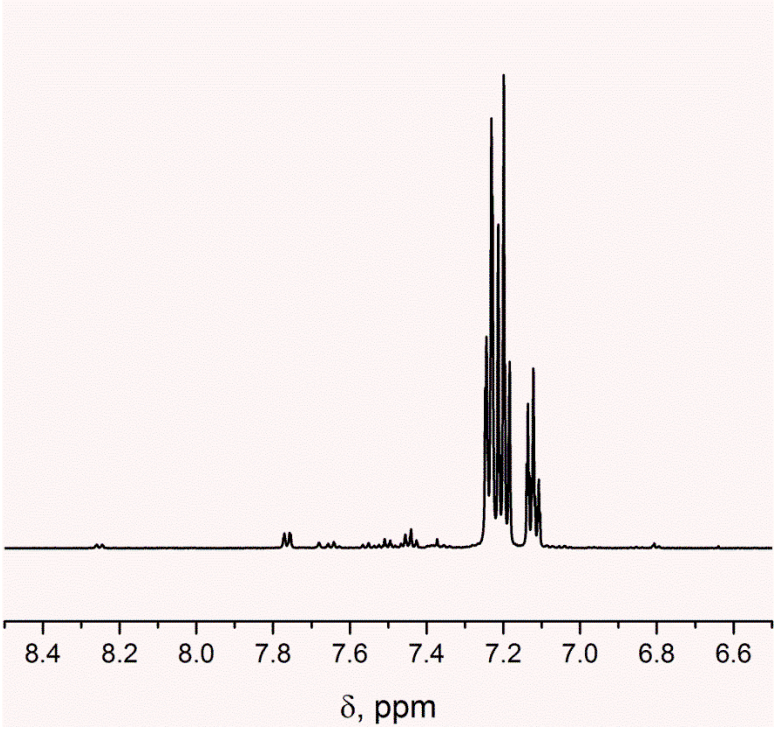

Figure 4.8: ^{1}H NMR spectrum of triphenylborane in CD_3CN.

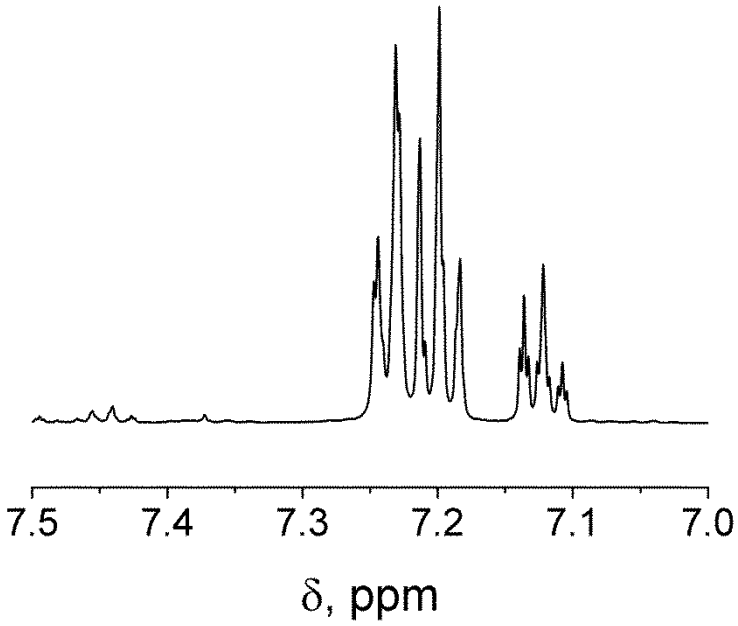

Figure 4.9: ^{1}H NMR spectrum of triphenylborane in CD_3CN, focusing on the peaks corresponding to triphenylborane.

Table 4.1: Products of reactions determined by GC analysis and ^{1}H NMR quantification

Conditions	Biphenyl Concentration (mM) GC/^{1}H NMR	Phenol Concentration (mM) GC/^{1}H NMR	BPh_2OH Concentration (mM) ^{1}H NMR	BPh_4^- Concentration (mM) ^{1}H NMR
10 + O_2 + BPh_4^- + $HClO_4$	0.6/0.6	0.6/0.8	0.4	0.2
O_2 + BPh_4^- + $HClO_4$	0.5/0.4	0.6/0.6	0.1	0
O_2 + BPh_4^-	0/0	0/0	0	1.1

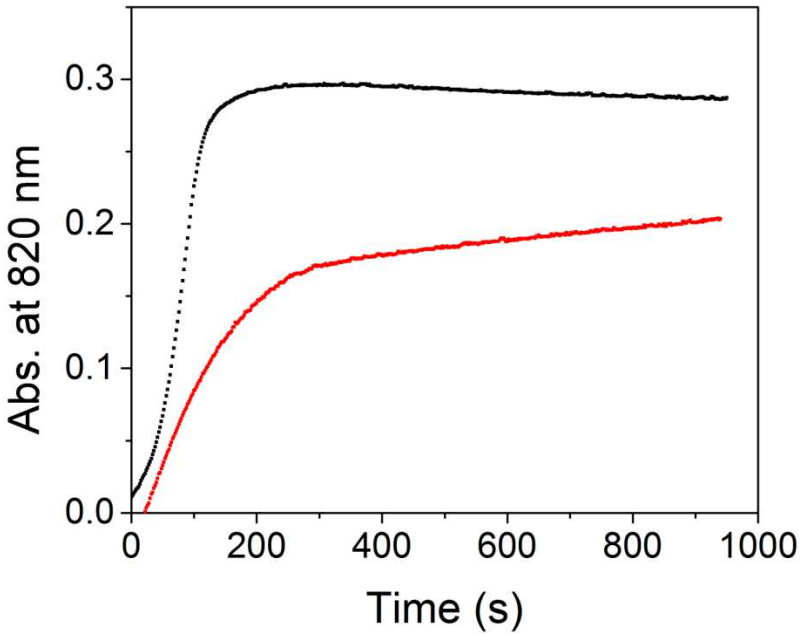

Figure 4.10: Time cource of 1 mM **10** in acetonitrile with 1 eq. $HClO_4$ and 1 eq. $NaBPh_4$ under saturated oxygen conditions at 0 °C without radical scavenger (black) and with 1 eq. 2,6-di-*tert*-butyl-4-methylphenol (red).

Scheme 4.4: Reaction of TEMPO under acidic conditions with peroxyl radicals.[82]

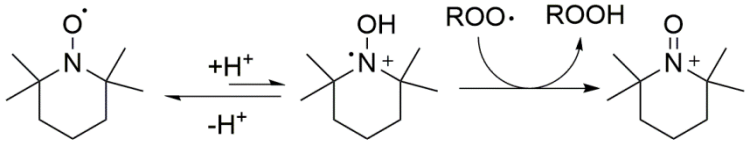

methylphenol. This indicates that the 1 equivalent of 2,6-di-*tert*-butyl-4-methylphenol reacts as a radical scavenger in the dioxygen activation reaction to reduce the yield of **6**.

TEMPO was used to further probe the type of reaction occurring. TEMPO has been shown to react readily with peroxyl radicals to form peroxides in the presence of acid.[82] Since these reactions are normally conducted under acidic conditions, addition of TEMPO seemed like a reasonable choice to see if peroxyl radicals were forming. Addition of 1 equiv. TEMPO to a solution with 1 equiv. $NaBPh_4$, 1 equiv. $HClO_4$ acid and 1 mM **10** slowed the reaction dramatically, compared to that without TEMPO, and lowered the yield of **6** to ~28 % (Figure 4.11). This lowered yield upon the addition of TEMPO suggests peroxyl radicals could be forming and reacting with the TEMPO to form peroxides, which still are reactive towards **10** and may be responsible for the **6** produced in the presence of TEMPO.

Both radical scavengers employed show a decrease in **6** yield, indicating that radicals are crucial to the formation of **6**, against what has been previously proposed.

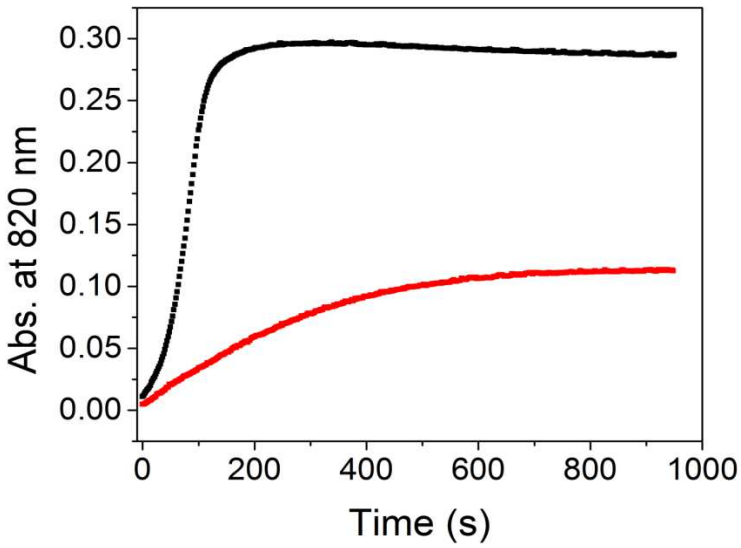

Figure 4.11: Time course for 1 mM of **10** under saturated oxygen conditions at 0 °C with 1 eq. $NaBPh_4$ and 1 eq. $HClO_4$ without (black) and with (red) 1 eq. TEMPO.

4.4 Conclusion

We have expanded the set of reactions involving nonheme iron complexes that are proposed to react through radical-based mechanisms in the presence of oxygen to form an iron(IV)-oxo complex. The reactions of **10** with cycloalkenes or $NaBPh_4$ and $HClO_4$ in the presence of dioxygen were already reported to form **6** through an HAT or PCET mechanism, respectively. The dependence on purity in the case of cycloalkenes and the fact that pseudo-first order reactivity is regained upon addition of impurities, which act as initiators, support the generation of peroxyl radicals from dioxygen. Radical traps used in both types of reaction decreased the yield of **6**, which implicate radical formation as a necessary part of both mechanisms. The product formation in the absence of iron in the cases involving BPh_4^- indicates that all reactions with BPh_4^- react through a similar radical-based pathway and that the iron(II) is merely a trap for this radical. These radical-based mechanisms, in the context of the work of Comba, Nam, and Fukuzumi,[39,73,74] indicate that formation of peroxyl radicals in the presence of dioxygen is a very common reaction that allows for synthetic iron(II) complexes to form iron(IV)-oxo species. This more generalized mechanism likely explains much of the reactivity of synthetic iron(II) complexes, and should be strongly considered whenever oxygen is present in a system.

Chapter 5

Resonance Raman Spectroscopic Characterization Metal-Peroxo, Oxo, and Iodosylaryl Species in Collaboration with Other Groups

Part of this work appeared in: de Sousa, D. P.; Bigelow, J. O.; Sundberg, J.; Que, L.; McKenzie, C. J. *Chem. Commun.* **2015**, *51*, 2802–2805.

5.1 Introduction

In order to understand the mechanisms of metalloenzymes, an important step is trapping and identifying intermediates species in the enzymatic cycle. One way of identifying intermediates is resonance Raman (rRaman) spectroscopy.[83] By exciting into an absorption band, resonance enhancement is achieved, thereby requiring less of the species under investigation as compared to Raman spectroscopy. This aids in characterizing both enzymatic and synthetic species at low concentration. Resonance Raman spectroscopy has been used to identify oxo and peroxo species, which are proposed to lie along metalloenzymatic pathways.[1,17] Intermediates can be compared to model complexes to help identify the trapped species. By comparing similar rRaman features, identification of fast decaying intermediates is made easier by longer lasting synthetic complexes, which can be characterized more fully by other techniques.

Besides allowing for comparison, characterization of synthetic model complexes also expands our knowledge of how electronics and sterics influence bond length and strength. In order to illuminate why certain metals are prevalent in nature, metals can be changed, a task more easily accomplished for synthetic complexes than enzymes. The comparison of these complexes allows for an understanding of what factors affect bonding.

Herein, the resonance Raman features of several synthetic complexes relevant to metalloenzymes are reported. These complexes utilize two ligand systems, PyMac = 2,7,12-trimethyl-3,7,11,17-tetra-azabicyclo[11.3.1]heptadeca-1(17),13,15-triene and tpena = N,N,N′-tris(2-pyridylmethyl)ethylenediamine-N′-acetato (Scheme 5.1). Different complexes are generated using these ligands, including oxo, peroxo, and iodosylarene species. The features of each of these species are compared with other, similar species from the literature, and highlight the changes that metals and ligand environment can have on different Raman vibrations.

Scheme 5.1: Main ligands used in this study.

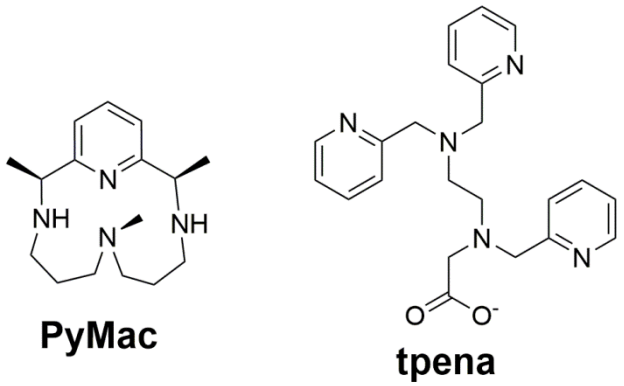

Scheme 5.2: Complexes using tpena ligand characterized by rRaman spectroscopy in this chapter.

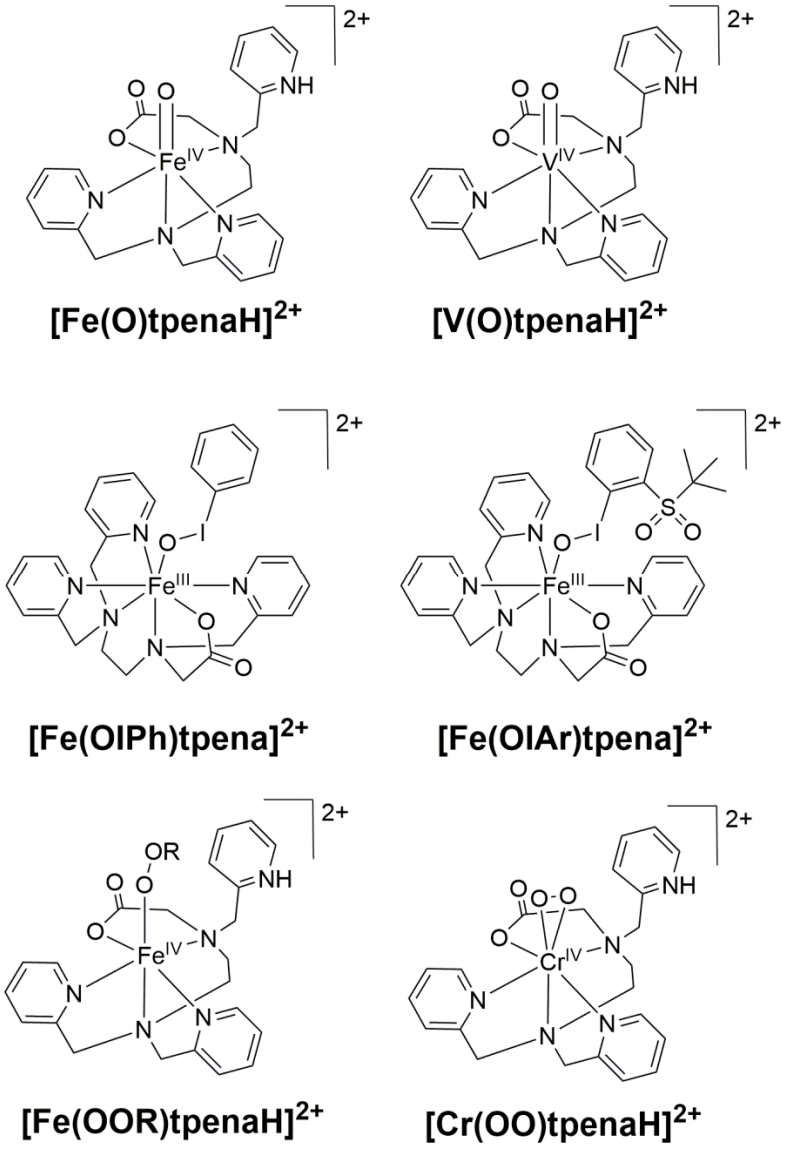

Scheme 5.3: Steps in the reactions from $[Fe^{II}(PyMac)]^{2+}$ and isopropyl 2-iodoxybenzoate. Reprinted with permission from Wanhua Ye; Douglas M. Ho; Simone Friedle; Taryn D. Palluccio; Elena V. Rybak-Akimova; *Inorg. Chem.* 2012, 51, 5006-5021. Copyright © 2012 American Chemical Society.

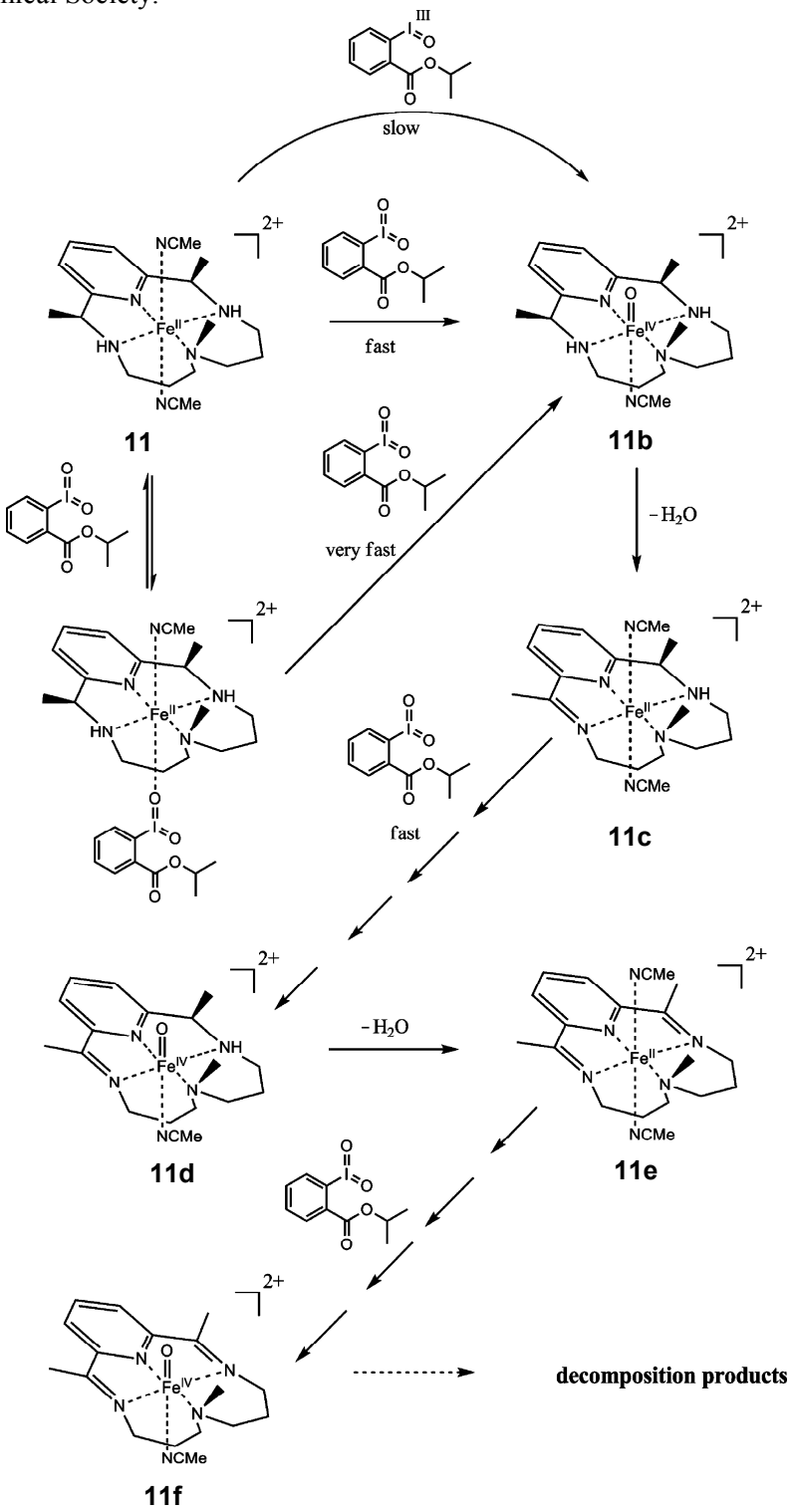

5.2 Experimental

5.2.1 General Methods

Resonance Raman spectra were collected using Spectra-Physics Model 2060 Kr^+ and 2030-15 Ar^+ lasers with an Acton AM-506M3 monochromator equipped with a Princeton LN/CCD data collection system. Spectra were obtained at 77 K and kept cold with liquid nitrogen in an EPR dewar. Raman frequencies were calibrated to indene prior to data collection. The monochromator slit width was set for a bandpass of 4 cm^{-1} for all spectra. Appropriate notch filters and, if necessary, pass filters were used. All solvents were used as received from Sigma-Aldrich unless otherwise noted. Synthesis of complexes were reported previously.[84–86] Iodosylbenzene, ^{18}O-labeled iodosylbenzene, and 2-(tert-butylsulfonyl)-iodosylbenzene were synthesized according to published procedures.[42,62,87,88]

5.2.2 Oxo Species

Tests for generation of $[Fe^{II}(PyMAC)]^{2+}$ derived oxo complexes: Complex **11b** was generated in 65 % yield with a 2 mM sample at -40 °C as reported previously.[84]

Since isopropyl 2-iodoxybenzoate was not very soluble in acetonitrile, only a 26 mM solution could be made where it completely dissolved. Therefore, 1 mL of 26 mM solution of isopropyl 2-iodoxybenzoate was added to 1 mL of a 20 mM solution of $[Fe^{II}(PyMAC)]^{2+}$ under argon. Unfortunately, two problems occurred: the λ_{max} was closer to 696 nm than 705 nm and the yield was low (40 %). A second attempt to generate **11b** with double the volume (2 mL) of 20 mM solution $[Fe^{II}(PyMAC)]^{2+}$ and 1.2 eq of isopropyl 2-iodoxybenzoate solution was tested. This still had low yield, until it was quickly warmed up in room temperature air and cooled again to -40 °C. The yield was then nearly quantitative, but again the λ_{max} was closer to 696 nm (the feature associated with **1d**) than 705 nm (the feature reported to be due to **11b**). However, the original authors indicated that a feature around 500 nm should be present if the complex was **11d**. Because this feature at 500 nm was not present, the spectra was assigned to **11b**.

Due to the success of warming the sample, the generation was tried at -20 °C, but the sample decayed rapidly; rather than form **11b**, it appears **11d** was formed. The molar equivalents of oxidant were increased by adding 100 μL of 3.6 M cooled solution of

$[Fe^{II}(PyMAC)]^{2+}$ to a 2 mL solution of 22 mM of isopropyl 2-iodoxybenzoate at -40 °C so that 18 mM $[Fe^{II}(PyMAC)]^{2+}$ could be achieved with 1.2 eq. of oxidant. However, the yield was even lower than before (12 %). Therefore, iodosylbenzene was used as an alternative oxidant by stirring with $[Fe^{II}(PyMAC)]^{2+}$ and then filtering off the excess, but this did not improve yield either.

Tests for the generation of $[Fe^{IV}(O)(tpenaH)]^{2+}$: Formation of $[Fe^{IV}(O)(tpenaH)]^{2+}$ in high enough concentration for rRaman proved to be a challenge. The starting complex had trouble dissolving in pure water; the most concentrated solution that completely dissolved was 4.2 mM with respect to the monomer. However, when a 1:1 mixture of acetonitrile/water was used, the complex turned from green to brown upon freezing. Upon warming, it returned to a green color, and then upon freezing it became brown again. Due to the color change, only pure water solutions were used in preparation of rRaman samples.

*Generation and rRaman conditions of **11b:*** To 2 mL of a 20 mM solution of **11** at -40 °C, 1 mL of a 26 mM acetonitrile solution of isopropyl 2-iodoxybenzoate was added (0.57 eq) under argon. This did not generate a high enough yield of **11b**, so a total of 1.2 eq. of isopropyl-2-iodoxybenzoate was added. The yield was still not high enough, so the solution was taken out of the cuvette and warmed up in the presence of air. The solution was returned to the cuvette and cooled to -40 °C for a UV-vis spectrum, which confirmed the species as **11b** (see Figure 5.1b). This sample was frozen on a cold finger and rRaman spectrum taken with rastering. An excitation wavelength of 406.7 nm at ~25 mW power was used. The spectrum resulted from 60 second exposures for 32 accumulations

*Generation and rRaman conditions of **11f***: A 1 mL of a 20 mM solution of **11** in acetonitrile was combined with 1 mL of a 26 mM solution of isopropyl 2-iodobenzoate in acetonitrile at -40 °C under argon. A portion of the solution was allowed to warm up to room temperature for approximately 30 minutes and turned a brick red color. To an argon filled schlenk cuvette, 1 mL of this brick red solution and 1 mL of 26 mM solution isopropyl 2-iodoxybenzoate were added (2.5 equivalents of isopropyl 2-iodoxybenzoate). This was stirred at room temperature, and then cooled to -40 °C for a UV-vis spectrum. This sample was frozen on a cold finger for rRaman with rastering. An excitation

wavelength of 406.7 nm at ~25 mW power was used. The spectrum resulted from 60 second exposure for 64 accumulations.

Generation and rRaman conditions of $[Fe(O)(tpenaH)]^{2+}$: A 4.9 mM solution of $[Fe^{III}(tpena)]^{2+}$ was generated by dissolving $[Fe^{III}_2(O)(tpenaH)_2]$ $(ClO_4)_4(H_2O)_2$ in water. To this solution, 11 eq. of cerium ammonium nitrate (CAN) was added and stirred at 25 °C. The sample was frozen on cold finger, evacuated and rastered during collection. An excitation wavelength of 406.7 nm was used ~20 mW power. The spectrum was collected with 30 second exposures, with 64 scans accumulated.

Generation and rRaman conditions of $[Fe^{IV}(O)(N4Py)]^{2+}$ sample: 0.5 mL of DI water was added to 0.0066 g of $[Fe(N4Py)](CH_3CN)(ClO4)_2$. To completely dissolve, 5.4 eq. CAN was added at 25 °C, resulting in an 18 mM solution of $[Fe^{IV}(O)(N4Py)]^{2+}$ by UV-vis spectroscopy. This was frozen on a cold finger and rastered during collection. An excitation wavelength of 406.7 nm at ~20 mW of power was used. The spectrum was collected with 60 second exposures for 16 accumulations.

Generation and rRaman conditions of $[Fe(O)(Bn\text{-}TPEN)]^{2+}$: 0.5 mL of DI water was added to 0.0035 g $[Fe(Bn\text{-}TPEN)](OTf)_2$. Approximately 6 eq. of CAN was added to the solution at 25 °C and stirred. The solution was frozen on a cold finger and rastered during collection. An excitation wavelength of 406.7 nm at ~20 mW power was used. The spectrum was collected with 15 second exposures for 256 accumulations.

Generation and rRaman conditions of $[V(O)(tpenaH)]^{2+}$ sample: 0.0079 g of $[V(O)(tpenaH)](ClO_4)_2$ was weighed out and stirred in 0.5 mL of DI H_2O. As not all the complex dissolved, the solution was filtered and then frozen on a cold finger. An excitation wavelength of 406.7 nm at ~30 mW power was used. The spectrum was collected with a scan rate of 1 second, with 1920 scans accumulated due to high fluorescence

5.2.3 Iodosylarene Species

Generation and rRaman conditions of $[Fe^{III}(tpena)]^{2+}$: the dimer $[Fe^{III}_2(O)(tpenaH)_2]^{4+}$ when dissolved in acetonitrile generates the major species, a low spin $[Fe^{III}(tpena)]^{2+}$ monomer.[85] Assuming all of the dimer converts to monomer, the concentration of the sample used was 9.5 mM. This was frozen in an EPR tube. This

sample was used for an excitation profile with ~30 mW at 406.7 nm, ~55 mW at 457.9 nm, ~60 mW at 488.0 nm, and ~ 80 mW 514.5 nm. These samples were collected at either 30 s or 60 s exposures with 32 accumulations

Generation and rRaman conditions of $[Fe^{III}(tpena)OIPh]^{2+}$: a sample of $[Fe^{III}_2(O)(tpenaH)_2]^{4+}$ was dissolved in CH_3CN (8.8 mM with respect to the monomer) and treated with an excess of solid iodosylbenzene, a bright orange color appears which corresponds to the complex $[Fe^{III}(tpena)OIPh]^{2+}$. This was frozen in an EPR tube. This sample was used for an excitation profile with ~30 mW at 406.7 nm, ~55 mW at 457.9 nm, ~60 mW at 488.0 nm, and ~ 80 mW 514.5 nm. A similar procedure was followed for ^{18}O-labeled iodosylbenzene. These samples were collected at either 30 s or 60 s exposures with 32 accumulations

For a higher concentration sample, the complex $[Fe^{III}(tpena)OIPh]^{2+}$ was generated with a 16 mM sample of $[Fe^{III}(tpena)]^{2+}$ dissolved in acetonitrile at 25 °C, to which excess iodosylbenzene was added. This sample was filtered, transferred to an EPR tube and frozen. A similar procedure was followed for ^{18}O-labeled iodosylbenzene. Excitation at 488 nm with ~40 mW power was used. Exposure of 60 seconds and 32 accumulations was used for both.

Generation and rRaman conditions for $[Fe^{III}(tpena)OIAr]^{2+}$: Using a 17 mM solution, 2-(tert-butylsulfonyl)-iodosylbenzene was added, following the procedure above. Excitation at 488 nm with ~40 mW power was used. Exposure of 15 seconds and 128 accumulations was used.

5.2.4 Peroxo Species

All Fe(OOR)tpena spectra were collected using a 568.2 nm laser line (50 mW) for 32 accumulations of 120 second exposures, except for the t-butylperoxo species, which was collected at the same wavelength, but at 65 mW power for 60 second exposures for 32 accumulations.

Generation of cumenyl peroxo species: a 6.5 mM solution of the $[Fe(tpena)]^{2+}$ was generated in CH_3CN. A 0.98 mL sample was cooled to -40 °C in a 0.5 cm cuvette, and 40 μL of a 37 mM stock solution of 80% cumene hydroperoxide diluted in CH_3CN

was added with stirring. Once the species was generated as determined by UV-vis absorption features, the sample was frozen in a NMR tube.

Generation of hydroperoxo species: a 10.4 mM solution of the $[Fe(tpena)]^{2+}$ was generated in CH_3CN. A 1 mL sample was cooled to -40 °C in a 0.5 cm cuvette, and 40 µL of a 40 mM stock solution of 30% hydrogen peroxide diluted in CH_3CN was added with stirring. Once the species was generated as determined by UV-vis absorption features, the sample was frozen in an EPR tube.

Generation of t-butylperoxo species: a 7.7 mM solution of the $[Fe(tpena)]^{2+}$ was generated in CH_3CN. A 2 mL sample was cooled to -40 °C in a 1 cm cuvette, and 100 µL of a 5-6 M stock solution of tert-butyl hydroperoxide was added with stirring. Once the species was generated as determined by UV-vis absorption features, the sample was frozen in an EPR tube.

Generation of the 9 mM samples for the chromium analysis were carried out as described in de Sousa *et al*.[89]

5.3 Results and Discussion

5.3.1 Iron(IV)-oxo Species

Iron(IV)-oxo species are important intermediates in nonheme iron enzymes.[1] They are proposed in several enzymatic cycles to be the reactive intermediate that abstracts a hydrogen atom from certain substrates. Developing an understanding of the factors that affect the rRaman frequencies of the iron(IV)-oxo species will help us understand their reactivity and allow for the classification of new intermediates.

The Que group has developed a number of techniques to obtain resonance Raman spectra of iron(IV)-oxo species.[57] A major problem with excitation into the ligand-to-metal charge transfer (LMCT) band of the iron(IV)-oxo species is that it also leads to their decay. This means that a slightly lower energy laser than the true LMCT band will be required so the sample does not photodecay as rapidly. However, changing the wavelength of excitation from that of the LMCT band decreases the resonance enhancement; therefore high concentrations of the iron(IV)-oxo complex must be used. This generally means that a frozen sample works better, although high concentration

solution samples have been shown to work.[60,90] The frozen sample must be rastered to avoid decay. Given these parameters, we chose to start with a 406.7 nm line with the frozen sample and raster to obtain good rRaman spectra of the iron(IV)-oxo complexes.

5.3.1.1 rRaman Studies Fe^{II}(PyMAC) Derived Species

A major way of determining Fe=O bond strength is rRaman spectroscopy. Stronger bonds generally have higher frequencies. Interestingly, $[Fe^{II}(PyMAC)]^{2+}$ has been shown to form three different iron(IV)-oxo species upon the addition of isopropyl 2-iodoxybenzoate (Scheme 5.3).[84] Previously, in the Rybak-Akimova group, low concentration samples of $[Fe^{II}(PyMAC)]^{2+}$ could generate complex **11b** (Scheme 5.3). This complex was stable at -40 °C for several hours and has a λ_{max} = 705 nm (ε = 240 M^{-1} cm^{-1}). However, the oxo moiety can attack the ligand, producing the decay product, **11c**, from species **11b**. The decay product **11c** can react further with isopropyl 2-iodoxybenzoate, producing **11d**, an oxoiron(IV) species with λ_{max} = 696 nm. The decay of **11d** is proposed to occur by the oxo moiety attacking the ligand again to form **11e**. The final product, **11f**, is obtained by adding even more of the oxidant. The three different oxo species, **11b**, **11d**, and **11f** provide a rare opportunity to compare Fe-O bond strength among similar complexes. The modification of the ligand should increase the electron donation from the ligand, and thus lower the Fe-O stretching frequency.

rRaman spectra were obtained for two of the species present in Scheme 5.3. One exhibited a UV-vis spectrum (Figure 5.1b) that was assigned to **11b**, although the spectrum was offset from 705 nm, which was reported previously.[84] The λ_{max} was closer to 696 nm than 705 nm, which was closer to the λ_{max} of **11d**. However, there was no feature around 500 nm identified, which is present for **11d.** This species was therefore assigned **11b** rather than **11d**. The rRaman spectrum for **11b** had a feature at 835 cm^{-1}, consistent with an iron(IV)-oxo stretch (Figure 5.1a).

While **11d** could not be characterized, a rRaman spectrum associated with **11f** was obtained. No absorbance maximum was assigned for **11f** previously, so this spectrum with a UV-vis feature at 665 nm was assigned to **11f** (Figure 5.2b).[84] The resonance Raman spectrum shows a feature at 831 cm^{-1} (Figure 5.2a), consistent with an iron(IV)-oxo stretch.

While complexes **11b**, **11d**, and **11f** cannot be generated in high yield,[84] and often form a mixture of products, the rRaman spectra of **11b** and **11f** show features in the range of iron(IV)-oxo species previously reported.[17] There is a minor shift from the peak at 835 cm^{-1} of **11b** to the peak at 831 cm^{-1} of **11f**. This is consistent with the ligand of **11f** being more electron-donating, but the shift is very small. This may be due to a mixture of iron(IV)-oxo species, which may broaden the features of the iron(IV)-oxo peaks. This may affect the wavenumber assignment of the peak. While there may be some impurity, the close values of the iron(IV)-oxo stretching frequencies indicates the ligand of **11f** is not different enough from **11b** to change the iron(IV)-oxo stretch significantly. Therefore, the electronic differences in these systems are not greatly influencing the rRaman stretching frequency for these iron(IV)-oxo species.

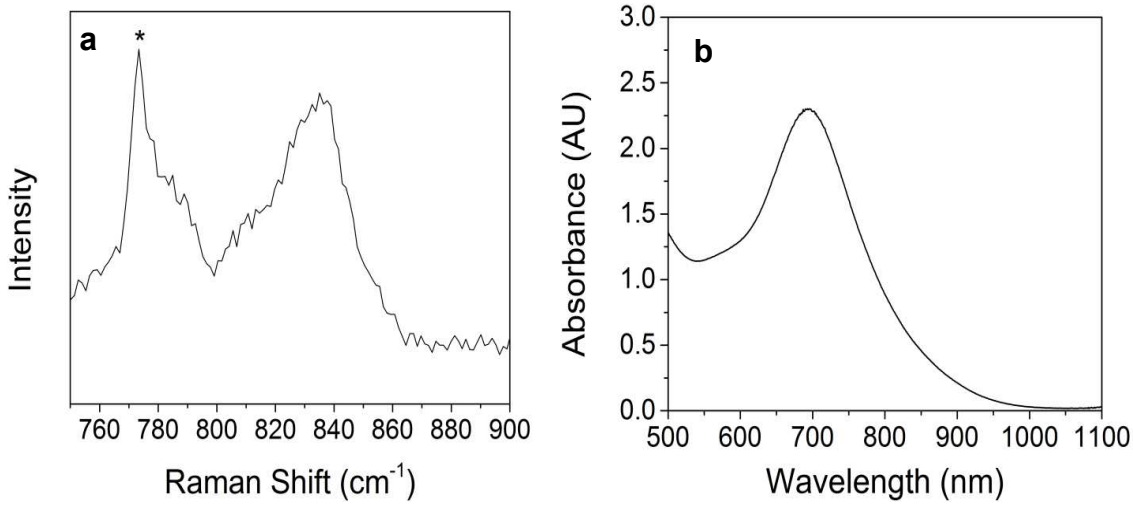

Figure 5.1: a) rRaman spectrum of sample associated with **11b**. Starred peak corresponds to acetonitrile. The broadness of the peak may indicate that more than one species is present. $\lambda_{excitation}$ = 406.7 nm. b) UV-vis data collected at -40 °C before freezing solution on a cold finger for resonance Raman spectroscopy. The high intensity indicates that ~10 mM of **11b** was produced.

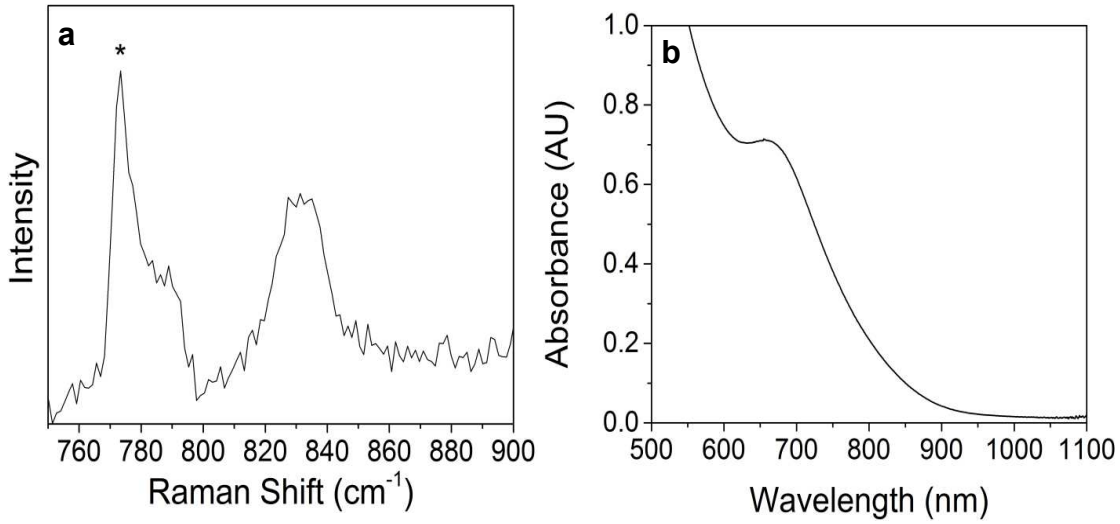

Figure 5.2: a) rRaman spectrum what was associated with **11f**. Starred peak corresponds to acetonitrile peak. $\lambda_{excitation}$ = 406.7 nm. b) UV-vis spectrum at -40 °C right before freezing to cold finger for resonance Raman spectroscopy. The λ_{max} is 665 nm.

5.3.1.2 Water Solutions of Iron(IV)-oxo Species

While many iron(IV)-oxo species have been characterized by rRaman spectroscopy, rRaman spectroscopy has not been used before on synthetic iron(IV)-oxo species with only water as the solvent.[17,90,91] Synthetic water-soluble iron(IV)-oxo species share the solvent in common with nonheme iron enzymes, making them of particular interest to generate and characterize. Vad *et al.* have demonstrated that $[Fe^{IV}(O)(tpenaH)]^{2+}$ can be generated in water by the addition of cerium ammonium nitrate (CAN).[85] This method of generating iron(IV)-oxo species in water led to the characterization of such species by rRaman spectroscopy.

Initial measurements of $[Fe^{IV}(O)(tpenaH)]^{2+}$ were complicated as the maximum solution concentration that could be generated was 5 mM, which only produced a rRaman spectrum with a very small iron(IV)-oxo peak. Other iron(IV)-oxo complexes were generated in water with the addition of CAN to test if an increase in concentration could be achieved. While the iron(II) complex had limited solubility in water, the addition of CAN generated the iron(IV)-oxo complex, which allowed for higher concentration of iron(IV)-oxo complex to dissolve as it formed in water. Concentrations of 18 mM for $[Fe^{IV}(O)(N4Py)]^{2+}$ and 7 mM for $[Fe^{IV}(O)(Bn\text{-}TPEN)]^{2+}$were generated in water in this manner (Scheme 5.4). However, the sample of $[Fe^{IV}(O)(tpenaH)]^{2+}$ showed increased fluorescence with an increase in concentration, so the 5 mM solution sample was used.

Of the iron(IV)-oxo species generated in water by the addition of CAN, $[Fe^{IV}(O)(N4Py)]^{2+}$, $[Fe^{IV}(O)(Bn\text{-}TPEN)]^{2+}$, and $[Fe^{IV}(O)(tpenaH)]^{2+}$ all produced peaks that were in the range of an Fe-O stretch. Both $[Fe^{IV}(O)(N4Py)]^{2+}$ and $[Fe^{IV}(O)(Bn\text{-}TPEN)]^{2+}$ had Fe-O frequencies that could be compared to those obtained in non-aqueous solutions. The 842 cm^{-1} peak for $[Fe^{IV}(O)(N4Py)]^{2+}$ (Figure 5.5) was within error of 841 cm^{-1}, which had been reported previously in acetonitrile, and the peak at 837 cm^{-1} for $[Fe^{IV}(O)(Bn\text{-}TPEN)]^{2+}$ (Figure 5.6) was also within error of the peak at 835 cm^{-1} previously reported in acetonitrile.[28] As the frequencies are not significantly different, the species being in generated in water by CAN is the same as the one generated in acetonitrile. This established that CAN addition is a new way of generating iron(IV)-oxo species in water in high concentration for the study by rRaman spectroscopy.

The spectrum of $[Fe^{IV}(O)(tpenaH)]^{2+}$showed a peak at 833 cm^{-1} (Figure 5.3), which could be an Fe-O stretch. However, due to a solution of pure water being necessary for generation, no isotope labeling experiment was tried. Instead, a vanadium-oxo complex was generated with the tpena ligand system to compare the V-O stretch with the Fe-O stretch, as an inexpensive version of an isotope-labeling test, but comparison was challenging due to fluorescence, which created a noisy baseline (Figure 5.4).

In summary, the generation of iron(IV)-oxo species in high concentration with the addition of the oxidant CAN has been proven to be an effective method of producing aqueous iron(IV)-oxo species for detection by rRaman spectroscopy. The excess of CAN needed does not seem to necessarily protonate the species, as two complexes with reported iron(IV)-oxo stretches showed no significant change in frequencies from a sample generated in acetonitrile using iodosylbenzene as the oxidant. Interestingly, a new iron(IV)-oxo species was characterized, $[Fe^{IV}(O)(tpenaH)]^{2+}$, which has a frequency that falls within the range Fe-O stretches reported previously. As $Fe^{IV}(O)(tpenaH)]^{2+}$ has only been generated in water, we were able to show that it could be compared with other iron(IV)-oxo complexes that showed the same frequencies generated in water or acetonitrile.

Scheme 5.4: Other iron complexes generated using CAN in water and characterized by rRaman spectroscopy.

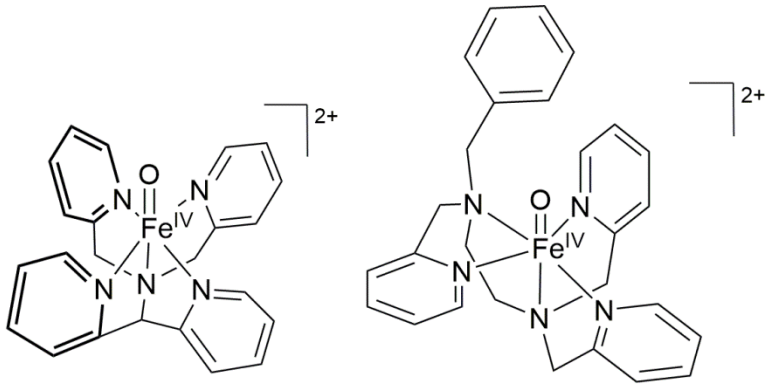

[Fe(O)(N4Py)]$^{2+}$ **[Fe(O)(Bn-TPEN)]$^{2+}$**

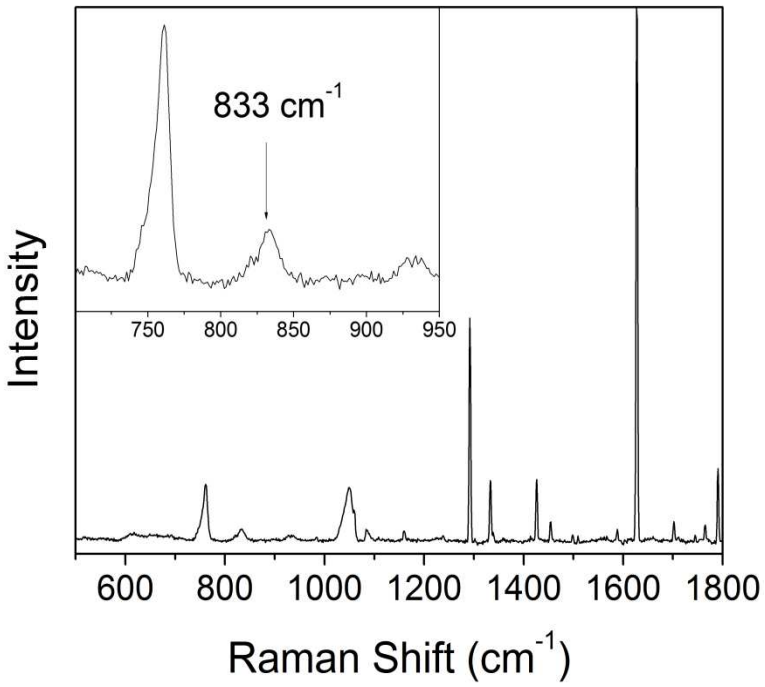

Figure 5.3: rRaman spectrum of $[Fe^{IV}(O)(tpenaH)]^{2+}$ generated in water with CAN collected with 406.7 nm excitation; inset shows the region that has a peak that could correspond to an Fe-O stretch.

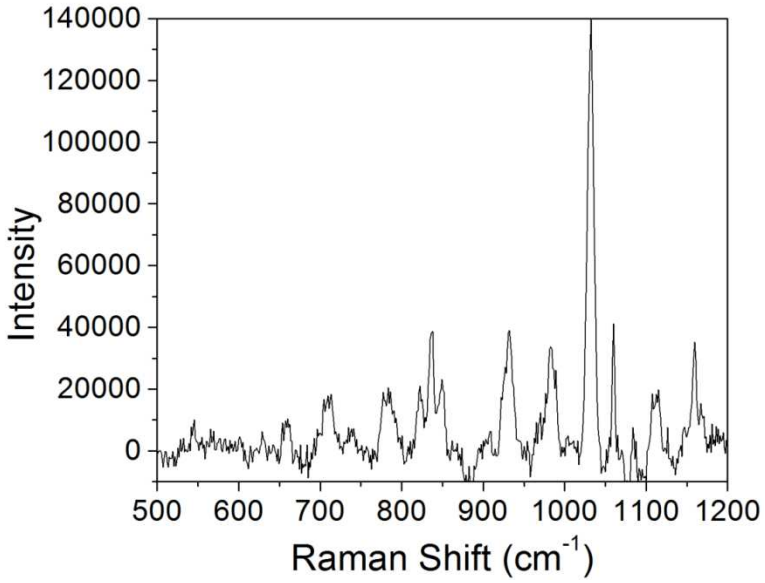

Figure 5.4: Noisy spectrum of $[V(O)(tpenaH)]^{2+}$ in water collected in a similar manner to $[Fe^{IV}(O)(tpenaH)]^{2+}$. The oxo related peak may be shifted from the iron complex, but due to the noise, no conclusive assignment was made. $\lambda_{excitation}$ = 406.7 nm.

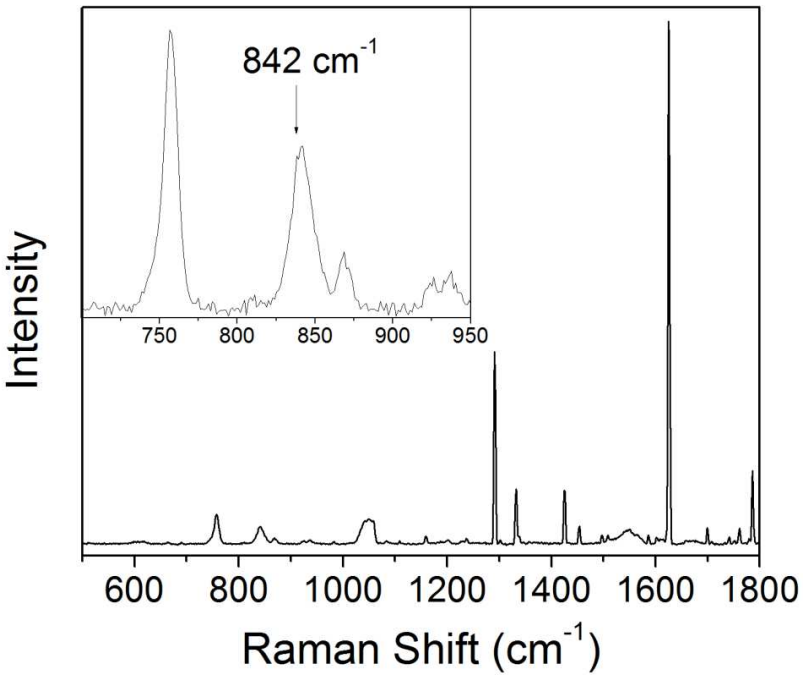

Figure 5.5: : rRaman spectrum of $[Fe^{IV}(O)(N4Py)]^{2+}$ generated in water with CAN collected with 406.7 nm excitation; inset shows the region that has a peak that corresponds to an Fe-O stretch.

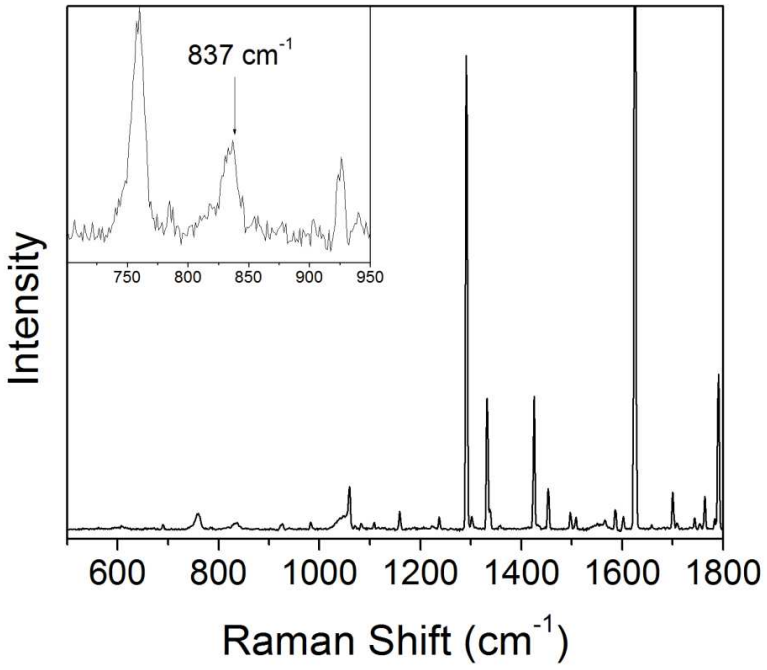

Figure 5.6: : rRaman spectrum of $[Fe^{IV}(O)(Bn\text{-}TPEN)]^{2+}$ generated in water with CAN collected with 406.7 nm excitation; inset shows the region that has a peak that corresponds to an Fe-O stretch.

5.3.2 Iodosylarene-iron(III) Complexes

Iodosylbenzene and similar species are often used as oxidants in the generation of metal-oxo species.[17] However, some species instead react with iodosylarenes to form iodosylarene-metal complexes.[86,92] An iodosylarene-iron(III) species was proposed in recent work to be an precursor to an unstable iron(V)-oxo species.[86] Understanding this species may illuminate the factors necessary for the generation of a new iron(V)-oxo species.

The dimer $[Fe^{III}_2(O)(tpenaH)_2]^{4+}$ when dissolved in acetonitrile generates the major species, a low spin $[Fe^{III}(tpena)]^{2+}$. When this is treated with an excess of solid iodosylbenzene, the solution turns a bright orange color which corresponds to the complex $[Fe^{III}(tpena)OIPh]^{2+}$. The Raman spectra of $[Fe^{III}(tpena)]^{2+}$ and $[Fe^{III}(tpena)OIPh]^{2+}$ were conducted to investigate their stretching frequencies.

Excitation profiles of both complexes were collected, as both were new species and no other method of characterization had been established. $[Fe^{III}(tpena)]^{2+}$ has a feature with a $\lambda_{max} \approx 380$ nm, while $[Fe^{III}(tpena)OIPh]^{2+}$ has a broad shoulder at ~450 nm. Based on internal comparison of major peaks (815 cm^{-1} and 1286 cm^{-1}) in the spectra of $[Fe^{III}(tpena)]^{2+}$ to the main solvent peak at 922 cm^{-1} allowed for a general trend to be established of decreasing intensity associated with the features from the complex with decreasing energy of the line (Figure 5.7). It should be noted, however, that the 406.7 nm and 457.9 nm lines produced very noisy spectra, and the 514.5 nm line spectra did not contain the 1286 cm^{-1} peak due to the smaller spectral window. However, the basic trend of the excitation profile conducted indicates that 815 cm^{-1} is resonance enhanced and that the 406.7 nm line is closest to what appears to be a LMCT or π-to-π^* transition. Changes in the collection could allow for better spectra with the 406.7 nm and 457.9 nm, so a better peak comparison con be used for a more quantitative analysis.

The $[Fe^{III}(tpena)OIPh]^{2+}$ complex unfortunately blackens upon irradiation with the 406.7 nm line, indicating some kind of photodecay. However, given that many complexes bleach instead of becoming darker upon irradiation with the 406.7 nm line, this indicates that the 406.7 nm laser may aid in unmasking the Fe^{V}=O species proposed

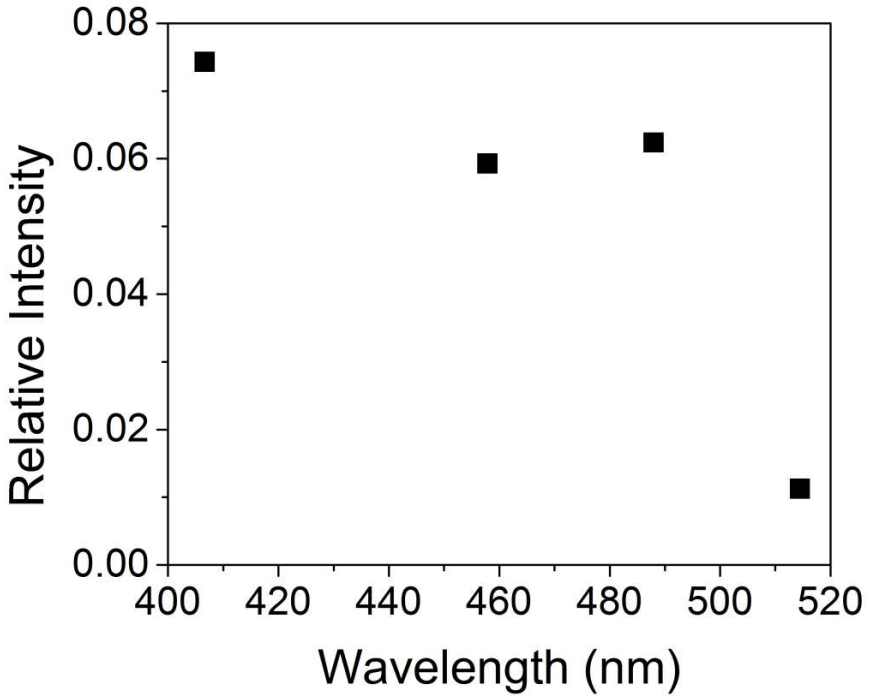

Figure 5.7: Excitation profile of $[Fe^{III}(tpena)]^{2+}$ comparing the intensity of the peak at 815 cm^{-1} to the solvent peak at 922 cm^{-1}.

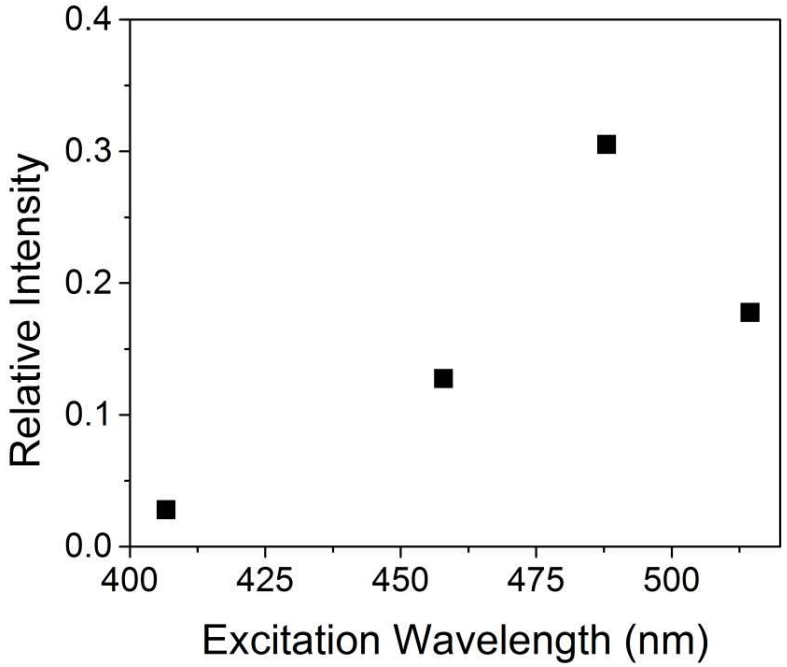

Figure 5.8: Resonance Raman excitation profile of $[Fe^{III}(tpena)OIPh]^{2+}$ following the 665 cm^{-1} peak seen in all spectra.

as the reactive intermediate in the catalysis of the oxidation of thioanisole in the presence of excess iodosylbenzene.

Even though decay occurs in with the 406.7 nm line, it is still included in an excitation profile of the 665 cm^{-1} peak from the iodosylbenzene complex (Figure 5.8). This was the only peak to be seen clearly in all the spectra collected and does not have a corresponding peak in the $[Fe^{III}(tpena)]^{2+}$ spectra. It seems that the 488.0 nm line is where the greatest resonance enhancement occurs, which is not surprising given the increased absorbance in this area from $[Fe^{III}(tpena)]^{2+}$ to $[Fe^{III}(tpena)OIPh]^{2+}$.

The resonance enhancement of the 488.0 nm spectrum allowed for many peaks attributed to $[Fe^{III}(tpena)OIPh]^{2+}$ to be clearly observed (Figure 5.9). This allowed for the possibility of ^{18}O labeling experiments to be worthwhile. Comparison of the labeled and unlabeled spectra (Figure 5.9) did not show any isotope-induced shifts. The fault does not lie in the ^{18}O-labeled iodosylbenzene, as the same ^{18}O-labeled iodosylbenzene was used later for successful labeling of an unrelated species. The lack of peak shifting indicates that the vibrations of $[Fe^{III}(tpena)OIPh]^{2+}$ may not be affected by labeling, which could be due to a linear bond or exchange with water present in the solution which may have decreased the labeling of the complex. Coupling may also result in the Fe-O stretch and the I-O stretch moving together, making isotope labeling inconsequential. It is also possible these vibrations are not due to I-O or Fe-O bonds.

To aid in the determination of the origins of the vibrations in the rRaman of $[Fe^{III}(tpena)OIPh]^{2+}$, $[Fe^{III}(tpena)]^{2+}$ was reacted with 2-(tert-butylsulfonyl)-iodosylbenzene to form the analogous species $[Fe^{III}(tpena)OIAr]^{2+}$. The rRaman of this new complex is shown in Figure 5.10. Peaks shifted compared to the iodosylbenzene complex, from 434 cm^{-1} to 448 cm^{-1} and from 668 cm^{-1} to 679 cm^{-1}. Since the peaks both shift upwards with use of 2-(tert-butylsulfonyl)-iodosylbenzene, it seems unlikely that one of the vibrations represents the Fe-O bond and the other the I-O bond. If they were, the bond strength of one should increase while the other decreases. The lower frequency could be the I-O bond, as 431 cm^{-1} and 488 cm^{-1} have been reported as the I-O stretching for iodosylbenzene[93] – in fact, there is a 488 cm^{-1} peak in both spectra.

The resonance Raman spectra of a related complex $[Fe(OCl)(MeN4Py)]^{2+}$ have been reported, where MeN4Py = 1,1-di(pyridin-2-yl)-N,N-bis(pyridin-2-ylmethyl)ethanamine.[94] Three major frequencies are assigned: Fe-O stretch at 653 cm^{-1}, O-Cl at 580 cm^{-1}, and a symmetric Fe-O-Cl bend at 673 cm^{-1}. The symmetric bending mode is not perturbed by ^{18}O-labeling, but slightly be the replacement of the chloride with a bromide. The small shifting frequency upon a larger atom being used is analogous to the replacement of iodosylbenzene with 2-(tert-butylsulfonyl)-iodosylbenzene for the formation of iodosylarene complexes from $[Fe^{III}(tpena)]^{2+}$. While no peaks shift upon ^{18}O-labeling of $[Fe^{III}(tpena)OIPh]^{2+}$, two peaks shift upon changing the iodosylarene. The peak at 668 cm^{-1} for $[Fe^{III}(tpena)OIPh]^{2+}$ and at 679 cm^{-1} for $[Fe^{III}(tpena)OIAr]^{2+}$ is very similar to the Fe-O-Cl bend of $[Fe(OCl)(MeN4Py)]^{2+}$ at 673 cm^{-1}. It may be that these peaks in $[Fe^{III}(tpena)OIPh]^{2+}$ and $[Fe^{III}(tpena)OIAr]^{2+}$ represent an Fe-O-I bending mode. This assignment could explain the lack of sensitivity to ^{18}O-labeling for $[Fe^{III}(tpena)OIPh]^{2+}$: the peaks are not isolated stretches, e.g. Fe-O and I-O, but rather bending modes or combined stretching frequencies.

Very few other nonheme iodosylarene-iron(III) species have been characterized by resonance Raman. Two nonheme examples was characterized by the Nam group,[92] yet there are startling differences between these complexes and the iodosylarene-iron(III) complexes reported herein. First, the λ_{max} = 660 nm for the Nam complees, while no such feature exists for $[Fe^{III}(tpena)OIPh]^{2+}$. Instead, there is a feature around 450 nm. The two types of complexes are also different in the rRaman features. For the window shown for the Nam group complexes, only small peaks at 772 cm^{-1} for $[Fe^{III}(13\text{-}TMC)(OIArF_5)]^{3+}$ and 783 cm^{-1} for $[Fe^{III}(13\text{-}TMC)(OIPh)]^{3+}$ were seen. These areas are unfortunately often obscured by notch filter bleed in our samples, so small peaks may go undetected. However, even in spectra where there is less notch filter bleed, we do not see peaks in that region. While these four complexes are all iodosylarene-iron(III) species, there obviously is some difference due to the peaks in both the electronic spectra and the rRaman spectra. This may be due to ligand effects. The negatively charged tpena ligand forms a seven-coordinate iodosylbenzene complex based on the crystal structure, while the neutral 13-TMC may only provide a five-coordinate compound. This can alter both

the bond strength and angle of the iodosylarene, and may contribute to the differences seen.

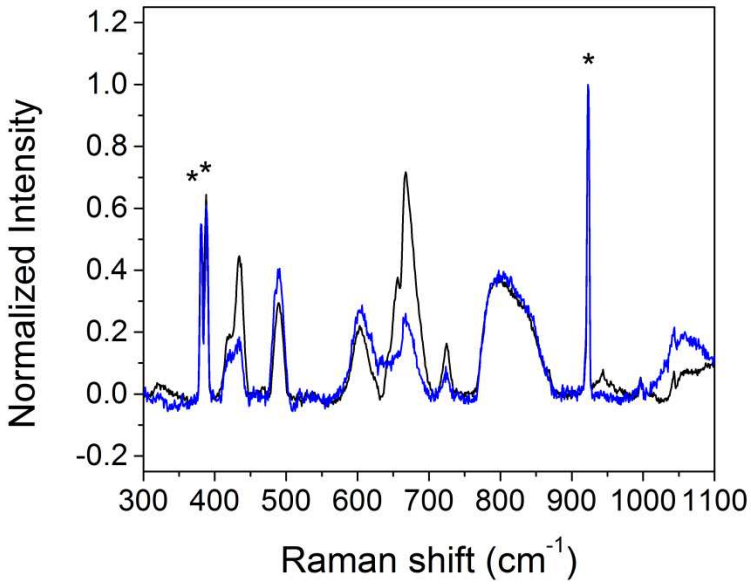

Figure 5.9: Comparison of rRaman spectra of ^{18}O-labeled (blue) and unlabeled (black) $[Fe^{III}(tpena)OIPh]^{2+}$ upon 488.0nm excitation. The spectra are very similar, indicating either exchange with water, a linear bond, or that these vibrations do not involve oxygen. The peak at around 800 cm^{-1} seems likely to be notch filter bleed.

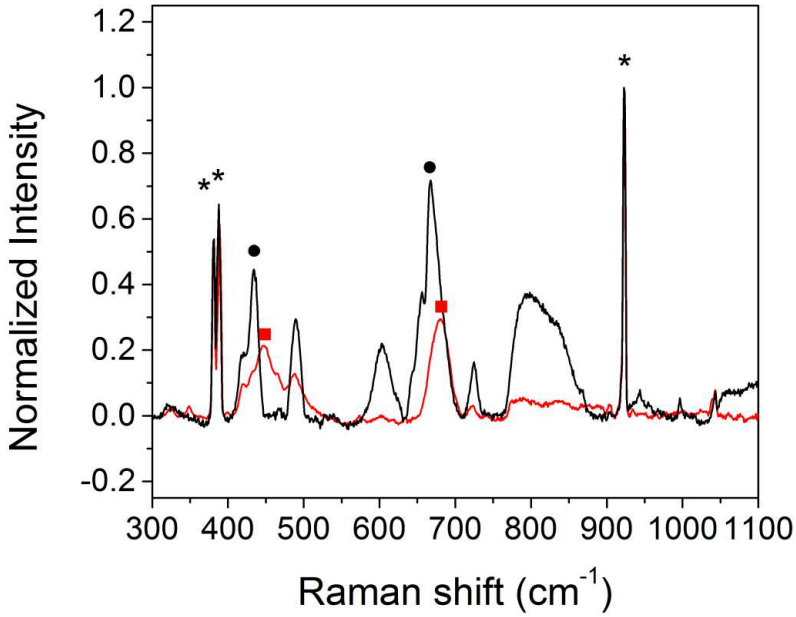

Figure 5.10: A comparison the rRaman spectra of $[Fe^{III}(tpena)OIPh]^{2+}$ (black) and $[Fe^{III}(tpena)OIAr]^{2+}$ (red) collected with a 488.0 nm excitation. The peaks of $[Fe^{III}(tpena)OIPh]^{2+}$ labeled by the black circles shift to the peaks of $[Fe^{III}(tpena)OIAr]^{2+}$ labeled by the red squares: 434 cm^{-1} to 448 cm^{-1} and from 668 cm^{-1} to 679 cm^{-1}. The 488 cm^{-1} peak does not move and 603 cm^{-1} decreases in intensity.

5.3.3 Peroxo Complexes

5.3.3.1 Iron(III)-peroxo Species

Peroxo species are implicated as intermediates in many different metalloenzymes, most importantly nonheme iron enzymes.[1] Building a library of such compound allows for comparison between synthetic and new enzymatic intermediates that can only be trapped and characterized by rRaman spectroscopy.

Upon addition of hydrogen peroxide, cumene hydroperoxide, t-butyl hydroperoxide to $[Fe^{III}(tpena)]^{2+}$ in CH_3CN, intense purple features appeared, typical of iron(III)-peroxo species. The rRaman spectra of these complexes indicate that these are end-on low-spin iron(III)-peroxo species.

The t-butylperoxo species had a frequency at 682 cm^{-1}, which we assign to the Fe-O stretch, and a frequency and at 790 cm^{-1} that we assign to O-O stretch (Figure 5.11). These signals are consistent with what has been reported previously for end-on low-spin iron(III)-t-butylperoxo species, where Fe-O stretches from 685 cm^{-1} to 696 cm^{-1} and O-O stretches between 790 cm^{-1} and 796 cm^{-1} have been reported.[95–97] A previously reported end-on low-spin iron(III)-t-butylperoxo species using the tris(2-pyridylmethyl)amine (TPA) ligand was reported to have an Fe-O stretch at 696 cm^{-1} and an O-O stretch at 796 cm^{-1},[95] while an iron(III) t-butylperoxo species with a modified version of the ligand, 6-Me_3TPA, was high-spin and had an Fe-O stretch at 648 cm^{-1} and a Fermi doublet at 844 and 880 cm^{-1}.[98] The shift to a much higher O-O stretch and a lower Fe-O stretch indicates the transition from a low spin complex to a high spin complex. However, our complex was not at such high or low values, as is consistent for a low-spin iron(III)-peroxo species.

The hydroperoxo species exhibited two features, one at 615 cm^{-1} that was assigned to an Fe-O stretch and another at 789 cm^{-1} that was assigned to an O-O stretch (Figure 5.12). These values fall within the range of end-on low-spin iron(III)-hydroperoxo species, which have Fe-O stretches from 609 cm^{-1} to 632 cm^{-1} and O-O stretches from 790 cm^{-1} to 811 cm^{-1}.[1] For comparison, a much higher O-O stretch (830-891 cm^{-1}) is reported for high-spin iron(III)-peroxo species.[31,99–102]

Interestingly, the cumenylperoxo iron(III) species showed a higher Fe-O stretch than had been previously reported for low-spin iron(III)-cumenylperoxo species. While the cumeneperoxo iron(III) species had a frequency at 685 cm^{-1} assigned to the Fe-O stretch (Figure 5.13), previously reported low-spin cumenylperoxo-iron(III) species have Fe-O stretches that occur at 615 cm^{-1} to 631 cm^{-1}.[103,104] While the Fe-O stretch is higher than expected, the possible O-O stretches of 770 cm^{-1} and 786 cm^{-1} is close to the range of previously reported species: 795-799 cm^{-1}.[103,104] Likely, the difference in Fe-O frequencies between this work and what is reported previously results from a sulfur ligand bound axially in all previous cases. Without such an electron-donating species, the Fe-O bond would likely be stronger.

The iron(III)-peroxo species shows similar results as what has been reported previously, but add to the collection with an example of carboxylate ligation often found for the active sites of nonheme iron enzymes. This ligation change did not bring about a high-spin complex, and it does not seem the free pyridyl arm interacted with the peroxo portion in any significant way.

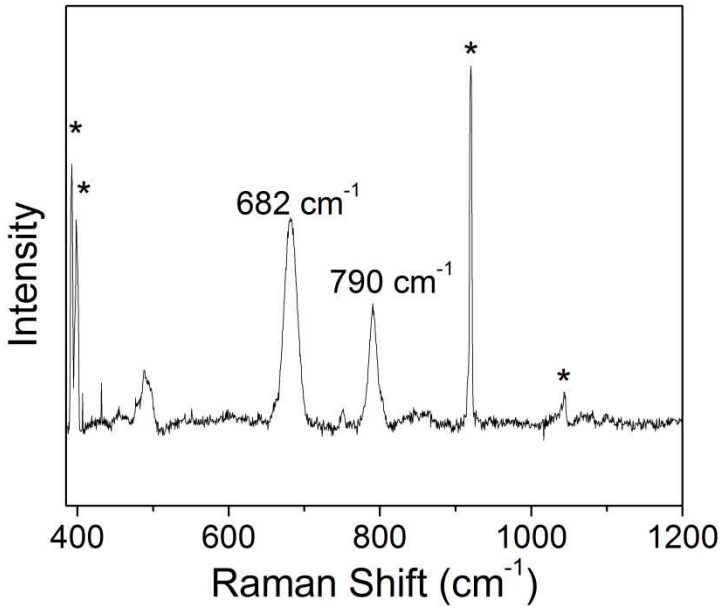

Figure 5.11: Resonance Raman spectrum of $[Fe^{III}(OOtBu)(tpenaH)]^{2+}$ shows distinct peaks at 682 cm^{-1}, corresponding to an Fe-O stretch, and 790 cm^{-1}, corresponding to an O-O stretch. These are indicative of a low-spin iron(III)-peroxo species. Solvent peaks marked with asterisks. $\lambda_{excitation}$ = 568.2 nm.

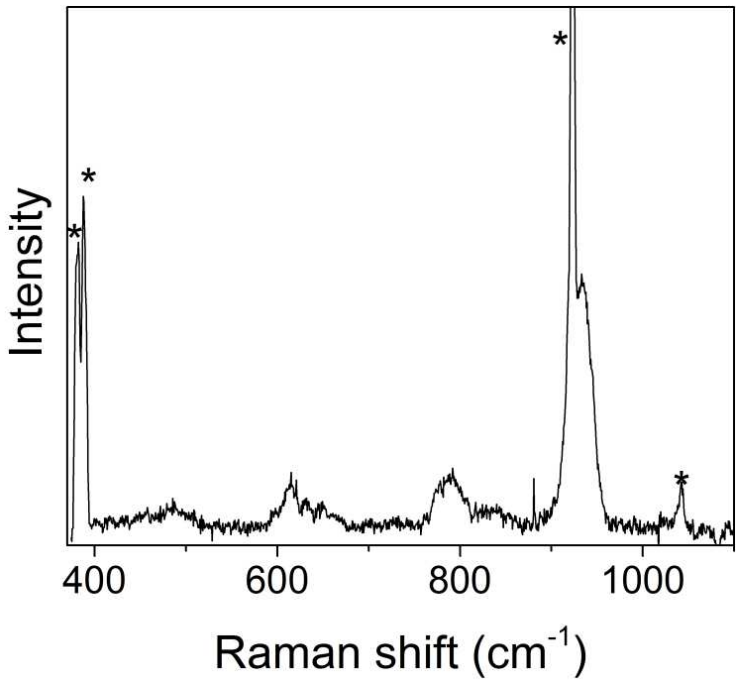

Figure 5.12: Resonance Raman spectrum of $[Fe^{III}(OOH)(tpenaH)]^{2+}$ shows peaks at 615 cm^{-1}, corresponding to an Fe-O stretch, and 789 cm^{-1}, corresponding to an O-O stretch. These are indicative of a low-spin iron(III)-peroxo species. Solvent peaks marked with asterisks. $\lambda_{excitation}$ = 568.2 nm.

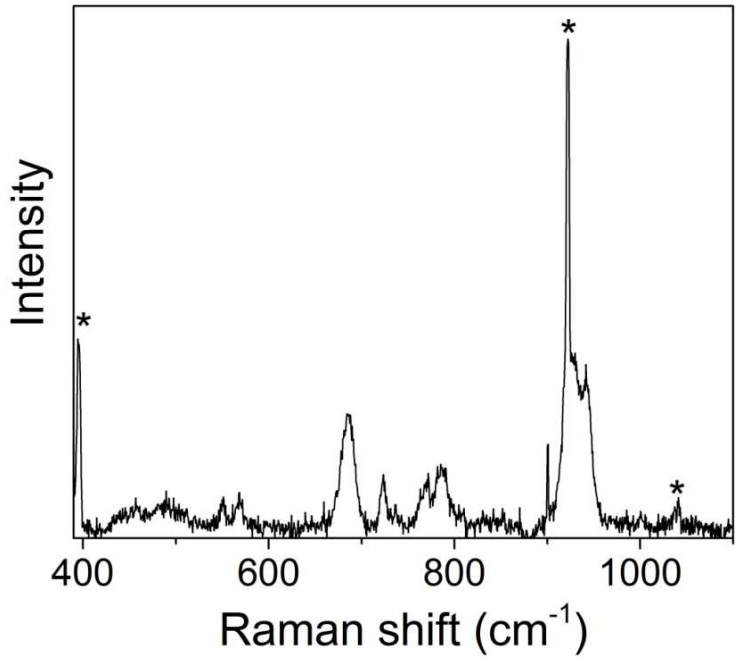

Figure 5.13: Resonance Raman spectrum of $[Fe^{III}(OOCm)(tpenaH)]^{2+}$ shows peaks at 685 cm^{-1}, corresponding to an Fe-O stretch, and a doublet at 770 cm^{-1} and at 786 cm^{-1}, corresponding to an O-O stretch. These are indicative of a low-spin iron(III)-peroxo species. Solvent peaks marked with asterisks. $\lambda_{excitation}$ = 568.2 nm.

Table 5.1: rRaman stretching frequencies of Fe(OOt-butyl) species

Species	Fe-O stretch (cm^{-1})	O-O stretch (cm^{-1})	Spin	Ref.
Fe(TPA)	696	796	LS	[95]
Fe(L)	694	790	LS	[96]
Fe(β-BPMCN)	685	793	LS	[97]
Fe(6-Me_3TPA)	648	880/844	HS	[98]

Table 5.2: rRaman stretching frequencies of Fe(OOH) species

Species	Fe-O stretch (cm^{-1})	O-O stretch (cm^{-1})	Spin	Ref.
Fe(N4Py)	632	790	LS	[105,106]
Fe(Py5)	627	806	LS	[105]
Fe(H-TPEN)	625	801	LS	[107]
Fe(Me-TPEN)	617	796	LS	[107]
Fe(Pc-TPEN)	617	796	LS	[107]
Fe(pb)2	623	811	LS	[108]
Fe(TPA)	626	789	LS	[106]
Fe(Me-TPPN)	609	799	LS	[109]
Fe(TMC)	676	870	HS	[31]
Fe(H_2bbpa)	621	830	HS	[100]
Oxyhemerythrin	503	844	HS	[101]
E11A-SOR	567	838	HS	[102]
Fe(cyclam-PrS)	419	891	HS	[99]

Table 5.3: rRaman stretching frequencies of Fe(OO-cumenyl) species

Species	Fe-O stretch (cm^{-1})	O-O stretch (cm^{-1})	Spin	Ref.
Fe([15]aneN4)(SAr)	615	795	LS	[103]
Fe([15]aneN4)(SAr)	623	799	LS	[104]
Fe([15]aneN4)(SArF_4SArF_5)	631	797	LS	[104]
Fe([15]aneN4)(SArNO_2)	625	798	LS	[104]

5.3.3.2 Side-on Peroxo Chromium Complex

While chromium is not usually a metal utilized by biology, it still can form oxo and peroxo species.[89,110–116] These species are interesting to compare with more common metals utilized in biology to learn what makes certain abundant metals more common for enzymes.

A side-on chromium-peroxo species could be generated using the same tpena ligand. Addition of excess hydrogen peroxide to a solution of $[Cr^{III}(tpenaH)]^{2+}$ in acetonitrile allowed a purple species to be generated.[89] This solution was frozen and characterized by rRaman spectroscopy. Three laser excitation wavelengths were used: 413.0 nm, 514.5 nm, and 647.1 nm. All showed a peak at 878 cm^{-1}, the intensity of which varied little compared to the solvent peaks. The spectrum from the 413.0 nm excitation was compared with spectra for $[Cr^{III}(tpenaH)]^{2+}$ and $[Cr^{III}(OH)(tpena)]^{2+}$ with the same excitation wavelength (Figure 5.15). Neither spectrum had a peak in that region. Based on this, the 878 cm^{-1} peak was assigned to an O-O stretching frequency. No ^{18}O-labeling was attempted as the equivalents of hydrogen peroxide needed for formation of the side-on peroxo complex would make labeling too expensive. Interestingly, the spectrum of the peroxo species excited by 647.1 nm laser line displayed a second peak, which may be the Cr-O stretch (Figure 5.14).

The frequency of the O-O stretch for the side-on peroxo species is comparable to other side-on peroxo species that have been reported previously (Table 5.4).[116,117] The only other known Cr side-on complex generated in acetonitrile $[Cr(\eta^2\text{-}O_2)(12\text{-}TMC)Cl]^+$ has a peak at 865 cm^{-1} corresponding to an O-O stretch,[116] which is similar to the 878 cm^{-1} reported here.

The O-O stretching frequencies are larger than those reported for side-on iron(III)-peroxo species (see Table 5.4), which is interesting, as there is a trend among TMC-based complexes from Fe to Co to Ni, where the O-O frequency increases across the row. However, chromium(IV) cannot donate into the O-O π^* orbital like the more electron rich metals can. Perhaps this donating ability is why later periodic metals are often incorporated into metalloenzymes.

Table 5.4: rRaman stretching frequencies of side-on peroxo species

Complex	O-O stretch (^{18}O) cm^{-1}	**Reference**
Cr(η_2-O_2)(tpena)	878	[89]
Cr(η_2-O_2)(12-TMC)Cl	865 (820)	[116]
(η_1-OO)(η_2-O_2)CrO_2(Xe)	917 (861)	[117]
Fe(η_2-O_2)TMC	825(781)/826(785)	[31,32]
Co(η_2-O_2)(12-TMC)	902 (845)	[118]
Ni(η_2-O_2)(12-TMC)	1002 (945)	[119]
Fe(N4Py)(η_2-O_2)	827 (780)	[105]
Fe(TPEN)(η_2-O_2)	817	[107]
Fe(EDTA)(η_2-O_2)	816 (776)	[120]
Fe(trispicMeen)(η_2-O_2)	819 (776)	[107]

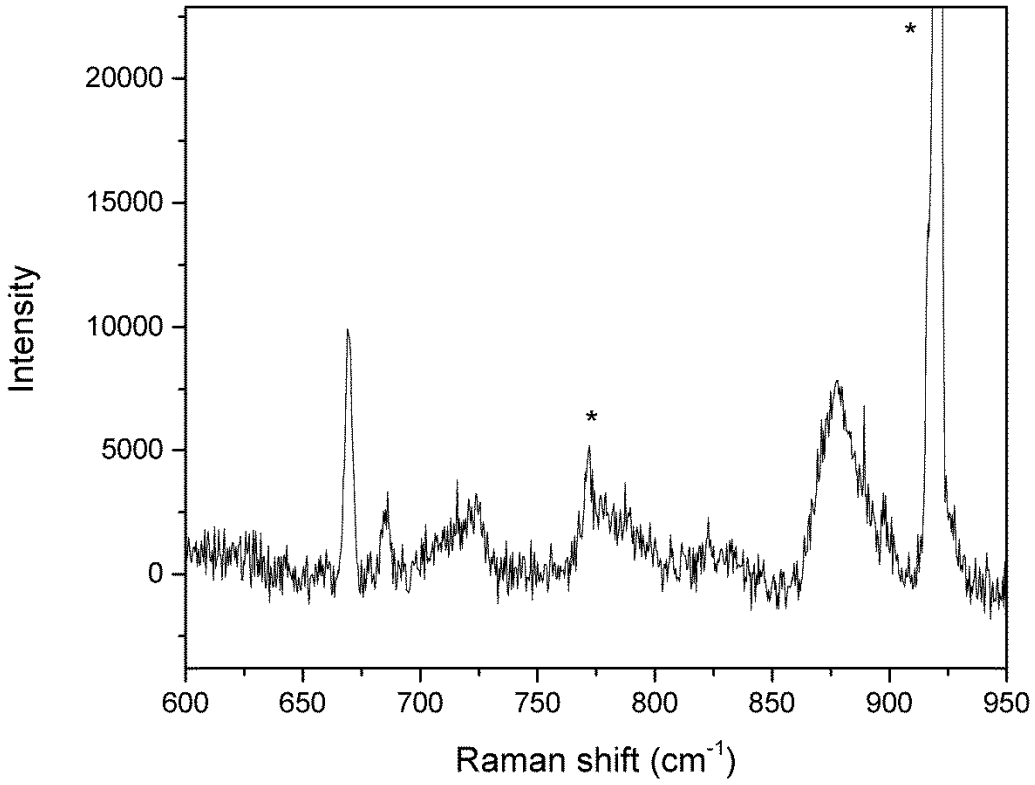

Figure 5.14: Resonance Raman spectrum of $[Cr(OO)(tpenaH)]^{2+}$ with an excitation of 647.1 nm. A peak at 878 cm^{-1} was observed, which was assigned to the O-O stretch. Lower frequency features may correspond to the Cr-O stretch. Solvent peaks marked with asterisks.

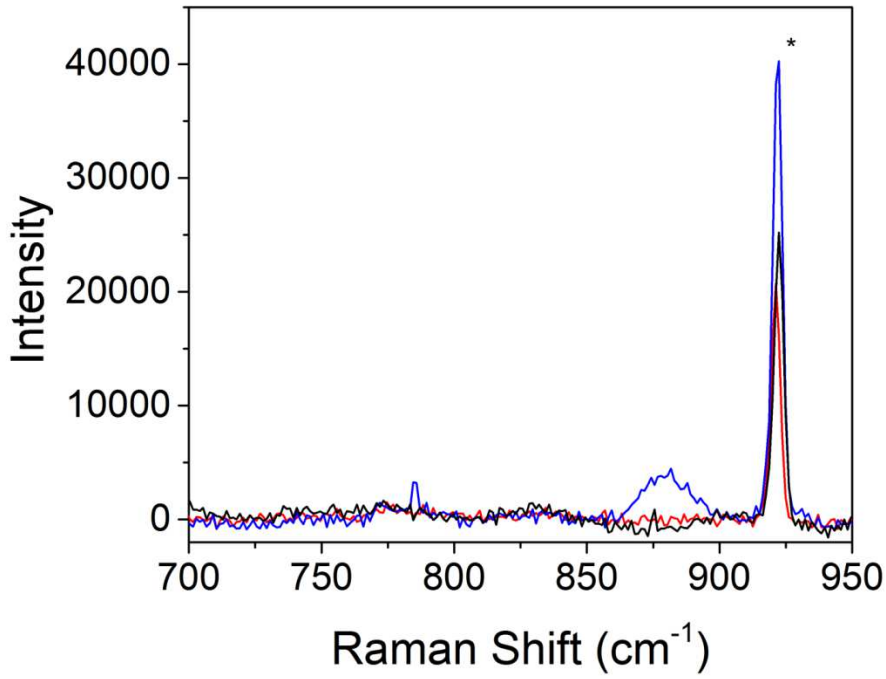

Figure 5.15: Resonance Raman spectrum of $[Cr(OO)(tpenaH)]^{2+}$ (blue), $[Cr(OH)(tpena)]^{+}$ (red), and $[Cr(tpenaH)]^{2+}$ (black) with an excitation of 413.0 nm. A peak at 878 cm^{-1} was observed only for $[Cr(OO)(tpenaH)]^{2+}$, which was assigned to the O-O stretch.

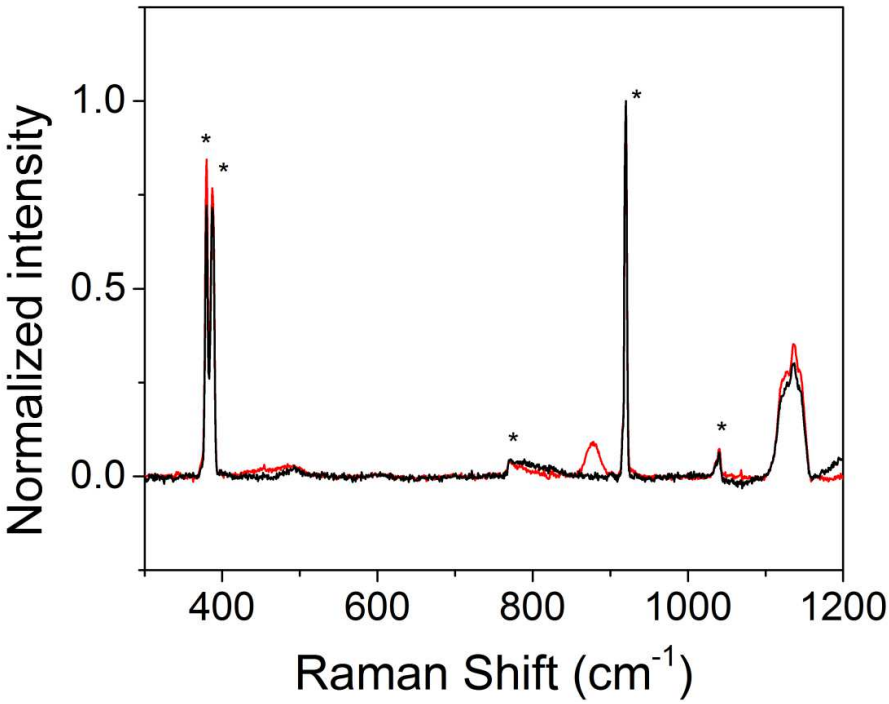

Figure 5.16: Resonance Raman spectrum of $[Cr(OO)(tpenaH)]^{2+}$ (red) and $[Cr(tpenaH)]^{2+}$ (black) with an excitation of 514.5 nm. A peak at 878 cm^{-1} was observed only for $[Cr(OO)(tpenaH)]^{2+}$, which was assigned to the O-O stretch.

5.4 Conclusion

Resonance Raman spectroscopy remains a spectroscopic tool especially useful in the bioinorganic field.[83] Resonance Raman spectroscopy allows us to probe the vibrations associated with a specific transition. The excitation into a LMCT band probes the metal bonding interactions. We have characterized a wide variety of complexes. While complexes, such as the iron(III)-peroxo species and the iron(IV)-oxo species, have been reported before, new techniques and comparisons increased the library of complexes to call upon. Newer complexes, of which there are few examples reported, such as the side-on Cr(IV)-peroxo and Fe(III)-iodosylarene species, allow for such a library to begin to expand our understanding the bonding of these complexes. Understanding the bonding of synthetic model complexes allows for us to better understand the bonding in metalloenzymes.

Chapter 6
Conclusions

6.1 Conclusions

While a wide array of topics have been covered within the field of biomimetic synthetic model complexes, each has a major conclusion that applies to the larger scope of synthetic model complexes.

6.1.1 Reactivity of Oxoiron(IV) Complexes

The iron(IV)-oxo complexes presented in chapters 2 and 3 show how variable the reactivity of iron(IV)-oxo complexes actually is, even using the same TMC-framework. Within the TMC-based iron(IV)-oxo complexes, there is no consistent correlation between HAT reactivity and $E_{p,c}$ values. Because the TSR model rests on a more electron-donating axial ligand bringing the $S = 1$ state closer to the $S = 2$ state, this data calls into question how relevant the TSR model is to understanding the HAT reactivity of iron(IV)-oxo complexes. While modifications to this model indicate the importance of a large tunneling component, this was not shown to be the deciding factor in the reactivity of axially ligated carboxylate complexes. Eyring plots of these complexes indicated the difference between tethered and untethered ligands was enthalpically based, likely due to axial bond weakening appearing necessary with the less flexible ligands.

6.1.2 Reactivity of Iron(II) Complexes with Dioxygen

Some reactions appear initially to be biomimetically relevant, but actually proceed through a different pathway. Such is the case of the radical reactions involving oxygen and either a proposed hydrogen atom transfer reagent or a reductant and a proton donor. While previously proposed to proceed through an iron(III)-superoxo that was converted to an iron(III)-peroxo, the sensitivity of rates to purification, radical traps, and radical initiators all indicate that the oxygen is first being activated to form peroxyl radicals that then react with the iron(II) complex. Careful evaluation of oxygen reactions for such radical involvement is absolutely necessary for the creation of true oxygen-activating synthetic model complexes.

6.1.3 Resonance Raman Spectroscopy of Metal Complexes

While many synthetic model complexes have been characterized, the expansion of the library of those complexes characterized by rRaman spectroscopy is especially illuminating. Some complexes fit well into previously defined categories: iron(IV)-oxo

complexes often have an Fe=O stretch in the range of 800-850 cm^{-1} and low-spin iron(III)-peroxo complexes have O-O vibrations from 790-810 cm^{-1},[1,17] which our complexes also showed. However, nonheme iron(III)-iodosylarene complexes are less well defined, and two distinct peaks, not previously seen, are indicative of these types of complexes. Also, the chromium side-on peroxo complex shows a similar O-O frequency to the only other recorded complex studied in solution of this type.

6.2 Future Work

The work in this thesis has attempted to answer many questions pertaining to nonheme synthetic model complexes, but questions still remain.

6.2.1 Reactivity of Iron(IV)-oxo Complexes

One intriguing question that still has not been fully answered is what factors affect HAT for iron(IV)-oxo complexes. Chapters 2 and 3 have tried to address differences with previously proposed models, but there still is no general understanding of the factors that contribute to HAT reactivity. The enthalpic difference between tethered and untethered axial ligands is especially intriguing. Some initial results have shown that higher enthalpies of activation are common for tethered ligands, but more enthalpic data would indicate if this is a common factor for all tethered systems. Systematic studies of the Eyring parameters for HAT reactions of oxoiron(IV) complexes are underway by our group and the Costas group, which should help illuminate the important components of HAT, especially if combined with computation studies.

The lack of a general correlation to $E_{p,c}$ values also indicates that the rate of HAT with iron(IV)-oxo complexes having TMC-based ligands are not controlled by electron transfer. Resonance Raman spectroscopic studies indicate that either the reactivity is not correlated to bond strength or that the iron(IV)-oxo stretches are not based entirely on bond strength. As there is also no correlation with KIE values, it seems likely that a new explanation must be proposed for the reactivity. One method for understanding the reaction better would be to characterize not just the organic products, but the iron products as well. This would likely require isolating the proposed iron(III)-hydroxo complexes, a challenging task within itself, as no one has to date isolated an

Fe^{III}(OH)TMC complex. TMC-based ligands are a candidate for trapping such a product, as they have been shown not to dimerize. Isolating the species produced after HAT reactions will help with DFT calculations and understanding the transition state. This information, combined with the Eyring parameters, will aid in determining what factors actually affect reactivity.

6.2.2 Reactivity of Iron(II) Complexes with Dioxygen

The results from radical formation in the presence of oxygen are especially important for evaluating both past and future work done with oxygen as the oxidant. All studies should rule out radicals before proposing any intermediate based on oxygen binding directly to iron. In fact, there are still studies in the literature that have not ruled out peroxyl radical formation in what has been proposed as dioxygen activation. For example, Nam has proposed that **10** reacts with dioxygen in the presence of a NADH mimic, BNAH, and an acid.[38] However, given the new information about dioxygen activation, it seems likely that this reaction also involves peroxyl radicals. Tests for radical formation should be conducted for it to be established as true dioxygen activation.

To actually pursue biomimetic dioxygen activation, second sphere modifications seem a likely avenue. The ability to stabilize certain intermediates may allow the iron center to activate dioxygen. Introduction of proton and electron donors in the second sphere may allow peroxo intermediates to be trapped and characterized. One complex has been able to complete these steps, but it has not yet led to the formation of an iron(IV)-oxo species from the peroxo complex.[35] A ligand with second sphere interactions may allow for an iron(II) complex to form a superoxo, then a peroxo, and finally an oxo species, all utilizing the same ligand.

6.2.3 Formation of Iron(V)-oxo Complexes

Formation of iron(V)-oxo complexes, which would mimic a proposed intermediate of Rieske dioxygenases, is an active area of research. Iodosylareneiron(III) complexes may allow for the formation of an iron(V)-oxo complex based on their previously proposed reactivity.[86] Photolytic reactions seem to hold promise for the generation of iron(V)-oxo complexes. By unmasking the iron(V)-oxo species, OAT reactivity can be compared to iron(IV)-oxo complexes, especially the reactivity of the

iron(IV)-oxo complex utilizing the same ligand system. Such systems will be helpful in understanding Rieske dioxygenases, and may react with similar substrates.

6.3 Larger Scope

Returning to the enzymes that inspired the investigations of this thesis, there is much to be applied from the studies of these biomimetic complexes. As mentioned in chapter 5, the library of complexes characterized by rRaman spectroscopy has grown, and even metal-replaced enzymes will likely have small molecule models available for comparison. The iron(IV)-oxo complexes do tease out some important features for nonheme monoiron enzymes to test. For instance, the importance in the flexibility of the carboxylate ligand towards reactivity indicates that a similar ligand flexibility could be present in heme or nonheme monoiron enzymes that allows for greater reactivity of the iron(IV)-oxo intermediate. It also seems likely that the ligands present in the active site are not there due to simply the electron-donating power of such ligands. Likely, the diversity seen in these ligands is promoted by second-sphere residues, which is emerging as a strategy to trap reactive intermediates and create effective catalysts in biomimetic systems. Focusing on these differences in nonheme monoiron enzymes might illuminate why such similar active sites have such a range of reactivity.

References

(1) Costas, M.; Mehn, M. P.; Jensen, M. P.; Que, Jr., L. *Chem. Rev.* **2004**, *104* (2), 939–986.

(2) Kovaleva, E. G.; Lipscomb, J. D. *Nat. Chem. Biol.* **2008**, *4* (3), 186–193.

(3) Riggs-Gelasco, P. J.; Shu, L.; Chen, S.; Burdi, D.; Huynh, B. H.; Que, Jr., L.; Stubbe, J. *J. Am. Chem. Soc.* **1998**, *120* (5), 849–860.

(4) Price, J. C.; Barr, E. W.; Tirupati, B.; Bollinger; Krebs, C. *Biochemistry* **2003**, *42* (24), 7497–7508.

(5) Proshlyakov, D. A.; Henshaw, T. F.; Monterosso, G. R.; Ryle, M. J.; Hausinger, R. P. *J. Am. Chem. Soc.* **2004**, *126* (4), 1022–1023.

(6) Hoffart, L. M.; Barr, E. W.; Guyer, R. B.; Bollinger, J. M.; Krebs, C. *Proc. Natl. Acad. Sci.* **2006**, *103* (40), 14738–14743.

(7) Galonić Fujimori, D.; Barr, E. W.; Matthews, M. L.; Koch, G. M.; Yonce, J. R.; Walsh, C. T.; Bollinger; Krebs, C.; Riggs-Gelasco, P. J. *J. Am. Chem. Soc.* **2007**, *129* (44), 13408–13409.

(8) Galonić, D. P.; Barr, E. W.; Walsh, C. T.; Bollinger, J. M.; Krebs, C. *Nat. Chem. Biol.* **2007**, *3* (2), 113–116.

(9) Matthews, M. L.; Krest, C. M.; Barr, E. W.; Vaillancourt, F. H.; Walsh, C. T.; Green, M. T.; Krebs, C.; Bollinger, J. M. *Biochemistry* **2009**, *48* (20), 4331–4343.

(10) Riggs-Gelasco, P. J.; Price, J. C.; Guyer, R. B.; Brehm, J. H.; Barr, E. W.; Bollinger, J. M.; Krebs, C. *J. Am. Chem. Soc.* **2004**, *126* (26), 8108–8109.

(11) Price, J. C.; Barr, E. W.; Glass, T. E.; Krebs, C.; Bollinger, J. M. *J. Am. Chem. Soc.* **2003**, *125* (43), 13008–13009.

(12) Panay, A. J.; Lee, M.; Krebs, C.; Bollinger, J. M.; Fitzpatrick, P. F. *Biochemistry* **2011**, *50* (11), 1928–1933.

(13) Eser, B. E.; Barr, E. W.; Frantom, P. A.; Saleh, L.; Bollinger; Krebs, C.; Fitzpatrick, P. F. *J. Am. Chem. Soc.* **2007**, *129* (37), 11334–11335.

(14) Brisson, L.; Bakkali-Taheri, N. E.; Giorgi, M.; Fadel, A.; Kaizer, J.; Réglier, M.; Tron, T.; Ajandouz, E. H.; Simaan, A. J. *J. Biol. Inorg. Chem.* **2012**, *17* (6), 939–949.

(15) Tamanaha, E. Showcasing two C-H bond-cleaving manifolds through mechanistic studies of isopenicillin N synthase. Ph.D., The Pennsylvania State University: United States -- Pennsylvania, 2013.

(16) Mukherjee, A.; Martinho, M.; Bominaar, E. L.; Münck, E.; Que, Jr., L. *Angew. Chem.* **2009**, *121* (10), 1812–1815.

(17) McDonald, A. R.; Que, Jr., L. *Coord. Chem. Rev.* **2013**, *257* (2), 414–428.

(18) Shaik, S.; Chen, H.; Janardanan, D. *Nat. Chem.* **2010**, *3* (1), 19–27.

(19) England, J.; Martinho, M.; Farquhar, E. R.; Frisch, J. R.; Bominaar, E. L.; Münck, E.; Que, Jr., L. *Angew. Chem., Int. Ed.* **2009**, *48* (20), 3622–3626.

(20) Bigi, J. P.; Harman, W. H.; Lassalle-Kaiser, B.; Robles, D. M.; Stich, T. A.; Yano, J.; Britt, R. D.; Chang, C. J. *J. Am. Chem. Soc.* **2012**, *134* (3), 1536–1542.

(21) England, J.; Guo, Y.; Van Heuvelen, K. M.; Cranswick, M. A.; Rohde, G. T.; Bominaar, E. L.; Münck, E.; Que, Jr., L. *J. Am. Chem. Soc.* **2011**, *133* (31), 11880–11883.

(22) Lacy, D. C.; Gupta, R.; Stone, K. L.; Greaves, J.; Ziller, J. W.; Hendrich, M. P.; Borovik, A. S. *J. Am. Chem. Soc.* **2010**, *132* (35), 12188–12190.
(23) Biswas, A. N.; Puri, M.; Meier, K. K.; Oloo, W. N.; Rohde, G. T.; Bominaar, E. L.; Münck, E.; Que, Jr., L. *J. Am. Chem. Soc.* **2015**, *137* (7), 2428–2431.
(24) Seo, M. S.; Kim, N. H.; Cho, K.-B.; So, J. E.; Park, S. K.; Clémancey, M.; Garcia-Serres, R.; Latour, J.-M.; Shaik, S.; Nam, W. *Chem. Sci.* **2011**, *2* (6), 1039–1045.
(25) Zhou, Y.; Shan, X.; Mas-Ballesté, R.; Bukowski, M. R.; Stubna, A.; Chakrabarti, M.; Slominski, L.; Halfen, J. A.; Münck, E.; Que, Jr., L. *Angew. Chem. Int. Ed.* **2008**, *47* (10), 1896–1899.
(26) Sastri, C. V.; Lee, J.; Oh, K.; Lee, Y. J.; Lee, J.; Jackson, T. A.; Ray, K.; Hirao, H.; Shin, W.; Halfen, J. A.; Kim, J.; Que, Jr., L.; Shaik, S.; Nam, W. *Proc. Natl. Acad. Sci.* **2007**, *104* (49), 19181–19186.
(27) Wilson, S. A.; Chen, J.; Hong, S.; Lee, Y.-M.; Clémancey, M.; Garcia-Serres, R.; Nomura, T.; Ogura, T.; Latour, J.-M.; Hedman, B.; Hodgson, K. O.; Nam, W.; Solomon, E. I. *J. Am. Chem. Soc.* **2012**, *134* (28), 11791–11806.
(28) Wang, D.; Ray, K.; Collins, M. J.; Farquhar, E. R.; Frisch, J. R.; Gómez, L.; Jackson, T. A.; Kerscher, M.; Waleska, A.; Comba, P.; Costas, M.; Que, Jr., L. *Chem. Sci.* **2012**, *4* (1), 282–291.
(29) Hong, S.; Lee, Y.-M.; Cho, K.-B.; Sundaravel, K.; Cho, J.; Kim, M. J.; Shin, W.; Nam, W. *J. Am. Chem. Soc.* **2011**, *133* (31), 11876–11879.
(30) Li, F.; England, J.; Que, Jr., L. *J. Am. Chem. Soc.* **2010**, *132* (7), 2134–2135.
(31) Li, F.; Meier, K. K.; Cranswick, M. A.; Chakrabarti, M.; Van Heuvelen, K. M.; Münck, E.; Que, Jr., L. *J. Am. Chem. Soc.* **2011**, *133* (19), 7256–7259.
(32) Cho, J.; Jeon, S.; Wilson, S. A.; Liu, L. V.; Kang, E. A.; Braymer, J. J.; Lim, M. H.; Hedman, B.; Hodgson, K. O.; Valentine, J. S.; Solomon, E. I.; Nam, W. *Nature* **2011**, *478* (7370), 502–505.
(33) Li, F.; Van Heuvelen, K. M.; Meier, K. K.; Münck, E.; Que, Jr., L. *J. Am. Chem. Soc.* **2013**, *135* (28), 10198–10201.
(34) Lee, Y.-M.; Bang, S.; Kim, Y. M.; Cho, J.; Hong, S.; Nomura, T.; Ogura, T.; Troeppner, O.; Ivanović-Burmazović, I.; Sarangi, R.; Fukuzumi, S.; Nam, W. *Chem. Sci.* **2013**, *4* (10), 3917–3923.
(35) Chiang, C.-W.; Kleespies, S. T.; Stout, H. D.; Meier, K. K.; Li, P.-Y.; Bominaar, E. L.; Que, Jr., L.; Münck, E.; Lee, W.-Z. *J. Am. Chem. Soc.* **2014**, *136* (31), 10846–10849.
(36) Thibon, A.; England, J.; Martinho, M.; Young Jr., V. G.; Frisch, J. R.; Guillot, R.; Girerd, J.; Münck, E.; Que, Jr., L.; Banse, F. *Angew. Chem. Int. Ed.* **2008**, *47* (37), 7064–7067.
(37) Hong, S.; Lee, Y.-M.; Shin, W.; Fukuzumi, S.; Nam, W. *J. Am. Chem. Soc.* **2009**, *131* (39), 13910–13911.
(38) Lee, Y.-M.; Hong, S.; Morimoto, Y.; Shin, W.; Fukuzumi, S.; Nam, W. *J. Am. Chem. Soc.* **2010**, *132* (31), 10668–10670.
(39) Nishida, Y.; Lee, Y.-M.; Nam, W.; Fukuzumi, S. *J. Am. Chem. Soc.* **2014**, *136* (22), 8042–8049.

(40) Krebs, C.; Galonić Fujimori, D.; Walsh, C. T.; Bollinger, J. M. *Acc. Chem. Res.* **2007**, *40* (7), 484–492.
(41) Hirao, H.; Que, Jr., L.; Nam, W.; Shaik, S. *Chem. Eur. J.* **2008**, *14* (6), 1740–1756.
(42) Saltzman, H.; Sharefin, J. G. *Org. Synth.* **1963**, *43*, 60–61.
(43) Royal, G.; Dahaoui-Gindrey, V.; Dahaoui, S.; Tabard, A.; Guilard, R.; Pullumbi, P.; Lecomte, C. *Eur. J. Org. Chem.* **1998**, *1998* (9), 1971–1975.
(44) Bucher, C.; Duval, E.; Barbe, J.-M.; Verpeaux, J.-N.; Amatore, C.; Guilard, R. *C. R. l'Academie. Sci., Ser. IIC Chem.* **2000**, *3* (3), 211–222.
(45) Studer, M.; Kaden, T. A. *Helv. Chim. Acta* **1986**, *69* (8), 2081–2086.
(46) Berry, J. F.; Bill, E.; Bothe, E.; Weyhermüller, T.; Wieghardt, K. *J. Am. Chem. Soc.* **2005**, *127* (33), 11550–11551.
(47) Hagadorn, J. R.; Que, Jr., L.; Tolman, W. B. *Inorg. Chem.* **2000**, *39* (26), 6086–6090.
(48) Rohde, J.-U.; In, J.-H.; Lim, M. H.; Brennessel, W. W.; Bukowski, M. R.; Stubna, A.; Münck, E.; Nam, W.; Que, Jr., L. *Science* **2003**, *299* (5609), 1037–1039.
(49) Warren, J. J.; Mayer, J. M. *J. Am. Chem. Soc.* **2011**, *133* (22), 8544–8551.
(50) Fukuzumi, S.; Kotani, H.; Suenobu, T.; Hong, S.; Lee, Y.-M.; Nam, W. *Chem. Eur. J.* **2010**, *16* (1), 354–361.
(51) George, G. N. *EXAFSPAK*; Stanford Synchrotron Radiation Laboratory: Stanford Linear Accelerator Center, Stanford, CA, 2000.
(52) Scarrow, R. C.; Trimitsis, M. G.; Buck, C. P.; Grove, G. N.; Cowling, R. A.; Nelson, M. J. *Biochemistry* **1994**, *33* (50), 15023–15035.
(53) Ankudinov, A. L.; Ravel, B.; Rehr, J. J.; Conradson, S. D. *Phys. Rev. B* **1998**, *58* (12), 7565–7576.
(54) Riggs-Gelasco, P. J.; Stemmler, T. L.; Penner-Hahn, J. E. *Coord. Chem. Rev.* **1995**, *144*, 245–286.
(55) Kaljurand, I.; Kütt, A.; Sooväli, L.; Rodima, T.; Mäemets, V.; Leito, I.; Koppel, I. A. *J. Org. Chem.* **2005**, *70* (3), 1019–1028.
(56) Izutsu, K. *Acid-base dissociation constants in dipolar aprotic solvents*; Blackwell Scientific Publications ; Brookline Village, Mass: Oxford ; Boston, 1990.
(57) Frisch, J. Spectroscopic and Crystallographic Characterization of Peroxo - and Oxoiron Complexes. Ph.D. Dissertation, University of Minnesota: Minneapolis, MN, 2010.
(58) Lee, Y.-M.; Kotani, H.; Suenobu, T.; Nam, W.; Fukuzumi, S. *J. Am. Chem. Soc.* **2008**, *130* (2), 434–435.
(59) England, J.; Guo, Y.; Farquhar, E. R.; Young Jr., V. G.; Münck, E.; Que, Jr., L. *J. Am. Chem. Soc.* **2010**, *132* (25), 8635–8644.
(60) England, J.; Bigelow, J. O.; Heuvelen, K. M. V.; Farquhar, E. R.; Martinho, M.; Meier, K. K.; Frisch, J. R.; Münck, E.; Que, Jr., L. *Chem. Sci.* **2014**, *5* (3), 1204–1215.
(61) Mandal, D.; Ramanan, R.; Usharani, D.; Janardanan, D.; Wang, B.; Shaik, S. *J. Am. Chem. Soc.* **2015**, *137* (2), 722–733.
(62) Schardt, B. C.; Hill, C. L. *Inorg. Chem.* **1983**, *22* (10), 1563–1565.

(63) Yang, W.; Giandomenico, C. M.; Sartori, M.; Moore, D. A. *Tetrahedron Lett.* **2003**, *44* (12), 2481–2483.
(64) Halfen, J. A.; Young, Jr., V. G. *Chem. Commun.* **2003**, No. 23, 2894.
(65) Ramirez, A. L. B.; Kean, Z. S.; Orlicki, J. A.; Champhekar, M.; Elsakr, S. M.; Krause, W. E.; Craig, S. L. *Nat. Chem.* **2013**, *5* (9), 757–761.
(66) Rabideau, P. W.; Mooney, J. L.; Lipkowitz, K. B. *J. Am. Chem. Soc.* **1986**, *108* (26), 8130–8134.
(67) Xue, G.; De Hont, R.; Münck, E.; Que, Jr., L. *Nature Chem.* **2010**, *2* (5), 400–405.
(68) Decker, A.; Rohde, J.-U.; Klinker, E. J.; Wong, S. D.; Que, Jr., L.; Solomon, E. I. *J. Am. Chem. Soc.* **2007**, *129* (51), 15983–15996.
(69) Lente, G.; Fábián, I.; Poë, A. J. *New J. Chem.* **2005**, *29* (6), 759–760.
(70) Espenson, J. *LSC Chemical Kinetics and Reaction Mechanisms*; McGraw-Hill Education, 2002.
(71) Solomon, E. I.; Wong, S. D.; Liu, L. V.; Decker, A.; Chow, M. S. *Curr. Opin. Chem. Biol.* **2009**, *13* (1), 99–113.
(72) Koehntop, K. D.; Emerson, J. P.; Que, Jr., L. *J. Biol. Inorg. Chem.* **2005**, *10* (2), 87–93.
(73) Morimoto, Y.; Lee, Y.-M.; Nam, W.; Fukuzumi, S. *Chem. Commun.* **2013**, *49* (25), 2500–2502.
(74) Comba, P.; Lee, Y.-M.; Nam, W.; Waleska, A. *Chem. Commun.* **2014**, *50* (4), 412–414.
(75) W. L. F. Armarego. *Purification of laboratory chemicals*, 4th ed..; Butterworth Heinemann: Oxford ; Boston, 1996.
(76) Chen, K.; Costas, M.; Kim, J.; Tipton, A. K.; Que, Jr., L. *J. Am. Chem. Soc.* **2002**, *124* (12), 3026–3035.
(77) Moore, J. W.; Pearson, R. G. *Kinetics and Mechanism*; John Wiley & Sons, 1981.
(78) Lee, D.; Newman, S. G.; Taylor, M. S. *Org. Lett.* **2009**, *11* (23), 5486–5489.
(79) Nishida, H.; Takada, N.; Yoshimura, M.; Sonoda, T.; Kobayashi, H. *Bull. Chem. Soc. Jpn.* **1984**, *57* (9), 2600–2604.
(80) Cooper, J. N.; Powell, R. E. *J. Am. Chem. Soc.* **1963**, *85* (11), 1590–1592.
(81) Geske, D. H. *J. Phys. Chem.* **1962**, *66* (9), 1743–1744.
(82) Amorati, R.; Pedulli, G. F.; Pratt, D. A.; Valgimigli, L. *Chem. Commun.* **2010**, *46* (28), 5139–5141.
(83) In *Physical methods in bioinorganic chemistry*; Que, Jr, L., Ed.; University Science Books: Sausalito, 2000; pp 287–274.
(84) Ye, W.; Ho, D. M.; Friedle, S.; Palluccio, T. D.; Rybak-Akimova, E. V. *Inorg. Chem.* **2012**, *51* (9), 5006–5021.
(85) Vad, M. S.; Lennartson, A.; Nielsen, A.; Harmer, J.; McGrady, J. E.; Frandsen, C.; Mørup, S.; McKenzie, C. J. *Chem. Commun.* **2012**, *48*, 10880–10882.
(86) Lennartson, A.; McKenzie, C. J. *Angew. Chem., Int. Ed.* **2012**, *51* (27), 6767–6770.
(87) Macikenas, D.; Skrzypczak-Jankun, E.; Protasiewicz, J. D. *J. Am. Chem. Soc.* **1999**, *121* (30), 7164–7165.

(88) Macikenas, D.; Skrzypczak-Jankun, E.; Protasiewicz, J. D. *J. Am. Chem. Soc.* **2011**, *133* (11), 4151–4151.
(89) De Sousa, D. P.; Bigelow, J. O.; Sundberg, J.; Que, Jr., L.; McKenzie, C. J. *Chem. Commun.* **2015**, *51* (14), 2802–2805.
(90) Codolà, Z.; Gómez, L.; Kleespies, S. T.; Que, Jr, L.; Costas, M.; Lloret-Fillol, J. *Nat. Commun.* **2015**, *6*:5865 doi: 10.1038/ncomms6865
(91) Lee, Y.-M.; Dhuri, S. N.; Sawant, S. C.; Cho, J.; Kubo, M.; Ogura, T.; Fukuzumi, S.; Nam, W. *Angew. Chem., Int. Ed.* **2009**, *48* (10), 1803–1806.
(92) Hong, S.; Wang, B.; Seo, M. S.; Lee, Y.-M.; Kim, M. J.; Kim, H. R.; Ogura, T.; Garcia-Serres, R.; Clémancey, M.; Latour, J.-M.; Nam, W. *Angew. Chem. Int. Ed.* **2014**, *53* (25), 6388–6392.
(93) Siebert, H.; Handrich, M. *Z. Anorg. Allg. Chem.* **1976**, *426* (2), 173–183.
(94) Draksharapu, A.; Angelone, D.; Quesne, M. G.; Padamati, S. K.; Gómez, L.; Hage, R.; Costas, M.; Browne, W. R.; de Visser, S. P. *Angew. Chem. Int. Ed.* **2015**, *54* (14), 4357–4361.
(95) Lehnert, N.; Ho, R. Y. N.; Que, Jr., Lawrence; Solomon, E. I. *J. Am. Chem. Soc.* **2001**, *123* (34), 8271–8290.
(96) Bautz, J.; Comba, P.; Que, Jr., L. *Inorg. Chem.* **2006**, *45* (18), 7077–7082.
(97) Jensen, M. P.; Costas, M.; Ho, R. Y. N.; Kaizer, J.; Mairata i Payeras, A.; Münck, E.; Que, Jr., Lawrence; Rohde, J.-U.; Stubna, A. *J. Am. Chem. Soc.* **2005**, *127* (30), 10512–10525.
(98) Zang, Y.; Elgren, T. E.; Dong, Y.; Que, Jr., L. *J. Am. Chem. Soc.* **1993**, *115* (2), 811–813.
(99) Kitagawa, T.; Dey, A.; Lugo-Mas, P.; Benedict, J. B.; Kaminsky, W.; Solomon, E.; Kovacs, J. A. *J. Am. Chem. Soc.* **2006**, *128* (45), 14448–14449.
(100) Wada, A.; Ogo, S.; Nagatomo, S.; Kitagawa, T.; Watanabe, Y.; Jitsukawa, K.; Masuda, H. *Inorg. Chem.* **2002**, *41* (4), 616–618.
(101) Brunold, T. C.; Solomon, E. I. *J. Am. Chem. Soc.* **1999**, *121* (36), 8277–8287.
(102) Katona, G.; Carpentier, P.; Nivière, V.; Amara, P.; Adam, V.; Ohana, J.; Tsanov, N.; Bourgeois, D. *Science* **2007**, *316* (5823), 449–453.
(103) Krishnamurthy, D.; Kasper, G. D.; Namuswe, F.; Kerber, W. D.; Narducci Sarjeant, A. A.; Moënne-Loccoz, P.; Goldberg, D. P. *J. Am. Chem. Soc.* **2006**, *128* (44), 14222–14223.
(104) Namuswe, F.; Kasper, G. D.; Sarjeant, A. A. N.; Hayashi, T.; Krest, C. M.; Green, M. T.; Moënne-Loccoz, P.; Goldberg, D. P. *J. Am. Chem. Soc.* **2008**, *130* (43), 14189–14200.
(105) Roelfes, G.; Vrajmasu, V.; Chen, K.; Ho, R. Y. N.; Rohde, J.-U.; Zondervan, C.; la Crois, R. M.; Schudde, E. P.; Lutz, M.; Spek, A. L.; Hage, R.; Feringa, B. L.; Münck, E.; Que, Jr., L. *Inorg. Chem.* **2003**, *42* (8), 2639–2653.
(106) Ho, R. Y. N.; Roelfes, G.; Feringa, B. L.; Que, Jr., L. *J. Am. Chem. Soc.* **1999**, *121* (1), 264–265.
(107) Simaan, A. J.; Döpner, S.; Banse, F.; Bourcier, S.; Bouchoux, G.; Boussac, A.; Hildebrandt, P.; Girerd, J.-J. *Eur. J. Inorg. Chem.* **2000**, *2000* (7), 1627–1633.
(108) Mekmouche, Y.; Hummel, H.; Ho, R. Y. N.; Que, Jr., L.; Schünemann, V.; Thomas, F.; Trautwein, A. X.; Lebrun, C.; Gorgy, K.; Leprêtre, J.-C.; Collomb,

M.-N.; Deronzier, A.; Fontecave, M.; Ménage, S. *Chem. Eur. J.* **2002**, *8* (5), 1196–1204.
(109) Balland, V.; Banse, F.; Anxolabéhère-Mallart, E.; Ghiladi, M.; Mattioli, T. A.; Philouze, C.; Blondin, G.; Girerd, J.-J. *Inorg. Chem.* **2003**, *42* (7), 2470–2477.
(110) Srinivasan, K.; Kochi, J. K. *Inorg. Chem.* **1985**, *24* (26), 4671–4679.
(111) Nill, K. H.; Wasgestian, F.; Pfeil, A. *Inorg. Chem.* **1979**, *18* (3), 564–567.
(112) Collins, T. J.; Slebodnick, C.; Uffelman, E. S. *Inorg. Chem.* **1990**, *29* (18), 3433–3436.
(113) Cho, J.; Woo, J.; Han, J. E.; Kubo, M.; Ogura, T.; Nam, W. *Chem. Sci.* **2011**, *2* (10), 2057–2062.
(114) O'Reilly, M. E.; Del Castillo, T. J.; Falkowski, J. M.; Ramachandran, V.; Pati, M.; Correia, M. C.; Abboud, K. A.; Dalal, N. S.; Richardson, D. E.; Veige, A. S. *J. Am. Chem. Soc.* **2011**, *133* (34), 13661–13673.
(115) Cho, J.; Sarangi, R.; Nam, W. *Acc. Chem. Res.* **2012**, *45* (8), 1321–1330.
(116) Yokoyama, A.; Han, J. E.; Cho, J.; Kubo, M.; Ogura, T.; Siegler, M. A.; Karlin, K. D.; Nam, W. *J. Am. Chem. Soc.* **2012**, *134* (37), 15269–15272.
(117) Zhao, Y.; Su, J.; Gong, Y.; Li, J.; Zhou, M. *J. Phys. Chem. A* **2008**, *112* (37), 8606–8611.
(118) Cho, J.; Sarangi, R.; Kang, H. Y.; Lee, J. Y.; Kubo, M.; Ogura, T.; Solomon, E. I.; Nam, W. *J. Am. Chem. Soc.* **2010**, *132* (47), 16977–16986.
(119) Cho, J.; Sarangi, R.; Annaraj, J.; Kim, S. Y.; Kubo, M.; Ogura, T.; Solomon, E. I.; Nam, W. *Nat Chem* **2009**, *1* (7), 568–572.
(120) Neese, F.; Solomon, E. I. *J. Am. Chem. Soc.* **1998**, *120* (49), 12829–12848.

Appendix

Figure 3.S1. The electrospray ionization mass spectrum (ESI-MS) of **3**(BPh_4) showing the observed (top) and expected (bottom) isotope distribution patterns for the ion fragment **3**. Work performed by Dr. Jason England.

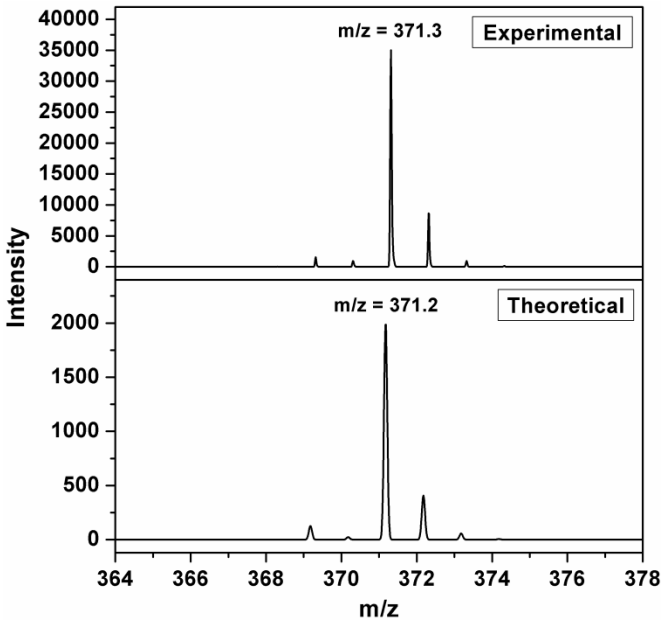

Figure 3.S2. The electrospray ionization mass spectrum (ESI-MS) of **7**(BPh_4), showing the observed (top) and expected (bottom) isotope distribution patterns for the ion fragment **7**. Work performed by Dr. Jason England.

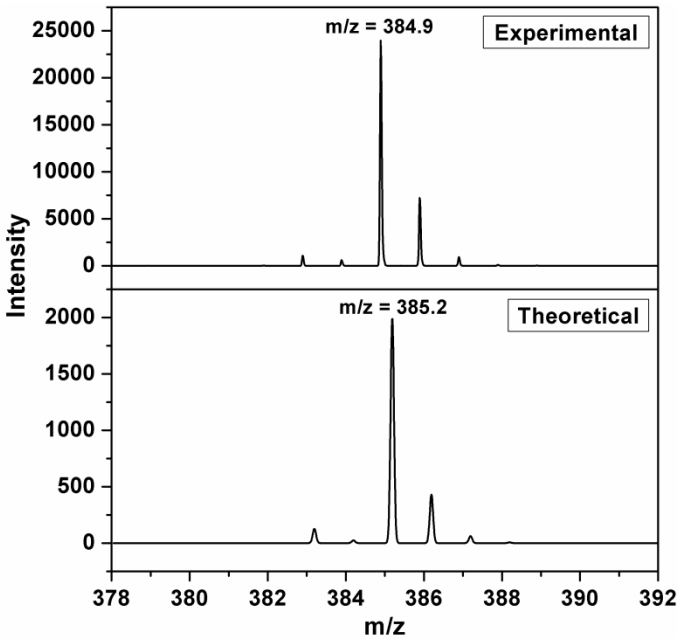

Figure 3.S3. The electrospray ionization mass spectrum (ESI-MS) of **8**[OTf], showing the observed (top) and expected (bottom) isotope distribution patterns for the ion fragment **8.** Work performed by Dr. Jason England.

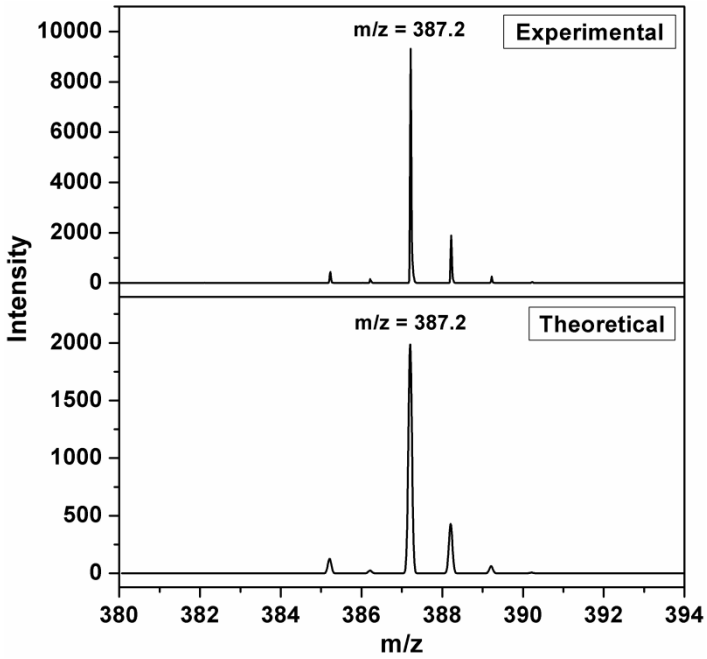

Figure 3.S4. Resonance Raman spectra (λ_{ex} = 407 nm, power = 20 mW) of the carboxylate bound oxoiron(IV) complexes (black lines) and their ^{18}O-labeled isotopomers (red lines), recorded in frozen CH_3CN solution. Top panel: **3**; middle panel: **7**; bottom panel: **8**. Work performed by Dr. Jonathan Frisch.

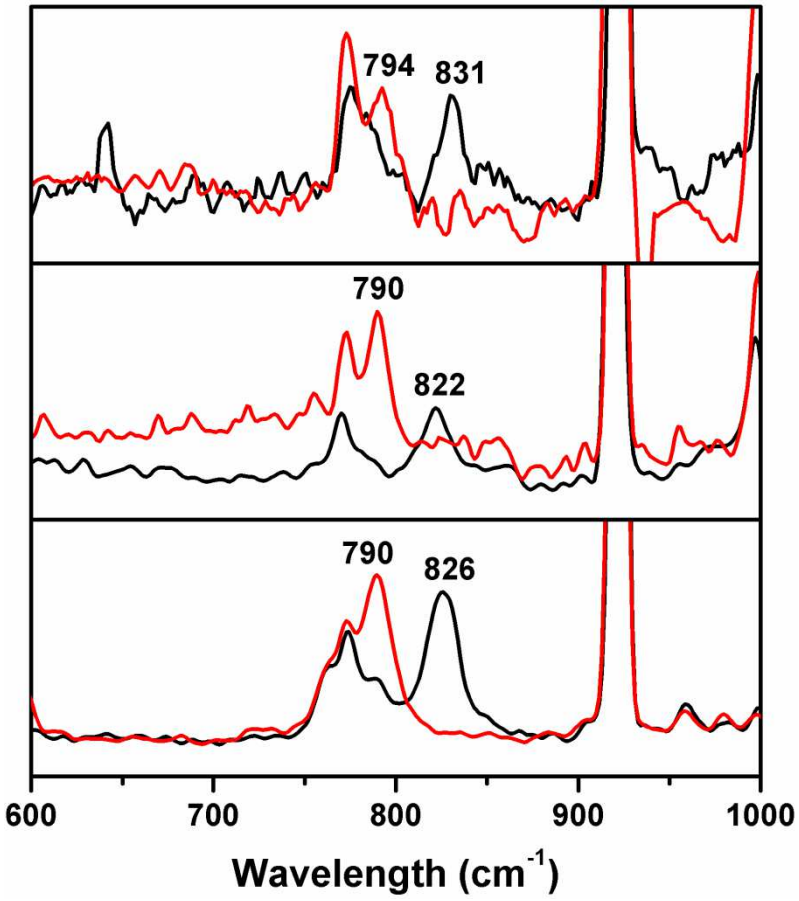

Figure 3.S5. ^{1}H-NMR spectra of **3** (upper panel) and **7** (lower panel) recorded in CD_3CN solution at room temperature. Acquisition time = 0.064 sec.; relaxation delay = 0.03 sec.; line broadening factor = 30 Hz. Comprehensive peak assignments are provided below. Work performed by Dr. Jason England.

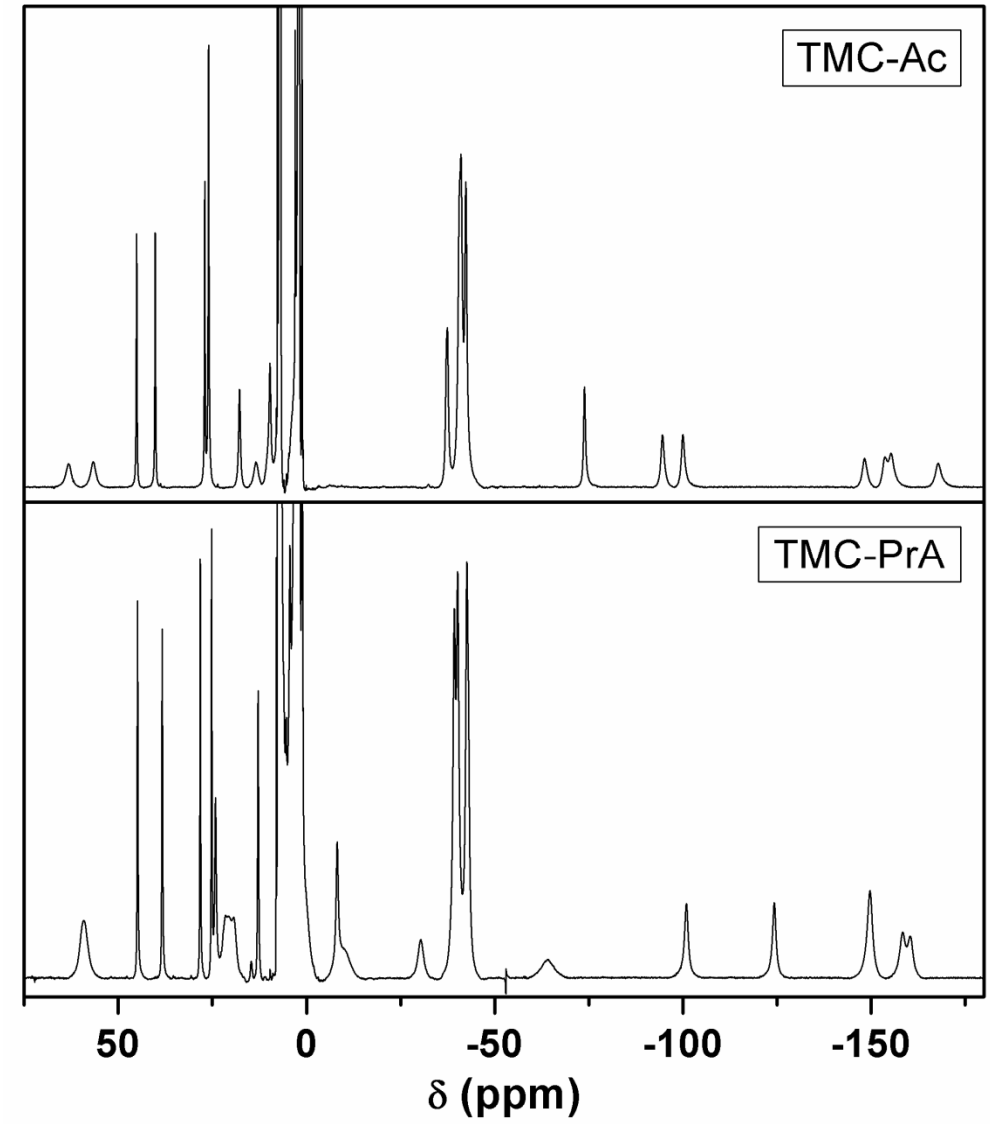

Figure 3.S6. ^{1}H-NMR spectra of **3** (upper panel) and **8** (lower panel) recorded in CD_3CN solution at -20°C. Acquisition time = 0.064 sec.; relaxation delay = 0.03 sec.; line broadening factor = 30 Hz. Comprehensive peak assignments are provided below. Work performed by Dr. Jason England.